SAPIENZA
UNIVERSITÀ DI ROMA

Berezinskii-Kosterlitz-Thouless transition in disordered superconducting films

Candidate

Ilaria Maccari

ID number 1209648

Thesis Advisors

Prof. Claudio Castellani

Dr. Lara Benfatto

Thesis defended on 26 February 2018
in front of a Board of Examiners composed by:

Prof. Thierry Giamarchi
Prof. Antonio Garcia-Garcia
Prof. Andrea Crisanti (chairman)

Berezinskii-Kosterlitz-Thouless transition in disordered superconducting films
Ph.D. thesis. Sapienza – University of Rome

This thesis has been typeset by LaTeX and the Sapthesis class.

Version: February 2018

Author's email: ilaria.maccari@uniroma1.it

Dedicated to
a 40-years revolutionary story.

Contents

Introduction

More than 40 years after the seminal work by Berezinskii[1] Kosterlitz and Thouless[2, 3] the BKT transition remains one of the most fascinating examples of topological phase transitions, as it had been acknowledged by the 2016 Nobel Prize in Physics. Its universality class describes several phenomena ranging from the quantum metal-insulator transition in one dimension to the Coulomb-gas screening transition in 2D, and of course the metal-to-superfluid transition in 2D[4]. As such it has been investigated in neutral superfluids, as e.g. thin He films[5] and cold-atoms systems made of bosons[6] or neutral fermions[7], but also in quasi-two-dimensional (2D) superconductors. The latter case is certainly the one which attracted most attention, since it can be detected with different probes and it applies to a wide class of systems: not only to thin films of conventional [8]-[9] and unconventional[10]-[11] superconductors, but also to the artificially confined 2D electron gas at the interface between two insulators in artificial heterostructures[12, 13], or in the top-most layer of ion-gated superconducting (SC) systems[14]. Nevertheless, the experimental observations made so far in real materials are often at odds with the predictions of the BKT transition and seem to point towards a kind of "unconventional" BKT physics. In particular, a typical example is the behavior of the superfluid-density which gives access to the most spectacular manifestation of the BKT transition, exhibiting a discontinuous jump to zero as soon as the system reaches the BKT critical temperature, leading thus to the sudden vanishing of the SC state. However, as a matter of fact, several experimental results[8, 15, 16, 17, 18, 19, 20, 21] show a systematical smearing out of the superfluid density jump, revealing a rapid downturn much broader than that observed in the case of superfluid helium films[5]. The effect is even more dramatic in ultrathin films of cuprate superconductors[22], where the BKT jump is completely lost by underdoping. A common characteristic of the cases mentioned above is that the BKT transition is expected to occur in presence of a spatial inhomogeneity of the SC order parameter, which results to be fragmented on a mesoscopic scale. This can be due to the presence of strong disorder, as in the case of thin disordered films of conventional superconductors, to the artificial optical confinement, as in the SC interfaces, or to the intrinsic nature of the system, as it occurs in cuprate superconductors. This issue raised new questions on the nature of the BKT transition in real materials, particularly on the role of the inhomogeneity on its critical behavior.

Understanding the role of microscopic electronic disorder on the BKT transition within SC fermionic model is an incredible task [23, 24, 25, 26], due mainly to the small size of systems accessible numerically. Alternatively, one can address the question directly within a proper phase-only model. A natural option is the

classical *XY* model with random couplings[27, 28, 29, 30], which mimics the random Josephson-like couplings between coarse-grained neighboring SC islands.

In this PhD Thesis, I have studied the effect of disorder on the BKT transition by means of Monte Carlo simulations on a disordered 2D *XY* model.

$$H = -\sum_{ij} J_{ij} \cos(\theta_i - \theta_j) \qquad (0.1)$$

where θ_i is the angular variable for the 2D (planar) spins, or equivalently the SC phase in the mapping to a SC problem. The spatial arrangement of the couplings J_{ij} between neighboring sites i, j is taken to mimic both uncorrelated and spatially-correlated disorder. As long as the couplings are spatially uncorrelated, the Harris criterium[31], guarantees that the disorder is irrelevant at the transition, so that, for example, the "universal" jump[32] of the superfluid stiffness at T_{BKT} is still preserved. Our Monte Carlo simulations not only confirmed this expectation, but they also revealed the irrelevance of the uncorrelated disorder away from the critical temperature. To get a deeper inside on this behavior, we have analytically demonstrated the universality of the spin-wave excitations, in the presence of uncorrelated disorder, by means of a perturbation expansion around an effective value of the local stiffness, in analogy with the original idea of the effective-medium theory applied to the formally equivalent Random-Resistor Network (RRN) problem[33].

The core of this Thesis is, however, the study of the BKT transition when the spatial arrangements of the couplings J_{ij} imitates the granular inhomogeneity experimentally observed, instead of being uncorrelated. With this purpose, the spatially correlated disordered couplings have been generated by the mean-field solution of the (quantum) *XY* model in a random transverse field (RTF), which has been recently proven to model disordered superconductors with a non-trivial granular space structure [34, 35, 36]. At weak disorder, the RTF model does not show any significant difference with respect to the uncorrelated-disorder case: the robustness of the BKT transition is preserved also away from the transition, with a universal rescaled behavior. On the contrary, the fragmentation of the SC state, obtained within the RTF model at the strong disorder, leads to a pronounced smearing of the BKT jump, in analogy with experimental observations. Our study reveals also that the underlying mechanism of the observed broadening is the anomalous nucleation of vortices, which occurs even at very low temperature within those regions in space where the local stiffness is strongly suppressed. Despite the observed smearing, the study of the finite size effects reveals that the universality class remains the BKT one, although the rescaled critical temperature results to be reduced in the presence of (strong) disorder with spatial correlations and the low-temperature dependence of the superfluid stiffness is different, a feature that could be tested on a Josephson-junctions disordered array.

An interesting extension of the study of phase fluctuations in thin SC films is the application of a transverse magnetic field, which induces a finite number of vortices with a given vorticity within the system. This has found recent experimental application both in thin SC films[37, 38]-[39], in layered high-T_c superconductors[40] and even in cold atomic systems, where the magnetic field is mimicked by imposing a rotation on the condensate[41]-[42].

Despite the large theoretical effort devoted to this field [43, 44, 45, 46]-[47], it is still not well understood how the BKT transition is modified by the presence of a

transverse magnetic field and it is even less clear the interplay between the applied field and the intrinsic inhomogeneity observed in the most of the real systems.

Very recently[38], it has been shown that the application of a transverse magnetic field on a weakly disordered SC films acts on the system by increasing its inner inhomogeneity, inducing a further fragmentation of the SC order parameter and pushing the system towards a pseudo-gap state governed by phase fluctuations. Moreover, by effect of the inhomogeneity, the ordered Abrikosov lattice observed in clean system modifies becoming disordered as well. We have addressed this interesting issue by means of Monte Carlo simulations on the uniformly frustrated XY model[46]-[47] in the presence of disordered couplings, recovering both the increase of the inhomogeneity by the applied field and the modification of the zero-temperature vortex lattice.

Finally, we have also studied how the superfluid-stiffness transition gets affected by the presence of the magnetic field both in the clean and in the disordered case. In the absence of disordered couplings, it is known[47] that a very small amount of magnetic flux within the system strongly suppresses the SC transition, since the few induced vortices are almost free to move within the film destroying any phase rigidity. It follows that, for a clean system, the superconducting critical temperature decreases with the decrease of the applied field, going to zero in the limit of infinitesimal amount of magnetic flux. What found in[47] appears to be completely at odd with some recent experimental results[48], in which it is shown an inverse proportionality between the critical temperature and the applied field.

In this work we have shown that once the disorder is taken into account, the experimentally observed dependency between T_c and the applied field is recovered. The presence of the inhomogeneity, indeed, by acting as a pinning potential for vortices, can make the vortex lattice more robust against thermal fluctuations, restoring the behavior observed experimentally.

This PhD Thesis is organised as follows: in Chapter 1, I will review the main aspects of the BKT transition within the classical two-dimensional XY model, showing its mapping both with the Coulomb-gas and with the one-dimensional sine-Gordon quantum model, discussing in the last section the BKT renormalization group's equations.

In Chapter 2, I will clarify why and under which conditions the 2D XY model is an effective model for superconducting thin films, starting from the analogy with superfluid films. I will then present the main ways to experimentally probe the BKT signatures in these SC systems, highlighting the main puzzling results.

Chapter 3 is devoted to role of disorder to induce an emergent inhomogeneity of the SC state, as observed both in thin SC films, by reducing the film thickness, and in layered SC, by underdoping the system. The two main theoretical models, the fermionic and the bosonic one are here discussed. In this Chapter, it is also presented the complete derivation of the mean-field spatially correlated couplings used in the rest of the Thesis.

In Chapter 4, I will present the Monte Carlo numerical results obtained both for the clean case and for the case of two kind of spatially uncorrelated disorder: random couplings with a Gaussian distribution and random link dilution. In the last section an effective medium theory for the disordered XY model is derived by a perturbation expansion around an effective value of the stiffness. The publication of this study is

actually under preparation.

In Chapter 5, I will instead address the case of spatially correlated disorder, showing by means of Monte Carlo simulations that when the couplings aggregation is enough pronounced within the system, an anomalous nucleation of vortices starts to occur even in the low-temperature regime, causing a symmetric smearing of the superfluid stiffness jump at the critical temperature. The details of this work can be found in the publication[49]. In the last section of the Chapter, we have also added to this study, the analysis of the finite size scaling in the two cases: the homogeneous and the spatially-correlated disordered one.

Finally in Chapter 6, after having presented the main and more recent experimental results, I will show and discuss the results of the Monte Carlo simulations on the XY model in the presence of a transverse magnetic field. I will show how the vortex lattice and the superfluid stiffness trend in temperature drastically modifies respect to zero-field case, highlighting the main differences occurring when the system considered is also inhomogeneous and disordered. These results are finally compared with some unpublished experimental results taken by the group of Prof. Raychaudhuri in Mumbai. The work, enriched by this collaboration, is under preparation and it will be soon available on the online arXiv.

Chapter 1

Berezinskii-Kosterlitz-Thouless transition

1.1 2D XY model

In this section, I will review the discovery and the characterisation of the Berezinskii-Kosterlitz-Thouless (BKT)[1][2][3] transition within the context of its paradigmatic formulation for the classical XY model. The model describes the ferromagnetic interactions between planar spins with fixed modulus ($|\vec{\mathbf{S}}_i| = 1$), placed on a square lattice. Its Hamiltonian reads:

$$H_{XY} = -J \sum_{<i,j>} \vec{\mathbf{S}}_i \cdot \vec{\mathbf{S}}_j = -J \sum_{<i,j>} \cos(\theta_i - \theta_j), \qquad (1.1)$$

being $\sum_{<i,j>}$ the sum restricted to nearest neighbors spins and J a positive coupling constant. Despite its simplicity, this model has been one of the biggest puzzle of the last century because of its peculiar phase transition, that occurs without any breaking of a given symmetry.

From (1.1), it is straightforward to recognise that the system shows two different symmetries:

- A continuous and global symmetry $U(1)$:

$$\forall i : \theta_i \to \theta_i + c$$

- A discrete and local symmetry $\mathbb{Z}^m$:

$$\theta_i \to \theta_i + 2\pi m$$

In the following, we will see that these two symmetries will give rise to two different phase excitations: the first responsible for the lack of order at any finite temperature and the second responsible for the occurrence of a phase transition, whose main signature is the sudden loss of spin rigidity of the system.

Let us proceed step by step. Looking again at the Hamiltonian (1.1), it can be easily seen that the minimum value of the energy corresponds to a situation in which all the spins are aligned in one particular direction, breaking in this way the $U(1)$

symmetry of the Hamiltonian itself. We can then wonder if it is possible to identify a finite critical temperature at which a spontaneous symmetry breaking occurs. We have already anticipated the answer, but let us give some more details about the Mermin-Wagner theorem[50].

1.2   Lack of ordering in two dimensions

At the time of the Mermin-Wagner theorem[50] formulation in 1966, several physicists were investigating the presence or the absence of phase transitions in low-dimensional systems ($d = 1, 2$) with short-range interactions. Among them, Peierls[51] in 1936 had already given an argument which excluded long range translational order in 2D. At the same time, almost concomitantly with [50], Hohenberg[52] (1967) showed, using the Bogoliubov inequality, that there is no Bose-Einstein condensation, so no conventional superfluid or superconducting order, in one- and two-dimensional systems. Using a similar application of the Bogoliubov inequality, Mermin and Wagner proved rigorously in their seminal paper[50] that the one- and two-dimensional isotropic Heisenberg models, with short range interactions, have no long-range order at any finite temperature. Referring at the original paper[50] for the demonstration of the theorem, we will give here a simple demonstration of the lack of long-range order at any nonzero temperature for the case of the XY model.

Since we are interested in the low-temperature regime, where the difference in angle between neighboring spins is very small, we can rewrite the Hamiltonian (1.1) expanding the cosine up to the second order in its argument. Furthermore, because of the slow variation of the spin angles on the scale of the lattice, we can approximate $\theta_i - \theta_{i+\hat{\delta}} \approx a\partial\theta(\mathbf{r})/\partial\hat{\delta}$ where $\theta(\mathbf{r})$ is a smooth function and $\hat{\delta} = x, y$. Finally, we get:

$$H_{XY} \simeq \frac{J}{2} \int d\mathbf{r}[\nabla\theta(\mathbf{r})]^2 = \frac{J}{2} \int \frac{d\mathbf{q}}{(2\pi)^2} \mathbf{q}^2 |\theta_{\mathbf{q}}|^2 \tag{1.2}$$

The quantity we want to compute is:

$$\langle \mathbf{S}_i \rangle = \langle e^{i\theta_i} \rangle = e^{-\langle \theta_i^2 \rangle/2} \tag{1.3}$$

In the last passage we have used a well known property of the average over a Gaussian distribution, while the average $\langle \ldots \rangle$ is the average over the canonical ensamble of the system:

$$\langle A \rangle = \frac{1}{Z} \int_0^{2\pi} d\theta_1 \cdots \int_0^{2\pi} d\theta_N A e^{-\beta H_{XY}} \tag{1.4}$$

where as usual $\beta = 1/T$.

The calculation (1.3) is then very easy:

$$\langle \theta_i^2 \rangle = \int \frac{d\mathbf{q}}{(2\pi)^2} \langle |\theta_{\mathbf{q}}|^2 \rangle = \int_{1/L}^{1/a} \frac{d\mathbf{q}}{(2\pi)^2} \frac{T}{J\mathbf{q}^2} = \frac{T}{2\pi J} \ln(\frac{L}{a}) \tag{1.5}$$

being L the linear size of the system and a the lattice spacing between two neighbors spins. Substituting the result in (1.3) we get:

$$\langle \mathbf{S}_i \rangle = e^{-\frac{T}{4\pi J} \ln(L/a)} = \left(\frac{a}{L}\right)^{\frac{T}{4\pi J}} \xrightarrow[L\to\infty]{} 0 \tag{1.6}$$

Hence, at any nonzero temperature the system has no spontaneous magnetization in the thermodynamic limit. The spin waves excitations, smooth variations of the phase within the system, are responsible for the lack of order: in the 2D XY model they have no mass and they can be recognised as the Goldstone modes of the system. However, it is worth to mention that very often real systems are quite far from the thermodynamic limit so that they could exhibit a finite magnetization in the low-temperature regime. Indeed, if we estimate the exponent of (1.6), using the universal relation between the renormalized stiffness J and the temperature at the critical point (we will come back on this point in the next pages), we obtain that it is $\leq 1/8$. It means that for a microscopic scale $a \sim 10 \, nm$ one would need a system with a linear size $L \sim 100000 \, km$ to have $\langle \mathbf{S}_i \rangle = 0.01$. In short, if a real finite system exhibits a spontaneous symmetry breaking, it does not mean that the Mermin Wagner theorem is violated, but that the system studied is far away from its thermodynamic limit.

Anyway, at the time of its formulation, the general accepted conclusion was that in the XY model[1] there is no transition to an ordered state at any nonzero temperature. The merit of Berezinskii, Kosterlitz and Thouless was first of all to overcome this idea, starting from other signals announcing that a sort of phase transition should still occur in the XY model.

1.3 Correlation functions and Spin stiffness

The main hint, indicating the presence of a phase transition in the model, come from the behavior of the correlation functions in the two regimes: the high and the low temperature one. The correlation function between two sites i and j is defined as:

$$C(\mathbf{r}_i - \mathbf{r}_j) = \langle \mathbf{S}_i \cdot \mathbf{S}_j \rangle = \langle \cos(\theta_i - \theta_j) \rangle \tag{1.7}$$

In the high temperature limit, since $\beta J \ll 1$, we can expand the exponent of the partition function (1.4) as follows:

$$C(\mathbf{r}_1 - \mathbf{r}_2) = \frac{\int_0^{2\pi} \prod_i d\theta_i \cos(\theta_1 - \theta_2) \sum_n \frac{(\beta J)^n}{n!} \left[\sum_{<i,j>} \cos(\theta_i - \theta_j) \right]^n}{\int_0^{2\pi} \prod_i d\theta_i \sum_n \frac{(\beta J)^n}{n!} \left[\sum_{<i,j>} \cos(\theta_i - \theta_j) \right]^n} \tag{1.8}$$

Following the procedure of[53], the cosine terms in (1.8) can be written as the sum of two exponentials: $\cos(\theta_i - \theta_j) = \frac{1}{2}(e^{i(\theta_i - \theta_j)} + e^{i(\theta_j - \theta_i)})$ and each exponential can be represented as an arrow connecting two points. This diagrammatic representation gives an easier interpretation of the non-vanishing contributions to the average. In particular, for the denominator the only non vanishing contributions correspond to those bonds forming a closed pattern (as shown in Fig.1.1) of the form:

$$\int_0^{2\pi} d\theta_P e^{i(\theta_P - \theta_P)} = 2\pi \tag{1.9}$$

---

[1]More generally in a two-dimensional system with a continuous symmetry and short-range interactions.
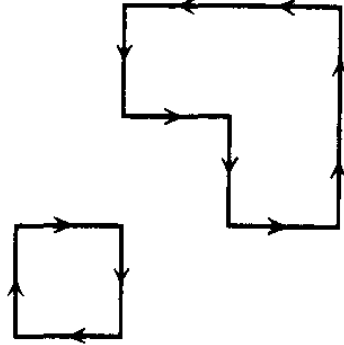
Figure 1.1. Diagrams leading to a finte contributions in (1.8).

For the numerator of (1.8), the argument is the same except the additional factor $\cos(\theta_1 - \theta_2)$.

Hence, in this case the finite contributions will come only from those paths connecting point 1 and point 2. Focusing on the case in which these two points are far enough from each others, the number of steps needed to connect them will be $n \sim |\mathbf{r}_1 - \mathbf{r}_2|$, with $n!$ different ways to build up such connection. The correlation function then will be:

$$C(\mathbf{r}_1 - \mathbf{r}_2) \simeq (\frac{\beta J}{2})^n \simeq (\frac{\beta J}{2})^{|\mathbf{r}_1 - \mathbf{r}_2|} = e^{[-\ln(\frac{2}{\beta J}) \cdot |\mathbf{r}_1 - \mathbf{r}_2|]} \tag{1.10}$$

Hence, in the high-temperature regime the correlation functions of the model decay exponentially with the distance, as in a typical disordered system:

$$C(\mathbf{r}_i - \mathbf{r}_j) \simeq e^{-|\mathbf{r}_1 - \mathbf{r}_2|/\xi} \tag{1.11}$$

where we have introduced the correlation length:

$$\xi = \frac{1}{\ln(\frac{2T}{J})} \tag{1.12}$$

From (1.12), we can see that ξ increases as the temperature decreases, without any divergence at finite T.

On the other hand if we compute the correlation functions in the low-temperature regime, we will find a completely different trend.

In this case we can use the same approximations used above for the calculation of the order parameter (1.2), so that the calculation of the correlation function (1.7) reduces to a simple Gaussian average:

$$C(\mathbf{r}) = \langle e^{i(\theta(\mathbf{r}) - \theta(0))} \rangle = e^{-\frac{1}{2}\langle [\theta(\mathbf{r}) - \theta(0)]^2 \rangle} \tag{1.13}$$

Computing the exponent in the Fourier space, we get:

$$\langle[\theta(\mathbf{r}) - \theta(0)]^2\rangle = \langle \int \frac{d\mathbf{q}_1}{2\pi} \theta_{\mathbf{q}_1}(e^{i\mathbf{q}_1\mathbf{r}} - 1) \int \frac{d\mathbf{q}_2}{2\pi} \theta_{\mathbf{q}_2}(e^{i\mathbf{q}_2\mathbf{r}} - 1)\rangle =$$

$$= \int \frac{d\mathbf{q}}{(2\pi)^2}(2 - 2\cos(\mathbf{q}\cdot\mathbf{r}))\langle|\theta(\mathbf{q})|^2\rangle =$$

$$= \frac{T}{\pi J}\Big[\int_{1/L}^{1/a} \frac{dq}{q}(1 - \cos(\mathbf{q}\cdot\mathbf{r}))\Big] \sim \frac{T}{\pi J}\int_{1/r}^{1/a} dq\frac{1}{q} = \frac{T}{\pi J}\ln(\frac{r}{a}) \tag{1.14}$$

Finally, substituting it in (1.13):

$$C(\mathbf{r}) = e^{-\frac{T}{2\pi J}\ln(r/a)} = \left(\frac{a}{r}\right)^{\frac{T}{2\pi J}} \tag{1.15}$$

In the low-temperature regime, as in the high-temperature one, the correlation functions decay to zero for large distance. However, in this case the decay is much slower respect to the exponential one found in the high-temperature case (1.11). The low-temperature power-low decay, in terms of correlation length (1.12) has the meaning of: $\xi \to \infty$. Between the two regimes a drastic change of the correlation functions occurs, strongly indicating the presence of a phase transition despite the lack of order at any finite temperature.

At that time, other hints to the presence of a phase transition were some experimental works[54] on ^4He, showing a discontinuous jump to zero of the superfluid density for a finite value of the temperature. As we will see in the following, both superfluid and superconducting films belong (for the superconducting case, only when films are thin enough to overcome the screening of charged supercurrent, as we will see below) to the same universality class of the XY model. Hence a discontinuous drop of the superfluid density, that in terms of the spins model corresponds to the spin stiffness [2] J_s, was the second strong signal of the occurrence of a phase transition.

1.4 The role of vortices

The answer to the puzzling problem of putting together the presence of a phase transition, with the lack of a spontaneous symmetry breaking, is embedded in the discrete and local symmetry of the Hamiltonian (1.1)

$$\theta_i \to \theta_i \pm 2\pi m \tag{1.16}$$

with $m \in \mathbb{Z}$. Indeed, this invariance leads to the possible formation within the system of a new class of spin excitations, very different from the *smooth* spin wave excitations coming from the continuous symmetry of the model. They are *new* spin excitations, called vortices, have a topological nature and are characterised by a winding of the phase by $\pm 2\pi m$, around their center:

$$\oint \nabla\theta \cdot d\ell = 2\pi m \tag{1.17}$$

---

[2]It is the energetic cost to induce a twist of the phase. At zero temperature it corresponds just to the coupling constant J.

where m represents the vorticity number of the vortex itself. Precisely because of their *uneveness*, vortices excitations were soon recognized by Berezinskii, Kosterlitz and Thouless as good candidates to be responsible for the phase transition occurring in the model. The first attempt of Kosterlitz and Thouless[2], and also one of the smartest idea in the study of this peculiar transition, was to look at the cost, in terms of free energy, of an isolated free vortex of unitary vorticity.

To make this estimate, we would like to rewrite the Hamiltonian (1.1), separating the vortices contribution from the spin waves one, keeping at the same time the continuum notation for $\theta(\mathbf{r})$. Following[55][56][43], we can think to add an additional term to the Gaussian approximated Hamiltonian (1.2), that otherwise would account only for smooth spin waves excitations. Let us write the Hamiltonian in terms of a phase current $\mathbf{j}(\mathbf{r})$:

$$H_{XY} = \frac{J}{2} \int d\mathbf{r} \mathbf{j}^2(\mathbf{r}) \tag{1.18}$$

where $\mathbf{j}(\mathbf{r})$ is now the sum of two different contributions:

$$\mathbf{j}(\mathbf{r}) = \mathbf{j}_{\parallel} + \mathbf{j}_{\perp}, \quad \nabla \times \mathbf{j}_{\parallel} = 0, \quad \nabla \cdot \mathbf{j}_{\perp} = 0 \tag{1.19}$$

The longitudinal current $\mathbf{j}_{\parallel} = \nabla\theta_{SW}$ accounts only for the smooth variation of the phase (for $\mathbf{j}_{\perp} = 0$ the Hamiltonian is nothing but (1.2)), while the transverse current $\mathbf{j}_{\perp} = \nabla\theta_V$ accounts for the singular configuration of the phase:

$$\oint \mathbf{j} \cdot dl = \int_S (\nabla \times \mathbf{j}) \cdot ds = \int_S (\nabla \times \mathbf{j}_{\perp}) \cdot ds = 2\pi \sum_i q_i \tag{1.20}$$

where $q_i = \pm m$. Moreover, since the mixed term $\int d\mathbf{r} \mathbf{j}_{\parallel} \cdot \mathbf{j}_{\perp} = 0$ vanishes, we can decouple the Hamiltonian (1.18) as: $H = H_{\parallel} + H_{\perp}$.

With this definition, we can deeply understand where the term *topological* excitations come from. Indeed, from the minimisation of (1.18) one obtains:

- A trivial solution:

$$\nabla^2 \theta_{SW}(\mathbf{r}) = 0 \tag{1.21}$$

- A non-trivial solution in singular points, corresponding to the core of topological defects:

$$\nabla^2 \theta_V(\mathbf{r}_0) = 2\pi m \delta(\mathbf{r} - \mathbf{r}_0) \tag{1.22}$$

Indeed by integrating the phase current around a close contour C enclosing a vortex-configuration one gets:

$$\oint_C d\mathbf{r} \, \nabla\theta_V(\mathbf{r}) = 2\pi m \tag{1.23}$$

The solution of Eq.(1.22) for $m = 1$ in 2D is exactly

$$\theta_V(\mathbf{r}_0) = \arctan\frac{y - y_0}{x - x_0} \tag{1.24}$$

Since $\nabla \theta_V(\mathbf{r}) = (-y/\mathbf{r}^2, x/\mathbf{r}^2)$, the integration of the transverse current along a closed contour enclosing the vortex center is:

$$\oint_C d\mathbf{r}\ \theta_V(\mathbf{r}_0) = 2\pi m \tag{1.25}$$

Finally, thus the energy of a single isolated vortex can be easily evaluated:

$$E_V = \frac{J}{2} \int d\mathbf{r}(\nabla \theta_V(\mathbf{r}))^2 = \frac{J}{2} \int_a^L dr\, 2\pi|\mathbf{r}|\frac{1}{\mathbf{r}^2} = \pi J \ln(\frac{L}{a}) \tag{1.26}$$

The energy of a single vortex configuration shows a logarithmic divergence with the system size L: from this perspective, its generation is unlikely in the thermodynamic limit. Nevertheless, at finite temperature we have also to consider the entropic gain in forming such vortex configuration. Given that the number of independent places where a vortex can be place is $\sim (\frac{L}{a})^2$ we obtain:

$$S_V = \ln\left(\frac{L^2}{a^2}\right) = 2\ln\frac{L}{a} \tag{1.27}$$

The entropic term of a single vortex configuration also diverges logarithmically with L. Because of this peculiarity[3] of the two-dimensional XY model, the single-vortex free energy reads:

$$F_V = E_V - TS_V = (\pi J - 2T)\ln(\frac{L}{a}) \tag{1.28}$$

The thermodynamic limit of F_V leads to two different physical situations depending on the the temperature of the system: we can identify a critical temperature T_c above which the entropic term *wins* against the energetic one, promoting the proliferation of free vortices in the system.

$$T_c = \frac{\pi J}{2} \tag{1.29}$$

Such proliferation of free vortices will destroy the *quasi*-long-range order embedded in the power law decay of the correlation functions at low temperature, and it will be responsible for the sudden loss of spin stiffness experimentally observed.

The two principal effects neglected in this simple estimate are: the energetic cost to form a single vortex at the length-scale of the lattice spacing (which in the case of the classical XY model is just a constant in addition to (1.26), hence it does not affect the previous calculation) and the possible presence of vortex-antivortex pairs also below [4] T_c, that can in principle change the "effective" large-distance coupling J of Eq.(1.29). Nonetheless, despite the above estimate (1.28) does not take into account all these effects, the relation between the critical temperature and the (renormalized) stiffness will turn out to be the same as the above Eq.(1.29), as we will see in the next sections.

---

[3]The energetic term has a logarithmic divergence in $L \to \infty$.

[4]If a vortex-antivortex pair arises with the vortex centres in neighboring places at large distances they do not perturb the system, so these configurations are energetically possible also for $T < T_c$.

1.5   Mapping into the 2D Coulomb gas model

In the previous section, we have already shown that the Hamiltonian (1.18) can be written as the sum of two different contributions:

$$H = H_\parallel + H_\perp = \frac{J}{2} \int d\mathbf{r}\, \mathbf{j}_\parallel^2(\mathbf{r}) + \frac{J}{2} \int d\mathbf{r}\, \mathbf{j}_\perp^2(\mathbf{r}) \qquad (1.30)$$

As mentioned before, the first contribution accounts for the spin-wave excitations, while the second one for the topological excitations and their mutual interactions. Let us focus on this last term $H_\perp$, in order to clarify the analogy with the two-dimensional Coulomb-gas model and to put the basis for the renormalization group analysis, addressed in the next section.

The transverse current $\mathbf{j}_\perp(\mathbf{r})$, can be expressed in terms of a scalar field W as:

$$\mathbf{j}_\perp = \nabla \times (\hat{z}W) = (\partial_y W, -\partial_x W, 0) \qquad (1.31)$$

With this definition, Eq.(1.20) reads:

$$\int_S \nabla \times [\nabla \times (\hat{z}W)] = -\int_S d\mathbf{r}\, \nabla^2 W(\mathbf{r}) = 2\pi \sum_i q_i \implies \nabla^2 W(\mathbf{r}) = -2\pi\rho(\mathbf{r}) \quad (1.32)$$

where: $\rho(\mathbf{r}) = \sum_i q_i \delta(\mathbf{r} - \mathbf{r}_i)$. Eq.(1.32) is nothing but the two-dimensional Poisson's equation for the *electric* potential field W generated by a distribution of point-like *charges* q_i at the positions $\mathbf{r}_i$. The general solution of (1.32) is:

$$W(\mathbf{r}) = 2\pi \int d\mathbf{r}'V(\mathbf{r} - \mathbf{r}')\rho(\mathbf{r}') \qquad (1.33)$$

where we have introduced the Coulomb gas potential $V(\mathbf{r})$:

$$\nabla^2 V(\mathbf{r}) = -\delta(\mathbf{r}) \quad \Rightarrow V(\mathbf{r}) = \int \frac{d\mathbf{k}}{(2\pi)^2} \frac{e^{i\mathbf{k}\cdot\mathbf{r}}}{\mathbf{k}^2}, \qquad (1.34)$$

Consequently, we can rewrite $H_\perp$ as:

$$\begin{aligned} H_\perp &= \frac{J}{2} \int d\mathbf{r}\mathbf{j}_\perp^2 = \frac{J}{2} \int d\mathbf{r}(\nabla W(\mathbf{r}))^2 = -\frac{J}{2} \int d\mathbf{r}W(\mathbf{r})\nabla^2 W(\mathbf{r}) = \\ &= \pi J \int d\mathbf{r}W(\mathbf{r})\rho(\mathbf{r}) = 2\pi^2 J \int d\mathbf{r}d\mathbf{r}'\rho(\mathbf{r})V(\mathbf{r} - \mathbf{r}')\rho(\mathbf{r}') = \\ &= 2\pi^2 J \sum_{ij} q_i q_j V(\mathbf{r}_i - \mathbf{r}_j) \end{aligned} \qquad (1.35)$$

Let us look more in details at the 2D Coulomb potential. From Eq.(1.34), one can observe that it shows two divergences: the characteristic infrared divergence at large distances $V(\mathbf{r} \gg a) \sim -\ln(\mathbf{r})$, and the ultraviolet divergence at very short distance $V(\mathbf{r} \to 0)$[5]. The infrared divergence requires the constraint of charge neutrality within the system, removing at the same time the ultraviolet divergence as well. In

---

[5]Since in the thermodynamic limit: $V(\mathbf{r} = 0) = \int_{1/L}^{1/a} \frac{d|\mathbf{k}|}{(2\pi)^2}|\mathbf{k}|^{-1} = \frac{1}{(2\pi)^2}\ln(\frac{L}{a}) \xrightarrow[L\to\infty]{} \infty$

order to clarify what has been said, let us write the Coulomb potential separating the divergent term in $\mathbf{r} = 0$ from the rest:

$$V(\mathbf{r}_i - \mathbf{r}_j) = V(0) + G(\mathbf{r}_i - \mathbf{r}_j) \tag{1.36}$$

where now the second term is a regular function in zero $G(0) = 0$, which accounts for the charges (vortices) interaction distant $\mathbf{r}$ from each other. Substituting (1.36) in (1.35), the Hamiltonian $H_\perp$ reads:

$$H_\perp = 2\pi^2 J \sum_{ij} q_i q_j [V(0) + G(\mathbf{r}_i - \mathbf{r}_j)] =$$
$$= 2\pi^2 J V(0) \left(\sum_i q_i \right)^2 + 2\pi^2 J \sum_{ij} q_i q_j G(\mathbf{r}_i - \mathbf{r}_j) \tag{1.37}$$

Being the last term of the above equation (1.37), almost equal to $\sim \sum_i q_i \sum_j q_j \ln(r_{ij})$ at large distance, if the neutrality condition:

$$\sum_i q_i = 0 \tag{1.38}$$

was not fulfilled, in the thermodynamic limit it would diverge as $\sim L^2 \ln(L)$, instead of diverging only with the volume as expected for energy. With this constraint, also the divergent term $V(0)$ is automatically removed. It is worth to highlight that while the charge neutrality condition (1.38) is strictly required to fix the infrared divergence of the Coulomb potential, the divergence of $V(0)$ could in principle be fixed differently, by considering for instance spherical charges instead of point-like ones. A second consequence of the above discussion is that one should include a cut-off for the smallest possible distance between two vortices. Starting from the lattice XY model (1.1) a natural cut-off is provided by the lattice spacing a in the original model. The interaction potential $G(\mathbf{r})$ can be then obtained from:

$$G(\mathbf{r}) = V(\mathbf{r}) - V(0) = \int_{1/L}^{1/a} \frac{d\mathbf{k}}{(2\pi)^2} \frac{(e^{i\mathbf{k}\cdot\mathbf{r}} - 1)}{\mathbf{k}^2} \tag{1.39}$$

for all the distances $\mathbf{r} > a$, it is well approximated by:

$$G(\mathbf{r} > a) \simeq -\frac{1}{2\pi} \ln(\frac{r}{a}) \tag{1.40}$$

While the value of $G(\mathbf{r} = a)$ depends in general on the geometry of the lattice considered, in a square lattice it reads:

$$G(a) = -\frac{1}{4} \tag{1.41}$$

The value of the vortex-interaction at the smallest scale possible $G(\mathbf{r} = a)$ is the so-called *vortex-core energy*: proportional to the value assumed by the interaction at the smallest distance possible, it corresponds to the energetic cost of generating a pair of opposite charges (vortices) within the system. Thus we can write:

$$G(\mathbf{r}) \simeq -\frac{1}{4} - \frac{1}{2\pi} \ln\left(\frac{r}{a}\right) \tag{1.42}$$

Substituting it in Eq.(1.37), with the omission of the term $\propto V(0)$ embedded in the charges neutrality constraint, we get:

$$
\begin{aligned}
H_\perp &= 2\pi^2 J \sum_{i \neq j} q_i q_j G(\mathbf{r}_i - \mathbf{r}_j) = -2\pi^2 J \sum_{i \neq j} \left[\frac{1}{4} + \frac{1}{2\pi} \ln\left(\frac{r_{ij}}{a}\right)\right] q_i q_j = \\
&= -\frac{\pi^2 J}{2} \sum_{i \neq j} q_i q_j - \pi J \sum_{i \neq j} \ln\left(\frac{r_{ij}}{a}\right) q_i q_j = \mu \sum_i q_i^2 - \pi J \sum_{i \neq j} \ln\left(\frac{r_{ij}}{a}\right) q_i q_j
\end{aligned}
\tag{1.43}
$$

where we used $\sum_{i \neq j} q_i q_j + \sum_i q_i^2 = (\sum_i q_i)(\sum_j q_j) = 0$ from Eq.(1.38) and we have finally identified the vortex-core energy μ as

$$\mu = \frac{\pi^2 J}{2} \tag{1.44}$$

Finally, we can use once again the neutrality condition (1.38) by imposing that there are n pairs of vortices of opposite vorticity. Furthermore, since configurations of vortices with a vorticity higher than one are less probable, in the following we will assume $q_i = \varepsilon_i = \pm 1$, $\forall i$. In this way $H_\perp$ reads:

$$H_\perp = 2n\mu - 2\pi J \sum_{i<j}^{2n} \ln\left(\frac{r_{ij}}{a}\right) \varepsilon_i \varepsilon_j, \tag{1.45}$$

The analogy with the two-dimensional neutral Coulomb-gas is now completed. The vortex-core energy μ can indeed be interpreted as the chemical potential conjugated to the number of charges present in the system and the effective value of the XY-model charge can be identified as[6] $q_0^2 = 2\pi J$.

Starting from Eq.(1.45), the first renormalization group (RG) analysis proposed for this model by Kosterlitz and Thouless[2, 3] lied on the physical idea of the dielectric-constant scaling: the Coulomb interaction between a neutral pair of unit charges separated by $\mathbf{r}$, will be screened by the polarisation of smaller pairs separated by less than $\mathbf{r}$ which are screened by even smaller pairs and so on. The original derivation of the *RG* flow[2, 3] was done by integrating out from the partition function the short distance degrees of freedom and by rescaling the cut-off as $a = a_0 e^l$.

In the following years, other renormalization procedures have been used for the study of the BKT transition. The renormalization group procedure proposed by Wilson[57], in which the rescaling is made in momentum space, is particularly easy and transparent for the analysis of the BKT transition when applied to the 1D sine-Gordon model. Indeed, despite it describes a 1D quantum field, its effective dimension is 1(spatial)+1 (temporal) and it belongs to the same universality class of the classical XY model. In the next section, I will briefly review the mapping from the classical 2D Coulomb-gas model to the quantum 1D sine-Gordon one, and afterwards I will present its correspondent RG equations.

---

[6]Despite the dimensionality of this effective charge correspond to the root of an energy, all the physical quantity of the system have the correct physical dimensions. For instance, for the conductivity $\sigma = n_q q_0^2 \mu_q$ this is compensated by the fact that in 2D the density of states does not depend on energy.

1.6   Mapping into the Sine-Gordon model

Starting from Eq.(1.45), let us write the partition function of the Coulomb-gas model, where we must consider all the possible values of n, taking into account that interchanging the n vortices with same vorticity gives the same configuration (so one should divide by a factor $1/(n!)^2$). In conclusion Z_{CG} reads:

$$
\begin{aligned}
Z_{CG} &= \sum_{n=1}^{\infty} \frac{1}{(n!)^2} \int d\mathbf{r}_1 \dots d\mathbf{r}_{2n} e^{-\beta 2 n \mu} e^{2\pi \beta J \sum_{i<j}^{2n} \ln\left(\frac{r_{ij}}{a}\right) \varepsilon_i \varepsilon_j} \\
&= \sum_{n=1}^{\infty} \frac{1}{(n!)^2} y^{2n} \int d\mathbf{r}_1 \dots d\mathbf{r}_{2n} e^{\sum_{i<j}^{2n} 2\pi \beta J \ln\left(\frac{r_{ij}}{a}\right) \varepsilon_i \varepsilon_j}
\end{aligned}
\tag{1.46}
$$

where we introduced the vortex fugacity

$$
y = e^{-\beta \mu}
\tag{1.47}
$$

The explicit derivation of the coulomb-gas partition function Z allows us to recognise easily the analogy with the quantum sine-Gordon model. The model describes a quantum field in 1D $\phi(\mathbf{r}) \equiv \phi(x, v\tau)$ and it is defined by the action:

$$
S_{SG} = \frac{1}{2\pi K} \int d\mathbf{r} \big[(\nabla \phi)^2 - \frac{g}{\pi} \cos(2\phi) \big]
\tag{1.48}
$$

We can treat the first term of the above action as the free part S_0 and we can write the partition function of the model by expanding the exponential of the interacting part in series of powers, so that:

$$
Z_{SG} = \int D\phi \, e^{-S_{SG}} = \int D\phi \, e^{-S_0} \sum_{p=0}^{\infty} \frac{1}{p!} \left(\frac{g}{\pi}\right)^p \cos(2\phi(\mathbf{r}_1)) \dots \cos(2\phi(\mathbf{r}_p))
\tag{1.49}
$$

Decomposing then each cosine term as:

$$
\cos(2\phi(\mathbf{r}_i)) = \frac{e^{2i\phi(\mathbf{r}_i)} + e^{-2i\phi(\mathbf{r}_i)}}{2} = \sum_{\epsilon_i = \pm 1} \frac{e^{2i\epsilon_i \phi(\mathbf{r}_i)}}{2}
\tag{1.50}
$$

we obtain automatically the neutrality condition because for each cosine term there will be both a positive and a negative *charge*: $\varepsilon_i = \pm 1$. We can now compute the gaussian integral $\int D\phi \, e^{-S_0} \dots$, that we will indicate with $\langle \dots \rangle$, for each of these exponentials:

$$
\begin{aligned}
\langle e^{2i \sum_i \epsilon_i \phi(\mathbf{r}_i)} \rangle &= e^{-2\langle [\sum_i \epsilon_i \phi(\mathbf{r}_i)]^2 \rangle} = \\
&= e^{-2 \sum_i \epsilon_i \sum_j \epsilon_j \langle \phi(\mathbf{r}_i) \phi(\mathbf{r}_j) \rangle} = e^{2K \sum_{i<j} \ln\left(\frac{r_{ij}}{a}\right) \varepsilon_i \varepsilon_j}
\end{aligned}
\tag{1.51}
$$

where we have used again the well know properties of Gaussian integrals. To complete the mapping, we need to consider the multiplicity of a configuration made by $p = 2n$ charges, whose global charge is zero. Such multiplicity is just the number of way in which we can choose n positive ε_i among the total $2n$. So it is just:

$\binom{2n}{n} = (2n)!/(n!)^2$. Adding this prefactor to Eq.(1.49) we complete the mapping with 2D Coulomb gas model:

$$Z_{SG} = \sum_{n=1}^{\infty} \frac{1}{(n!)^2} \left(\frac{g}{2\pi}\right)^{2n} \int d\mathbf{r}_1 \ldots d\mathbf{r}_{2n} e^{2K \sum_{i<j}^{2n} \ln\left(\frac{r_{ij}}{a}\right)\varepsilon_i \varepsilon_j} \tag{1.52}$$

Finally, identifying:

$$K = \quad \frac{\pi J}{T}, \tag{1.53}$$

$$g = \quad 2\pi e^{-\beta \mu} \tag{1.54}$$

the mapping between the sine-Gordon model and the 2D Coulomb-gas model is completed. So, even if these two models describe completely different physical systems, they both belong to same class of universality of the XY model admitting the same transition: the BKT transition.

1.7   RG equations

To complete our analysis on the XY model, by means of the mapping with the sine-Gordon model, we want to look how the system behaves for a given temperature, under coarse graining. The usual procedure is to change gradually the cutoff of the system, varying at the same time the coupling constant (and possibly also generating new coupling constants) in order to keep the low-energy properties of the system unchanged. As mentioned above there are different ways to carry on this calculation, in this section we will present the RG equations derived by means of the Wilson-like procedure, i.e. by progressively rescaling the upper cut-off Λ of the momenta space:

$$\begin{aligned} K(\Lambda) &\to K(\Lambda') \\ g(\Lambda) &\to g(\Lambda') \end{aligned} \tag{1.55}$$

where Λ is the original upper cut-off and $\Lambda' < \Lambda$ the new one. The way in which they modify by iterating such rescaling, will give us the renormalization group flow of the system itself. Addressing the reader to[58] for the complete derivation, we just present the resulting RG flow for the sine-Gordon model, with the usual parametrisation $\Lambda(l) = \Lambda_0 e^{-l}$, $l = \ln(\frac{a}{a_0})$:

$$\frac{dK}{d\ell} \quad = -K^2 g^2, \tag{1.56}$$

$$\frac{dg}{d\ell} \quad = (2 - K)g. \tag{1.57}$$

The spin stiffness is then identified[32] by the limiting value of K in the thermodynamic limit:

$$J_s \equiv \frac{TK(l \to \infty)}{\pi} \tag{1.58}$$

From (1.56)-(1.57), we can immediately recognise two main regimes of the model corresponding to: $K \gtrsim 2$, region (A) in Fig.1.2, and $K \lesssim 2$, region (B) in Fig.1.2.

In the first regime, the term on the right side of (1.57) is negative so that $g \to 0$, while K tends to a finite value $K \to K^*$. According to (1.58), thus, in this regime the system shows a finite spin-stiffness, while the role of the vortices, because of the vanishing of g, is irrelevant. On the contrary, when $K \lesssim 2$ the vortex fugacity g grows under coarse graining leading to the vanishing of K. Hence, the spin stiffness $J_s \to zero$ in this regime. In Fig.1.2, the resulting lines of the *RG* flow (1.56)-(1.57) are plotted in the $K - g$ plane. Each line corresponds to a different value of T.

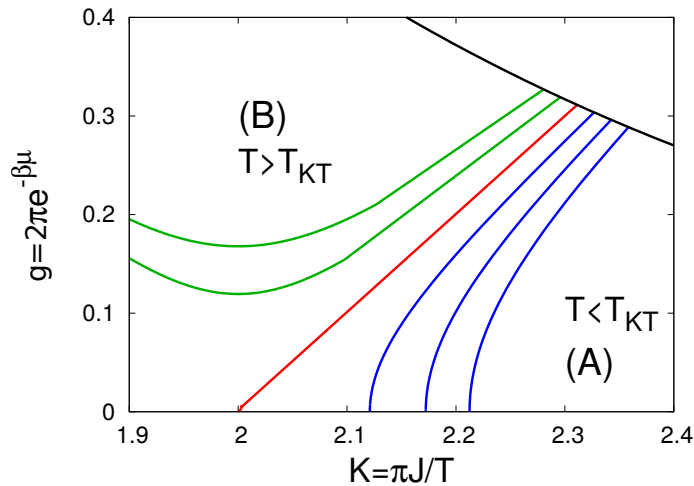In the XY model, as we already know, the two couplings at play are the spin stiffness

Figure 1.2. RG flow in the $K - g$ planes for the BKT transition.

J_s, and vortex-core energy μ, related to K and g through Eq. (1.53) and (1.54). However, the bare value of the vortex-core energy μ, before getting renormalized by the *RG* flux, is simply $\frac{\pi}{2}J$. Consequently the initial value of the coupling g_0, indicated with the black curve in Fig.1.2, is:

$$g_0 = 2\pi e^{-\beta\mu} = 2\pi e^{-\frac{1}{2}\beta\pi^2 J} = 2\pi e^{-\frac{\pi}{2}K(T)} \tag{1.59}$$

Notice that the bare value of K is temperature dependent, so that to each temperature corresponds a single point on the curve g_0, from which the renormalization flow starts. From Eq.(1.53), we also know that if we move on the black curve of Fig.1.2 from right to left, we are increasing the temperature (inversely proportional to K). Together with the temperature increase, as we have just discussed the *RG* flow change qualitatively behavior passing from the low-temperature region to the high-temperature one. The red line in between the two regimes is nothing but the critical line, related to the BKT critical temperature. Indeed it corresponds to the highest value assumed by the temperature before the coupling K flows to zero.

The sudden loss of spin rigidity is embedded in this change of flow, that let the spin stiffness J_s pass sharply from a finite value to zero. Moreover, the *last*-finite value of J_s, before its jump to zero, can be computed exactly looking at the *red-line RG* flow of Fig.1.2: starting from $g_0(T_{BKT})$ the line ends to the critical point $K = 2$, $g = 0$ which defines the universal relation between J_s and T_{BKT}:

$$K(T_{BKT}) = 2 \implies \frac{\pi J_s(T_{BKT})}{T_{BKT}} = 2 \tag{1.60}$$

As already said, as soon as one goes to temperature larger than T_{BKT}:

$$K(T_{BKT}^+) = 0 \implies J_s(T_{BKT}^+) = 0 \tag{1.61}$$

the system suddenly lostes its rigidity because of free vortices proliferation within the system.

Despite the power of this analysis, it is important to highlight that the *RG* equations (1.56)-(1.57) account only for the effects of vortex excitations. We have indeed neglected the effects of the spin-wave excitations coming from higher orders of the cosine expansion in (1.1), which nevertheless contribute, as the temperature increases, to a linear depletion of the spin stiffness. To derive the temperature dependence of J_s at low T, let us go beyond the Gaussian approximation of the original XY Hamiltonian (1.1):

$$H_{xy} = -J \sum_{<i,j>} \cos(\theta_i - \theta_j) \simeq \frac{J}{2} \sum_{<i,j>} [(\theta_i - \theta_j)^2 - \frac{1}{12}(\theta_i - \theta_j)^4 + \dots] \tag{1.62}$$

As usual, to allow for a simpler analytical treatment we approximate finite differences with gradients in the long-wavelength limit, so that:

$$H_{xy} \simeq \frac{J}{2} \int d\mathbf{r} \Big[(\nabla\theta(\mathbf{r}))^2 - \frac{1}{12} \sum_{\alpha=x,y} \Big(\frac{\partial\theta}{\partial\alpha}\Big)^4 + \dots \Big] \tag{1.63}$$

At low temperature, the corrections to the spin stiffness come from the fourth order term and they can be computed with perturbation theory respect to the Gaussian term:

$$\frac{1}{12} \sum_{\alpha=x,y} \Big(\frac{\partial\theta}{\partial\alpha}\Big)^4 \simeq \frac{1}{2} \Big[\langle\Big(\frac{\partial\theta}{\partial x}\Big)^2\rangle \Big(\frac{\partial\theta}{\partial x}\Big)^2 + \langle\Big(\frac{\partial\theta}{\partial y}\Big)^2\rangle \Big(\frac{\partial\theta}{\partial y}\Big)^2 \Big] = \frac{1}{4}(\nabla\theta)^2 \langle(\nabla\theta)^2\rangle \tag{1.64}$$

Finally we can rewrite Eq.(1.63) as:

$$\begin{aligned} H_{xy} &\simeq \frac{J}{2} \int d\mathbf{r} (\nabla\theta(\mathbf{r}))^2 \Big[1 - \frac{1}{4}\langle(\nabla\theta)^2\rangle \Big] = \\ &= \frac{J}{2} \int d\mathbf{r} (\nabla\theta(\mathbf{r}))^2 \Big[1 - \frac{T}{4J} \Big] = \frac{J(T)}{2} \int d\mathbf{r} (\nabla\theta(\mathbf{r}))^2 \end{aligned} \tag{1.65}$$

An easy way to include this effect in the *RG* equations, is to choose as bare value of the spin stiffness the temperature-dependent expression we have just derived: $J(T) = J - \frac{T}{4}$. The resulting temperature dependence of $J_s(T)$, obtained with this procedure, is shown in Fig.1.3.

As one can see, as one approaches the transition J_s is slightly smaller than J: this is due to the difference between the initial value of K and its limiting value $K^* = K(\ell = \infty)$ under the RG flow. Such a difference is practically zero at $T \ll T_{BKT}$ where the RG flow is almost vertical. However as T approaches T_{BKT} vortices renormalize at short distances the superfluid density with respect to its bare

value, but still J_s is finite, because at large distances vortices disappear effectively from the system. For this reason one must be very careful in defining what is universal: T_{KT} is *not* universal, what is universal in the relation between the *renormalized* superfluid density and the transition temperature, as encoded in Eq.(1.60). In other words, as shown by Nelson and Kosterlitz in[32], what characterised the BKT transition is the *universal jump* of the superfluid stiffness, occurring as soos as it becomes equal to: $J_s(T_{BKT}) = 2T_{BKT}/\pi$. In the following, we will refer to it also as the *Nelson-Kosterlitz* (universal) jump.
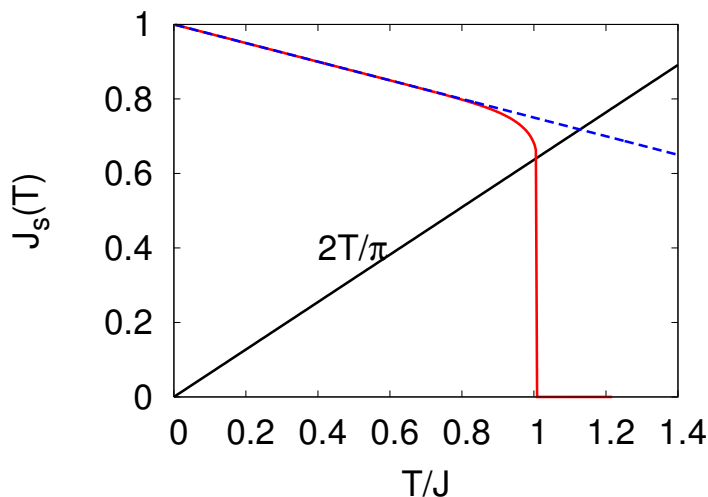
Figure 1.3. Temperature dependence of the spin stiffness $J_s(T)$ obtained via the RG flow, having used as bare value for J: $J(T) = J - T/4$, as indicated by the dashed blue line.

This procedure can be used to include also other effects that can come into play in the low temperature trend of J_s. For instance, for the case of superconducting films, as we will see afterwards, one can include in the bare expression of $J_s(T)$ also the effects due to quasiparticle excitations, reducing further its initial value.

Finally, it is worth spending still some time on the *RG* equations (1.56)-(1.57) to derive the expression of the correlation length ξ close to the BKT critical point. Let us start with a convenient change of variables:

$$x = K - 2 \tag{1.66}$$
$$y = 2g \tag{1.67}$$

the *RG* equations with this choice read:

$$\frac{dx}{dl} = -(x+2)^2 \frac{y^2}{4} \simeq -y^2 \tag{1.68}$$
$$\frac{dy}{dl} = -xy \tag{1.69}$$

having expanded around the fixed point $x = 0$, $y = 0$. We can easily solve these differential equations noticing that:

$$x\frac{dx}{dl} - y\frac{dy}{dl} = 0 \tag{1.70}$$

whence:

$$x^2 - y^2 = A^2 \tag{1.71}$$

Eq.(1.71) is nothing but the *RG* flow, close to the critical point, in the new $x - y$ plane. The resulting flow lines are hyperbola, whose symmetry axis can be: $y = 0$ if $A^2 > 0$ (equivalent to green lines in the region (B) of Fig.1.2) or $x = 0$ if $A^2 < 0$ (region (A) of Fig.1.2). The critical line corresponds obviously to $A^2 = 0$. Approaching the critical point $A \to 0^+$, Eq.(1.68), can be rewrite as:

$$\frac{dx}{dl} = -x^2 \tag{1.72}$$

whose solution is:

$$x = \frac{1}{l + c} \tag{1.73}$$

where c is a constant connected with the initial value of the RG flow l_0 and $x(l_0)$. The regime $A^2 > 0$, thus corresponds the low-temperature region with finite spin stiffness and vanishing g. Indeed, by substituting $x^2 = y^2 + A^2$ in (1.69), we get a first-order differential equation for y:

$$\frac{dy(l)}{dl} = -y\sqrt{y^2 + A^2} \tag{1.74}$$

whose solution gives:

$$y(l) = \frac{A}{\sinh(Al + \text{arcsinh}(\frac{A}{y_0}))} \xrightarrow[l \to \infty]{} 0 \tag{1.75}$$

On the other hand, following the same procedure, the solution for x will be:

$$x(l) = \frac{A}{\tanh(Al + \text{arcsinh}(\frac{A}{y_0}))} \xrightarrow[l \to \infty]{} A \tag{1.76}$$

Hence, as expected the spin stiffness tends to a finite value, while the coupling accounting for the vortices vanishes under coarse graining.

In order to derive the expression for the correlation length, divergent for $T < T_{BKT}$ (region (B)), we have to look at the other regime where $A^2 < 0$. For simplicity let us introduce another constant C, such that: $-A^2 = C^2 > 0$. After having expressed $y^2 = x^2 + C^2$, we can solve the differential equation (1.68):

$$\frac{dx}{dl} = -(x^2 + C^2) \implies \frac{x}{C} = \tan(-Cl + \arctan(\frac{x_0}{C})) \tag{1.77}$$

The correlation length can then be estimated as the scale l^* at which $x(l^*) = 0$. From (1.77), we have:

$$\arctan(\frac{x}{C}) = cl^* \tag{1.78}$$

Near the transition, we also know that $x_0 \sim y_0$, hence: $C^2 = y_0^2 - x_0^2 = (y_0 - x_0)(y_0 + x_0) \simeq 2y_0(y_0 - x_0)$. However, since approximately $(y_0 - x_0) \simeq \alpha(\frac{T - T_{BKT}}{T_{BKT}})$:

$$C = \alpha\sqrt{t} \tag{1.79}$$

where t is the reduced critical temperature: $t = \frac{T - T_{BKT}}{T_{BKT}}$.

Finally in the limit $t << 1 \rightarrow \arctan(\frac{x_0}{C}) \simeq \frac{\pi}{2}$, hence from Eq.(1.77) we derive that:

$$Cl^* \sim O(1) \implies l^* = \frac{b}{\sqrt{t}} \qquad (1.80)$$

Since $l^* = \ln(\frac{\xi}{a_0})$, we have that:

$$\frac{\xi}{a_0} = e^{b/\sqrt{t}} \qquad (1.81)$$

The parameter b in Eq.(1.81) depends on the specific model studied. In the case of SC films, as shown in details in[55], it is directly connected to the distance $t_c = (T_c - T_{BKT})/T_{BKT}$ between the BCS (mean-field) critical temperature T_c and the BKT one. From this calculation, we have found that approaching the critical point from above the correlation length as an exponential divergence in the reduced critical temperature t (Eq.(1.81)). This peculiar divergence it is well different from the usual power-law divergence observed in ordinary Ginzburg-Landau fluctuations. This is why, as we will see further, the observation of the correlation-length behavior in temperature, close to criticality, is one of the main signature used to distinguish between a BKT transition and a *standard* second-order one.

Chapter 2

BKT transition in superconducting films

From its original formulation[2][3], it was immediately clear that several physical systems belonged to the same class of universality of the 2D *XY* model. The BKT phase transition was expected to occur in two-dimensional magnets, in two-dimensional crystals and also in two-dimensional neutral superfluids. Indeed, despite the differences in the microscopic details of such systems, or even in their quantum or classical character, the fact that they share the same relevant symmetries, space dimension and range of interactions, ensures that they share the same phase transition and critical behavior too. However, it took some years to realise that also superconducting (SC) thin films[59][60][61] belonged to the same *XY* universality class. Nevertheless, nowadays both conventional[8]-[20] and unconventional[62]-[11] superconducting thin films are among the most studied applications of the BKT physics, as well as the object of this PhD Thesis.

In this chapter I will firstly illustrate why the $2D$ XY model is an effective model for superfluid films, afterwards I will discuss under which conditions also charged superfluids (i.e. superconducting films) are well described by the model and finally I will illustrate the three main ways to access experimentally to the specific signatures of BKT physics in SC thin films, highlighting the more recent puzzling problems coming from the experimental results.

2.1 Two-dimensional neutral superfluid

The superfluid transition in $2D$ can be easily described by means of the Gross-Pitaevskii (GP) phenomenological theory[63]-[64]. The superfluid order parameter is assumed to be a complex field defined at each point of the system as:

$$\Psi(\mathbf{r}) = \sqrt{\rho(\mathbf{r})}e^{i\theta(\mathbf{r})} \tag{2.1}$$

being $\rho(\mathbf{r})$ the superfluid mass density (areal density in $2D$) and $\theta(\mathbf{r})$ the phase related to the superfluid velocity:

$$v_s(\mathbf{r}) = \frac{\hbar}{m}\nabla\theta(\mathbf{r}) \tag{2.2}$$

As is known, in three-dimensional systems the superfluid transition is driven by the Bose-Einstein-Condensation (BEC), characterised by a finite value of the order parameter: $\langle\Psi\rangle \neq 0$, which in terms of magnets corresponds to a finite value of the system magnetization. However in $2D$, as we have already stressed, massless Goldstone modes prevent any low temperature condensation. Nevertheless, the superfluid transition still occurs, driven by the emergence of a finite superfluid stiffness within the system. Such transition is nothing but the BKT transition.
The analogy with the XY model becomes even clearer looking at the GP Hamiltonian:

$$H = \int d\mathbf{r} \left(\frac{\hbar^2}{2m} |\nabla\Psi(\mathbf{r})|^2 + V_0|\Psi(\mathbf{r})|^2 + \frac{g}{2}|\Psi(\mathbf{r})|^4 \right) \tag{2.3}$$

Indeed, in terms of mean field solution, taking the modulus of the order parameter to be constant $|\Psi(\mathbf{r})| = \sqrt{\rho(\mathbf{r})} = \sqrt{\rho_0}$, the Hamiltonian (2.3) reduces to:

$$H = \text{const} + \frac{\hbar^2 \rho_0^{2D}}{2m} \int d\mathbf{r} \, (\nabla\theta(\mathbf{r}))^2 \tag{2.4}$$

with $\theta(\mathbf{r})$ taken within the range $[0, 2\pi]$. It is then straightforward to identify the superfluid stiffness as:

$$J_s^{SF} = \frac{\hbar^2 \rho_0^{2D}}{m} = \frac{\hbar^2 \rho_0^{3D} d}{m} \tag{2.5}$$

having substituted $\rho_0^{2D} = \rho_0^{3D} d$, since from the experimental point of view a *two-dimensional* superfluid is a *three-dimensional* superfluid film, whose thickness d is small enough to render any perpendicular superflow negligible.
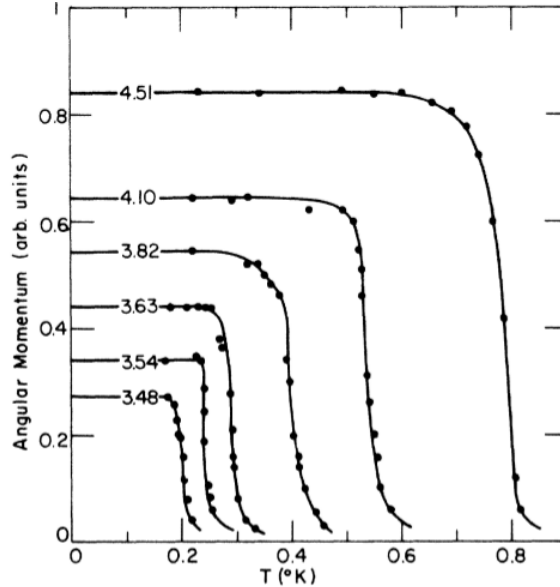
Figure 2.1. [54] Temperature dependence of the persistent current angular momentum of ^4He films for different values of the thickness d. The thickness in the figure is reported in terms of units of 10^{-5} mol m^{-2}.

The most spectacular signature of the BKT transition in real system has been observed for the first time in 1972 [1] (Fig.2.1) and officially published two years later. Using a gyroscopic apparatus, Chan et al.[54] directly measured the angular momentum of the persistent currents formed in thin films of ^4He (absorbed on a porous Vycor glass substrate). The experimental procedure consisted of rotating the system at a standard speed in order to form a persistent current, to cool it and to slowly stop the rotation once reached the lowest temperature accessible ($\sim 150mK$). Finally the temperature was increased again and the angular momentum of the superfluid persistent current was measured at each value of T. The resulting curves, shown in Fig.2.1, revealed the presence of a critical temperature at which the super-fluid film sudden looses its phase rigidity.
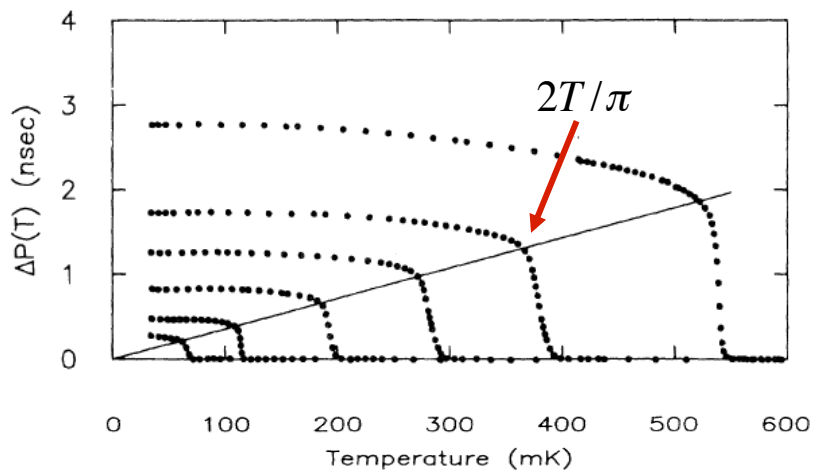
Figure 2.2. [5] Period shift $\Delta P(T)$ of the torsion oscillator for different films of pure ^4He. Each curve corresponds to a different value of the thickness d. $\Delta P(T = 0)$ decreases with d. Finally, the solid line defines the intersection with the superfluid density curves corresponding to the BKT jump prediction (2.6) for the system.

In Figure 2.2, it is shown an other experimental result[5], published some years later the previous one, performed by the use of a torsion pendulum, with which Mc Queeney et al. measured the period shift $\Delta P(T)$ of the superfluid-film rotation respect to the container one. Thus, being $\Delta P(T) \propto J_s^{SF}(T)$, its jump corresponds to the jump of the superfluid stiffness due to the free-vortices proliferation. In particular, repeating the measurements for different values of the film thickness, they stressed the universality relation between the superfluid stiffness and temperature at the BKT critical point:

$$J_s(T_{BKT}) = \frac{\hbar^2 \rho_0^{3D}(T_{BKT})d}{m} = \frac{2T_{BKT}}{\pi} \tag{2.6}$$

The way how the superfluid stiffness exactly jumps to zero at the intersection with the $2T/\pi$ line, for each of the curves plotted, it was really impressive and convincing

---

[1]Just one year before the seminal work of Kosterlitz and Thouless[2].

that they were observing a BKT physics.

2.2   Two-dimensional charged superfluid

The neutral superfluid case is a good starting point for the study of the BKT transition in two-dimensional superconductors. At the first sight one could indeed repeat the same procedure as before just recognising the neutral superfluid bosons as Cooper pairs and correspondingly the superconducting order parameter as:

$$\Psi(\mathbf{r}) = |\Delta(\mathbf{r})|e^{i\theta(\mathbf{r})} \tag{2.7}$$

where the amplitude $\Delta(\mathbf{r})$ is proportional to the SC gap, while $\theta(\mathbf{r})$ is the phase of the condensate. The phenomenological theory for superconductors, as the Gross-Pitaevskii for superfluids, is the Landau-Ginzburg[65] one, whose free energy reads:

$$F = \int d\mathbf{r} \left(\frac{\hbar^2}{4m}|\nabla\Psi(\mathbf{r})|^2 + \alpha|\Psi(\mathbf{r})|^2 + \frac{\beta}{2}|\Psi(\mathbf{r})|^4 \right) \tag{2.8}$$

where α depends on temperature as: $\alpha \propto (T - T_c^0)/T_c^0$, being T_c^0 the mean field transition temperature, while β is a temperature-independent coefficient which stems on the specific material. For fixed and finite amplitude: $\Psi = \Delta_0 e^{i\theta}$ Eq.(2.8) reduces to:

$$F = \int d\mathbf{r} \frac{\hbar^2 \rho_s}{8m} \Big(\nabla\theta(\mathbf{r})\Big)^2 + const \tag{2.9}$$

where we identified:

$$\frac{-\alpha}{\beta} = \frac{\rho_s}{2} \tag{2.10}$$

for the analogy with the bosons case. Thus:

$$\frac{\hbar^2 \rho_s}{4m} = \frac{\hbar^2 \rho_s^{3D} d}{4m} \equiv J_s^{SC} \tag{2.11}$$

is the corresponding XY-model spin stiffness for the superconducting case, perfectly equivalent to Eq.(2.5). As we will see below, the superfluid stiffness is proportional to the inverse London's penetration length λ^{-1}. The relation between ρ_s and λ arises by the need of having a SC-condensate phase rigidity for the expulsion of the magnetic field within the system: without a global phase rigidity the electromagnetic field cannot become massive and the system will not show any Meissner effect.
We can derive the dependency between ρ_s and λ introducing, via the minimal substitution, a finite magnetic field in Eq.(2.9):

$$F = \int d\mathbf{r} \, \frac{\rho_s}{8m} \Big(\hbar \vec{\nabla}\theta(\mathbf{r}) - \frac{2e}{c}\vec{A(\mathbf{r})} \Big)^2 + \frac{(\vec{\nabla}\times\vec{A})^2}{8\pi} \tag{2.12}$$

Looking just at the terms in $\vec{A}$ of Eq.(2.12):

$$\delta F(A) = \int d\mathbf{r} \, \frac{1}{8\pi}\Big[\frac{4\pi e^2}{mc^2}\rho_s \vec{A}^2 + (\vec{\nabla}\times\vec{A})^2 \Big] = \int d\mathbf{r} \, \frac{1}{8\pi}\Big[\frac{1}{\lambda^2}\vec{A}^2 + (\vec{\nabla}\times\vec{A})^2 \Big] \tag{2.13}$$

by taking the minimum of Eq.(2.13), we can recognise the London's equation:

$$\nabla^2 \vec{A} = \frac{1}{\lambda^2}\vec{A} \quad \text{where:} \quad \lambda^{-2} \equiv \frac{4\pi e^2 \rho_s}{mc^2} \tag{2.14}$$

The λ dependency on ρ_s tells us what already mentioned: the more rigid the system is, the smaller will be the magnetic field penetration depth.

However, in the picture given so far, we have omitted at least two fundamental differences with respect to the case of neutral bosons:

1. the temperature dependece of $|\Delta_0|$

2. the charge carried by Cooper pairs

First of all, in a superconducting film, since the bosons are indeed Cooper pairs they can split in pairs of fermions with the increase of the temperature. Such quasiparticles excitations occur already below T_{BKT}, where the vortices unbinding takes place. As a consequence, before the Nelson-Kosterlitz universal jump, the superfluid stiffness will have a *BCS*-like behavior. Thus for $T < T_{BKT}$ and $T \simeq T_c^0$[66]:

$$\rho_s = |\Delta_0|^2 \propto t \tag{2.15}$$

being t the reduced critical temperature respect to the mean field critical temperature T_c^0: $t = 1 - \frac{T}{T_c^0}$. As $T \to 0$, the temperature dependence of $\rho_s(T)$ can be computed within BCS theory and its typical temperature dependence for an s-wave SC is sketched in Fig.(2.3).
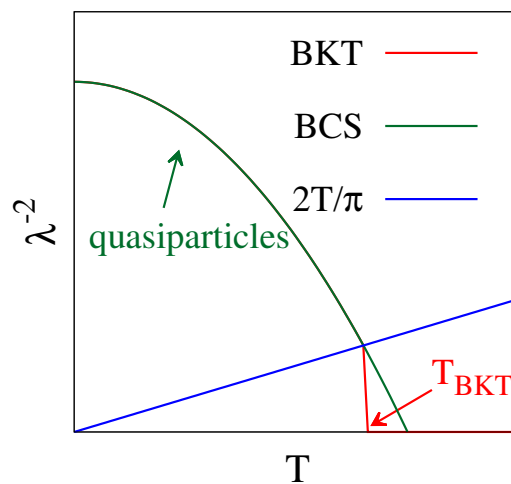
Figure 2.3. Cartoon picture of the superconducting transition in thin films. The superfluid stiffness, proportional to inverse square of the penetration length, is depleted already below T_{BKT} because of quasiparticles excitations.

The second point is more subtle and it is also the reason why in their seminal paper[2] Kosterlitz and Thouless sharply claimed: "*this type of phase transition cannot occur in a superconductor*".
As a matter of fact, the circulating density current around a single vortex screens the

interaction between vortices leading to a non logarithmical inter-vortices potential. As shown by Pearl in[67], in a SC film of thickness $d << \lambda$, with λ the London's penetration length, the force F_{12} between two vortices far apart $\mathbf{r}_{12}$ and of opposite sign reads:

$$F_{12} \simeq \begin{cases} \frac{\Phi_0^2}{\pi} \frac{d}{2\lambda^2} \frac{1}{\mathbf{r}_{12}} & \text{if } \mathbf{r}_{12} << \lambda^2/d \\ \\ \frac{\Phi_0^2}{\pi} \frac{1}{\mathbf{r}_{12}^2} & \text{if } \mathbf{r}_{12} >> \lambda^2/d \end{cases} \quad (2.16)$$

where $\Phi_0 = he/c$ is the quantum flux at the core of the vortex and $\lambda^2/d \equiv \Lambda$ is the so-called Pearl length. Hence, the only way to observe BKT in SC films is to reduce the linear size of the sample at least to Λ: for larger distances the intra-vortices potential will behaves as $\sim 1/\mathbf{r}$ instead of $\sim \ln(\mathbf{r})$ as needed. At the same time, a reduced system size may lead to very strong finite size effects on the phase transition, destroying the analogy to helium films.

However, later on it was realised[61][60][59] that the Pearl length can indeed be quite large in the SC films of interest, especially close to the BKT temperature, making the SC vortices equal (in terms of their mutual interactions) to those developing in helium films. In[59], starting from the universal relation between T_{BKT} and the 2D superfluid density [32]:

$$k_B T_{BKT} = \frac{\pi \hbar^2 \rho_s^{2D}}{8m} = \frac{\pi \hbar^2 \rho_s^{3D} d}{8m} \quad (2.17)$$

an estimation of Λ is given. By means of Eq.(2.14), we can indeed invert the relation in Eq.(2.17), obtaining a direct estimate of the Pearl penetration length at the critical temperature

$$\Lambda(T_{BKT}) = \frac{\hbar^2 c^2}{32 \, e^2} \frac{1}{k_B T_{BKT}} \simeq \frac{0.98}{T_{BKT}(K)} cm \quad (2.18)$$

Such estimate demonstrated that the Pearl length is very large close to the critical point, showing that screening effects are not so serious for T_{BKT} of the order of few kelvin, as it is the case in thin films of conventional SC. With this remark Beasely et al. paved the way to the firsts experimental detection of BKT signature in thin SC films.

2.3 Detection of the BKT phase transition in thin SC films

There are several possibilities to experimentally detect the BKT transition in thin SC films. As we discussed so far, approaching the transition from below[68]-[11] the superfluid density ρ_s is expected to jump discontinuously to zero at the intersection with the critical line[32]. On the other hand, approaching the transition from above one can detect the BKT transition from the temperature dependence of the SC fluctuations[37]-[69]. Indeed, both the paraconductivity $\Delta\sigma = \sigma - \sigma_n$ and the diamagnetism χ_d depend on temperature through the correlation length $\xi(T)$ whose behavior within the BKT physics is very different from the usual GL one. Finally, it is also possible to have evidence of the BKT physics looking at the temperature

dependence of the $I - V$ characteristics. It can indeed be fitted by $V \sim I^{a(T)}$, where $a(T)$ is proportional to the superfluid density of the film.

In this section, I will briefly review the three main experimentally ways to access the specific signatures of the BKT transition.

2.3.1   Paraconductivity measurements

The first attempts to detect the BKT signature in thin SC films focused on the study of the transport properties of the system[59]-[61].

In particular, Halperin and Nelson[61] found that within the BKT physics the SC-fluctuations to the conductivity, the so-called paraconductivity, depend on the SC correlation length ξ as:

$$\frac{\sigma_s}{\sigma_N} \simeq \left(\frac{\xi(T)}{\xi_0} \right)^2 \qquad (2.19)$$

where σ_N is the conductivity of the normal metal. The same dependence was previously found in 1968 by Aslamazov and Larkin[70][71] by a diagrammatic derivation within the Ginzburg-Landau (GL) theory and a year later by Schmidt [72] basing on the time dependent GL theory. Nevertheless, the temperature variation of the correlation length in the two cases is radically different: within the BKT regime approaching the critical temperature from above the correlation length does not diverge with a power-law, as observed in the ordinary Ginzburg-Landau theory where $\xi_{GL}^2 \sim T_c/(T - T_c)$ for $T \rightarrow T_c^+$, but it diverges exponentially as we have seen in Chapter 1:

$$\xi(T) \simeq \xi_0 e^{b/\sqrt{t}}, \quad t = \frac{T - T_{BKT}}{T_{BKT}} \qquad (2.20)$$

Such exponential behavior of the SC-fluctuations constitutes one of the experimental signature of the BKT physics.

Within the BKT theory, as shown in[61], Eq.(2.19) is a direct consequence of the motion of vortices under an applied current. Let us consider a plane of length L along x and width W along y. The finite supercurrent $\mathbf{j}_s$ along x will produce a force (the so-called Magnus force or Lorentz force) moving vortices perpendicularly with respect to it (thus along y), with a direction determined by the vorticity $\varepsilon_i = \pm 1$:

$$\mathbf{f} = \varepsilon_i \mathbf{j}_s \times \hat{z} \frac{\Phi_0}{c} \qquad (2.21)$$

There are several way to derive Eq.(2.21): the easiest is to think that this is just a consequence of the Lorentz force acting on the vortex, due to the magnetic-flux variation caused by the moving current. The movement of vortices along y causes in turn an electric field E_x along x that contrasts the applied current, giving rise to power dissipation to maintain a steady state. In particular, E_x can be estimated as follows: each time a vortex drift across the sample width W, a phase slip of 2π occurs through the sample. The number of vortices that escape the sample in the interval Δt is $n_v v_L \Delta t$, where v_L is the drift velocity of vortices along y. Thus the rate of phase slip is:

$$\frac{d\Delta\theta}{dt} = 2\pi n_v L v_L \qquad (2.22)$$

Thanks to the Josephson relation $\Delta V = (\hbar/2e)d\Delta\theta/dt$, this corresponds to a field $E_x = \Delta V/L$ equal to:

$$E_x = \frac{\Phi_0}{c}n_v v_L \tag{2.23}$$

In the steady state the drift velocity v_L will be simply proportional to the applied Magnus force (2.21), so that

$$\mathbf{v}_L = \mu_V \mathbf{f} = -\varepsilon_i \mu_V \frac{j_s \Phi_0}{c}\hat{y} \tag{2.24}$$

where $\mu_V = D/k_B T$ is the vortex mobility and D is the diffusion constant. In summary, we obtain for the resistivity of the material:

$$\rho = \frac{E_x}{j_s} = \left(\frac{h}{2e}\right)^2 n_v \mu_V \tag{2.25}$$

It is worth noting that Eq.(2.25) is a typical example of duality relation: indeed, the resistivity of the real (electronic) charges is expressed as a "conductivity" of the dual vortex charges $h/2e$, given as usual by the charge squared times the density of charges and their mobility. Eq.(2.25) can be further simplified by using the Bardeen-Stephen[66] expression for the vortex mobility μ_V, derived by an estimate of the dissipation due to the (normal) vortex core:

$$\mu_V = 2\pi\xi_0^2 c^2 \rho_n \Phi_0^2 \tag{2.26}$$

By inserting Eq.(2.26) into Eq.(2.25) one obtains: $\rho = \rho_n 2\pi\xi_0^2 n_V$. Since by definition the vortex density is connected to the SC BKT correlation length via $n_v \equiv 1/2\pi\xi^2(T)$ one finally obtains Eq.(2.19) above. As well discussed in[55], the analysis of the BKT transition based on the paraconductivity data has to deal with the unavoidable lack of knowledge about the exact temperature extension of the BKT fluctuation regime. Usually, in the case of thin SC films, the BKT regime is restricted to a very small range close to T_{BKT}, since in most of the cases the BCS critical temperature T_c is larger, but very close to T_{BKT} as sketched in Fig.2.4.
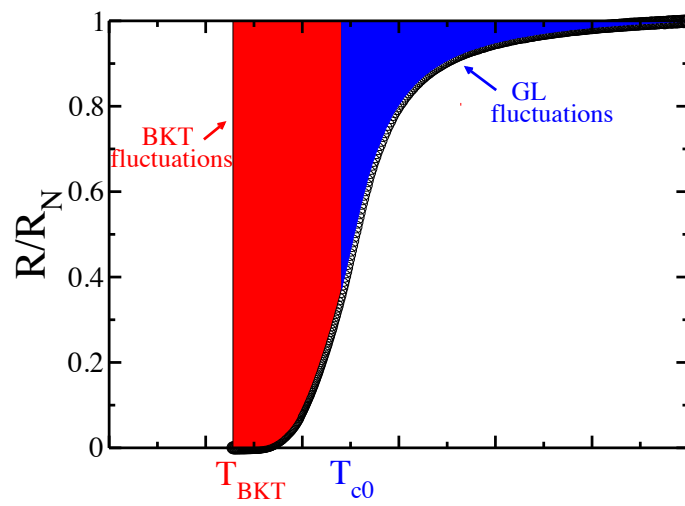
Figure 2.4. Typical temperature dependence of the resistance in 2D SC films. The red area identifies the SC-fluctuation region, which include both the G-L and the BKT fluctuations.

A possible way for the interpretation of the resistivity data is to use the interpolation formula for $\xi(T)$, proposed long ago by Halperin and Nelson[61]:

$$\frac{R}{R_N} = \frac{1}{1 + (\xi(T)/\xi_0)^2}, \qquad \xi(T) = \xi_0 A \sinh(\frac{b}{\sqrt{t}})$$

(2.27)

Eq.(2.27), indeed reduces to ξ_{BKT} for small t and to ξ_{GL} for large t.

Finally in Fig.2.5, we report one of the first paraconductivity measurements by Fiory et al.[73] taken in indium/indium-oxide composite superconducting thin films. As one can see, the interpolation with the theoretical functional form by Aslamov and Larkin fits very well the experimental data up to a certain temperature, corresponding to the temperature at which the regime of the BKT fluctuations starts.
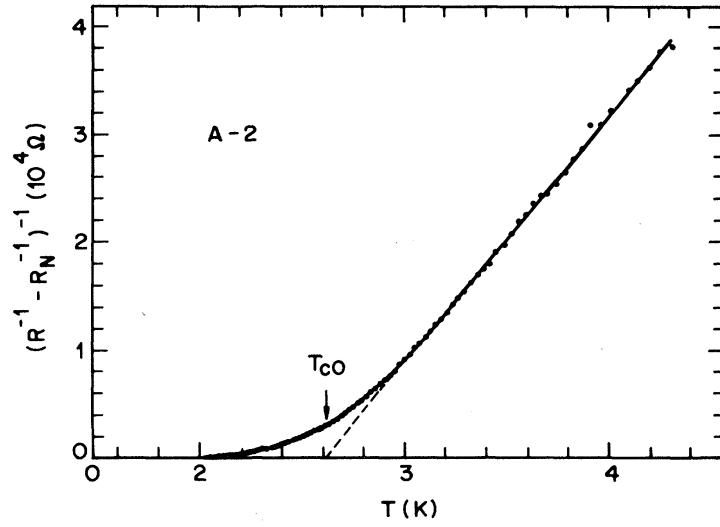
Figure 2.5. [73] Paraconductivity contribution to the resistance measured on a thin film of indium/indium-oxide as function of the temperature. The dashed line is a fit to the Aslamov-Larkin exrpression from which the mean-field critical temperature T_{c0} is extrapolated.

2.3.2 I-V characteristic

Another way to detect the BKT physics through transport measurements is by means of the $I - V$ characteristics. Indeed, a direct consequence of the superfluid-stiffness universal jump (1.60) is the anomalous power-law dependence of the $I - V$ characteristics below T_{BKT}. Let us start from the expression of the energy per unit length of a vortex-antivortex pair at distance r, placed in a films of thickness d. It contains two terms: the logarithmic interaction between the two charges and the Lorentz force (2.21) produced by the presence of a flowing supercurrent in the x direction:

$$\frac{E}{d} = \frac{2\pi J_s}{d} \ln \frac{r}{\xi_0} - \mathbf{f} \cdot \mathbf{r} = \frac{2\pi J_s}{d} \ln \frac{r}{\xi_0} - \frac{I}{Wd} \frac{\Phi_0}{c} r$$

(2.28)

where we wrote the current density through the film as [2] $j = I/Wd$. While the log potential tends to confine the vortices, keeping them bound together, the supercurrent tends to unbind them. There will be then a critical current, above which the vortices separate within the sample. To identify it, let us look at the change of sign of the energy arising when its derivative vanishes, i.e. when $\partial E(r^*)/\partial r = 0$, where:

$$r^* = \frac{2\pi J_s cW}{I\Phi_0} \tag{2.29}$$

since the condition $r^* \geq W$ states when free vortices start to be generated because of the supercurrent action, it follows that the minimum current required to unbind the vortices is the one corresponding to $r^* = W$, so that:

$$I^* = 2\pi J_s \frac{c}{\Phi_0} \tag{2.30}$$

To get en estimate of the critical current near T_{BKT} one can use the universal relation (2.17) to replace $2\pi J_s$ with $4k_B T_{BKT}$ in the previous equation. Then using $c/\Phi_0 = 0.5 10^{15} A/J$ one has:

$$I^*[A] \simeq 2.76 \times 10^{-8} T_{BKT}[K] \tag{2.31}$$

At larger currents one can generate free vortices. To estimate their density n_v one can use a kinetic equation such that:

$$\frac{dn_V}{dt} = \Gamma(T, I) - n_V^2 \tag{2.32}$$

where Γ is the rate at which vortices unbind and can be written as $e^{-E(r^*)/T}$ from the above argument. The second term in Eq. (2.32) accounts for the vortices recombining to form pairs again. In the steady state then one has:

$$n_V = \Gamma^{1/2} = e^{-E(r^*)/2T} \tag{2.33}$$

According to Eq. (2.23) one has that the electric field generated by vortices is proportional to $n_V \times v_L$, where the drift velocity v_L of vortices is proportional again to the applied current I according to Eq. (2.24). We then conclude that:
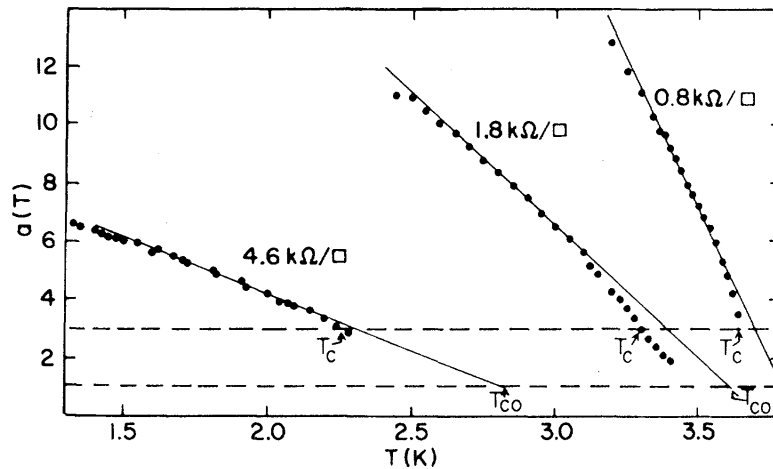
$$V \sim n_V I \tag{2.34}$$

Let us then estimate n_V by means of Eq. (2.33). By using the r^* value (2.29) into Eq. (2.28) we get:

$$E(r^*) = 2\pi J_s \ln \frac{2\pi J_s cW}{\xi_0 \Phi_0 I} - \frac{2\pi J_s c}{d} \tag{2.35}$$

since only the first term depends on the applied current we obtain from Eq.(2.33) that the vortex density scales with the applied current as:

$$n_V = e^{-E(r^*)/2T} \sim e^{-\pi J_s \ln(I^*/I)/T} = \left(\frac{I}{I^*}\right)^{\pi J_s/T} \tag{2.36}$$

Figure 2.6. [74] The exponent $a(T)$ as function of the temperature, obtained from $I - V$ measurements performed on thin $Hg - Xe$ alloy films, for three different values of the sheet resistance. In proximity of the expected BKT jump from $a(T) = 3$ to $a(T) = 1$, one can recognise a broadening of the transition

When replaced into Eq. (2.34) this implies that the non-linear $I - V$ characteristic is controlled by the exponent

$$V \propto I^{a(T)}, \quad a(T) = \frac{\pi J_s(T)}{T} + 1. \tag{2.37}$$

From Eq. (2.17), it follows then that a should jump discontinuously from $a = 3$ at $T = T_{BKT}^-$ to $a = 1$ at $T = T_{BKT}^+$. Below T_{BKT}, the exponent a is expected to increase with decreasing T since the superfluid density increases.

Eq. (2.37) is probably one of the most used way to characterise the BKT transition, even though it should be applied carefully avoiding, for example, to extract the exponent in the high-current regime where the system is near to the other critical current I_c, breaking Cooper pairs instead of exciting vortices.

In Fig.5.8, we report one of the first experimental realisation finalised to the BKT detection via the non-linear $I - V$ characteristic. As predicted, the exponent $a(T)$ jumps from the value $a(T) = 3$ to $a(T) = 1$ at the critical temperature, however the jump looks quite smeared in temperature. As we will see in the following, such broadening is also observed in superfluid stiffness measurements.

2.3.3   Superfluid-density jump

The most direct way to observe the BKT transition is looking at the superfluid-density jump. However, direct experimental measurements of ρ_s in thin SC films became available only recently[37]-[69] thanks to the technical improvements of the late nineties, mostly motivated by the investigation on the high-temperature superconductors.

---

[2]As in the previous section W is the linear size of the film in the y direction

Specifically, one can access the superfluid density probing the system both in the low frequency regime (order of kHz)[18][75] and in the high frequency one (order of GHz)[16]-[76].

Measurements of the superfluid density in the low frequency regime are taken by the use of the two-coils mutual inductance technique[77], which gives access to the absolute value of the London's penetration length λ and with it to the superfluid density of the system. The experimental apparatus used for such measurements is shown in Fig.2.7. The mutual inductance between the two coils is measured as function of the temperature by passing a small ac excitation current, at low frequency $\sim kHz$, to the first coil and then measuring the induced voltage in the second one. The induced voltage will obviously depend on the screening current of the SC film, placed between the two coils, giving thus access to the absolute value of λ. The experimental data of $\lambda^{-2}(T)$ obtained for thin-SC films of NbN are shown in Fig.2.8.
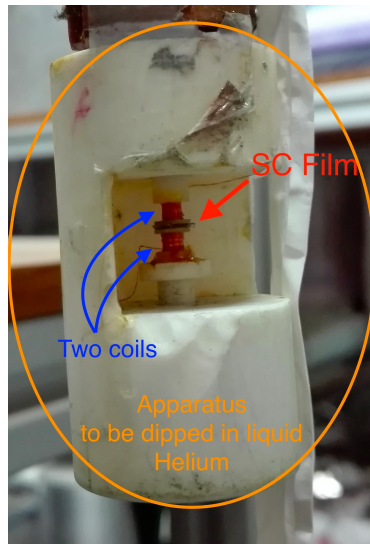

Figure 2.7. Two-coils mutual inductance apparatus. Photo made at the Tata Institute of Fundamental Research in Mumbai.

From these measurements[18], we immediately get the idea how difficult it is to detect the BKT signature:

1. The BKT line has a very low pendency with respect to the $\lambda^{-2}(T)$ scale (Fig.2.8a), leading to a tiny difference between the BCS critical temperature and the BKT one

2. Even zooming in the tiny temperature region of interest (Fig. 2.8b), the superfluid-density jump appears to be completely smeared out around T_{BKT}.

In respect to the first point, from Fig.2.8b it is clear that the film thickness plays an important role: its reduction, suppressing the zero temperature value of λ^{-2}, can make indeed the detection of the jump slightly easier. At the same time, as we will discuss more in detail in the next chapter, the decrease of the film thickness

leads to an increase of the intrinsic disorder, as embedded in the resistivity curves in
Fig.2.8c. This essentially means that the BKT transition in thin-SC films occurs in
the presence of strong disorder, condition that could be responsible for the symmetric
broadening of the jump. I will address this issue to the next three chapters of this
Thesis.
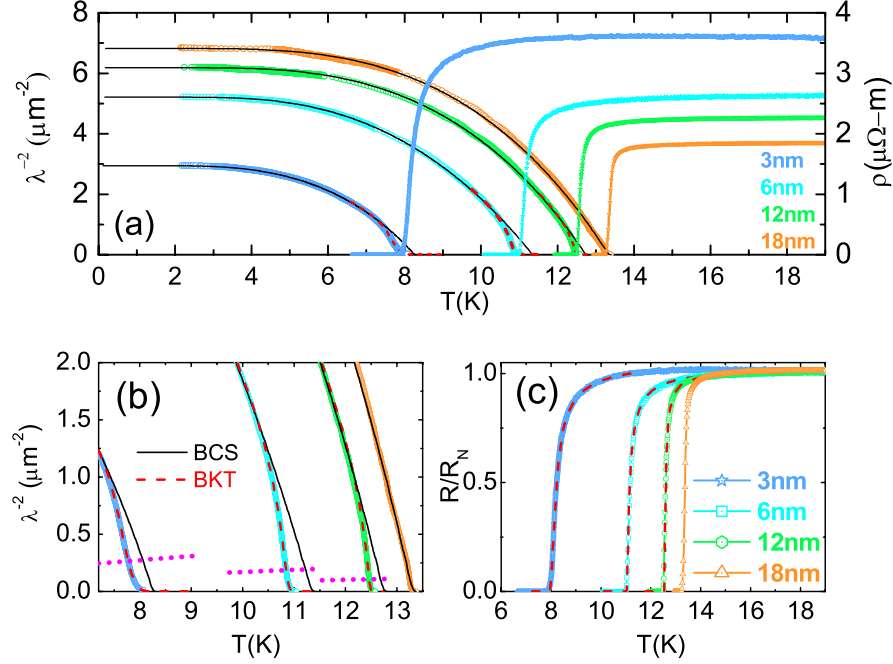
Figure 2.8. [18] (a) Temperature dependence of $\lambda^{-2}(T)$ and $\rho(T)$ for four NbN films with
different thickness. (b) Expanded view of the penetration depth close to the critical
temperature. The pink dotted line is the BKT line, while the black solid line and the red
dashed one correspond to a BCS and a BKT fits. (c) Temperature variation of R/R_N

Another way to detect ρ_s is by means of the electrodynamics response of the SC films
probed via Giga-Hertz spectroscopy[16]-[76]. Indeed the superconducting complex
conductivity $\sigma^S(\omega) = \sigma_1^S(\omega) + i\sigma_2^S(\omega)$ directly depends on the superfluid-carriers
density ρ_s[66]:

$$\sigma_1^S(\omega) = \frac{\pi e^2 \rho_s}{2m}\delta(\omega) + \sigma_{1,\text{reg}}(\omega) \tag{2.38}$$

$$\sigma_2^S(\omega) = \frac{\rho_s e^2}{m\omega} \quad \text{at } \omega \ll 2\Delta \tag{2.39}$$

where $\sigma_{1,\text{reg}}(\omega)$ is nonzero in the presence of disorder. Since for T_c of the order
of few kelvin the SC gap $\Delta \sim 0.1\,THz$, at GHz frequency, $\sigma_2^S(\omega) \cdot \omega$ gives the
superfluid stiffness of the system. In Fig.2.9, the experimental results obtained in[17]
are reported. They probed an amorphous superconducting InO_x thin film using a
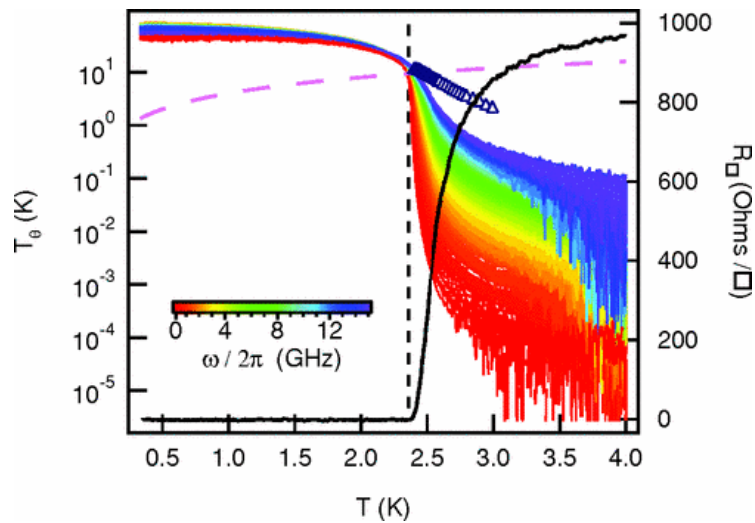microwave Corbino spectrometer, which ranges from 0.21 to 15 GHz.

The superfluid stiffness is here expressed in terms of temperature:

$$k_B T_\theta = 2\pi J_s = \frac{\sigma_2^S(\omega)}{\sigma_Q}\hbar\omega = \frac{\rho_s^{3D}(\omega)de^2\hbar}{4m} \tag{2.40}$$

where $\sigma_Q = 4e^2/h$ is the quantum of conductance for Cooper pairs. The BKT transition is then expected at

$$k_B T_\theta(T_{BKT}) = 2\pi J_s(T_{BKT}) = 4T_{BKT} \tag{2.41}$$

as indicated by the dashed pink curve in Fig.2.9.

Figure 2.9. [17]Temperature dependence of the phase stiffness, expressed as T_θ defined in Eq.(2.40), for different probing frequencies represented by the colour scale. The blue triangles mark the temperature dependence of T_θ^0, i.e. the BCS stiffness without BKT fluctuations obtained via a scaling analysis in[17]. The dashed pink line is the BKT prediction for the universal jump of the superfluid stiffness, while the black curve shows the resistance per square of the system. The experimental results shown here have been obtained through Giga-Hertz spectroscopy measurements on amorphous superconducting InO_x thin films.

The colour scale accounts for the different frequency at which the system has been probed. The probing frequency also defines the effective length scale for the stiffness measurements, which is typically proportional to the vortex diffusion length during a single radiation cycle: $L_\omega = \sqrt{\frac{2\pi\lambda D}{\omega}}$. With the increase of the probing frequency, the finite size effects increase too affecting the temperature regime above the critical temperature. Indeed, looking at the Fig.2.9 the superfluid stiffness jump exhibits for $T > T_{BKT}$ a tail larger and larger as the frequency of the probe increases. On the other hand, the low-temperature regime of the stiffness is almost not affected by finite size effects. In Chapter 4, we will show that the same behavior can be recovered also by means of Monte Carlo simulations on the XY model: the finite size of the system affect the temperature behavior of the stiffness only above T_{BKT}.

2.4 Quasi-2D layered superconductors

Finally, an alternative route for the observation of BKT physics is presented by *bulk* SC systems (Fig.2.10) made of weakly coupled layers. To this category belong the high-temperature (HT) cupratres superconductors, where the superconductivity is expected to be a quasi-2D phenomenon confined to the CuO_2 layers.
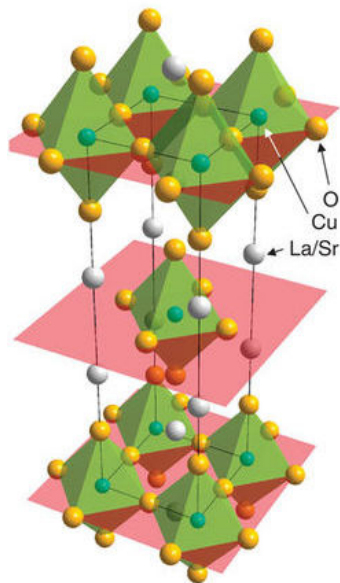
**Figure 2.10.** Crystal structure of the layered cuprate superconductor $La_{2-x}Sr_xCuO_4$ (LSCO).

The reason why BKT physics could be expected is that in the absence of Josephson pairing between planes, the vortex-pair interaction on a single layer is logarithmic up to all length scales[78]. This in principle makes such systems the best possible SC candidates for the detection of the BKT transition. This effect is a direct consequence of the electromagnetic interaction between different layers, which drastically modifies the monopole-like shape of the magnetic-field distribution found by Pearl[67], squeezing the field into a narrow strip of size λ along the $\hat{z}$ direction. On the other hand, in the presence of Josephson coupling, the logarithmic interaction between vortices holds only up to $\Lambda_J \simeq \xi_0 \sqrt{J_\perp/J_\parallel}$, where ξ_0 is the zero-temperature in-plane coherence length, and $J_{\perp,\parallel}$ are the out-of-plane and in-plane zero-temperature superfluid stiffness, respectively. Nevertheless, if the interlayer coupling is weak, i.e. $J_\perp/J_\parallel \ll 1$, this length scale is large enough to allow for a BKT-like description of the vortex-antivortex interaction, independently on the system thickness.[3] Hence, for highly anisotropic systems with a linear size smaller than Λ_J, the mechanism

---

[3]It is worth to highlight that the cutoff Λ_J in layered systems has a completely different meaning respect to the Pearl length Λ for thin films. In this case indeed, exceeding Λ_J the logarithmic interaction is replaced by a linearly increasing potential[78] which leads to the confinement of vortex pairs inducing a $3D$ bulk transition (i.e. into a SC state with a finite order parameter and true off-diagonal long-range order).

driving the transition is expected to be the unbinding of the vortex-antivortex pairs as in the purely 2D case. Among the layered superconductors, underdoped samples of cuprates are particularly indicates for the observation of the BKT transition: they not only show a strong anisotropy between the in-plane and the out-of-plane coupling, but they also have a quite large separation between T_{BKT} and T_c, due to the proximity to the Mott insulators[79]-[80] which suppresses the zero-temperature value of the superfluid-stiffness.

According to this argument, in bulk samples of underdoped cuprates one should be able to identify BKT signatures assuming that the fundamental 2D unit is represented by isolated CuO_2 layers, i.e., the transverse length scale $d \equiv d_{BKT}$ appearing in Eq.(2.14) would coincide with the interlayer distance d_c, as pointed out in the seminal work by Emery and Kivelson [79]. In the late 90s indeed, Corson et al.[81] gave one of the first experimental evidence of the BKT transition in underdoped cuprate, by extracting the superfluid stiffness via high-frequency conductivity measurements as shown in Fig.2.11. As we have seen in Fig.2.9 for the case of InO_x, the curves at different ω separate in correspondence to the BKT line, showing the existence of a BKT fluctuation regime.
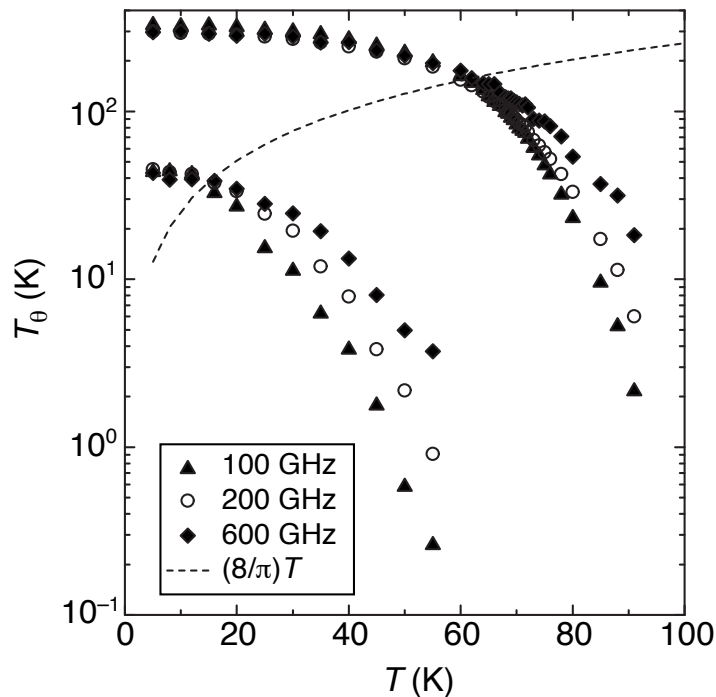


Figure 2.11. [81] Phase stiffness temperature $T_\theta(\omega)$, defined in (2.40), as function of the temperature. Data are shown for two samples, one with $T_c = 33K$ (left side) and the other with $T_c = 74K$ (right side). The three curves for each sample correspond to measurements taken at three different frequencies. Finally, the dashed line is the BKT critical line, at which the superfluid stiffness is expected to jump to zero.

However, as shown in [82] in many cases, this picture is somehow too simplified since one should also account for the nontrivial role of the vortex-core energy μ. Indeed, even if the layers are weakly coupled, what matters for the vortex proliferation is the

competition at large distances between the effective vortex fugacity and the effective Josephson coupling. As a consequence, when μ is large, the Josephson coupling between layers can prevent the vortex unbinding, moving the BKT transition away from the value expected for each isolated layer, resulting in an effective dimension d_{BKT} larger than d_c. This issue has been recently addressed by Baity et al. in [11], revealing an effective thickness of few layers: $d_{BKT} \simeq 2\text{-}3\,d_c$.

Nonetheless, so far the experimental situation in cuprate superconductors is still controversial. For example, the direct measurements of the inverse penetration depth have shown that, in the $YBa_2Cu_3O_{7-x}$ family, no BKT jump is observed even in strongly underdoped thick films [10],[83] or crystals[62]. A BKT-like superfluid-density jump is only seen in few-unit-cell thick films of $YBa_2Cu_3O_{7-x}$ (Ref.[62]) or $Bi_2Sr_2CaCu_2O_{8+x}$ (Ref. [22]), but even in this case, as the samples get underdoped, the superfluid-density jump gets smeared out as shown in Fig.2.12. A possible interpretation of such smearing could come from the increase of the inhomogeneity due to the competing phases, at low doping, between the SC state and the insulating antiferromagnetic one, as shown in the phase diagram in Fig.2.13. Such interpretation would be perfectly in analogy with the presence of strong disorder for the case of thin SC films, as we will see in the next chapters.
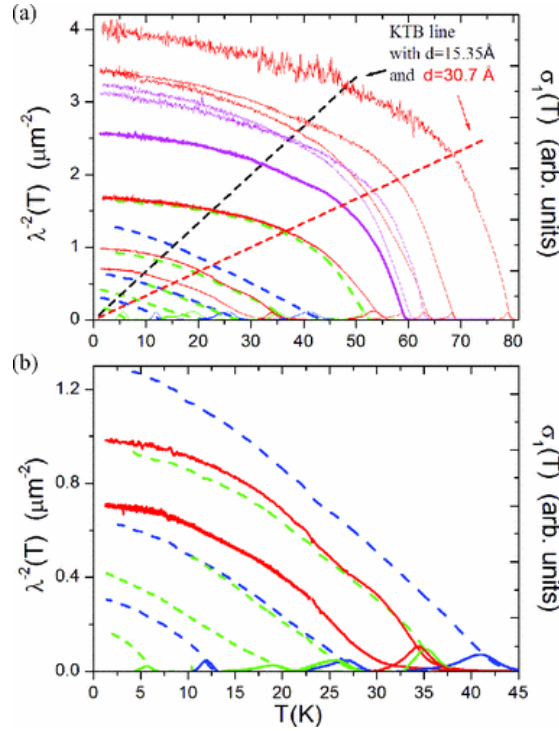
Figure 2.12. [22]Temperature dependence of superfluid density for underdoped $Bi-2212$ films. (a) Full range of dopings. The intersection of the dashed lines with $\lambda^{-2}(T)$ is where Kosterlitz-Thouless theory predicts a downturn in λ^{-2} due to vortex-antivortex unbinding respectively for $d = 15.35$Å, corresponding to one CuO_2 bilayer (black line) and $d = 30.7$Å, two CuO_2 bilayers (red line). (b) Extremely underdoped films with $T_c < 45K$. The widths of the peaks in σ_1 near T_c set an upper limit on the spatial inhomogeneity of T_c.
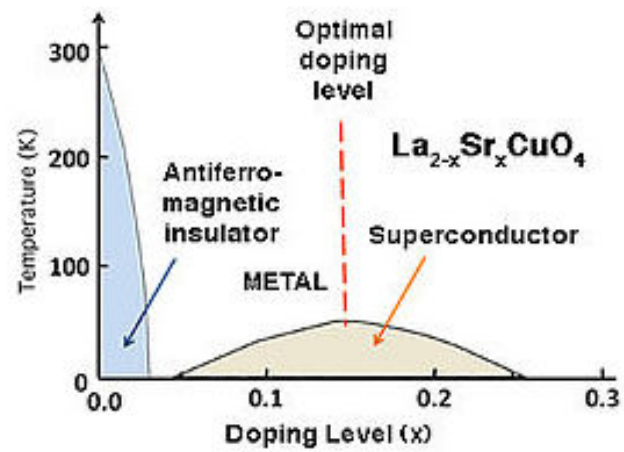
Figure 2.13. LSCO phase diagram as function of the doping.

Chapter 3

Disorder and Inhomogeneity

The study of the BKT transition in thin SC films cannot be addressed without considering the presence of disorder, whose strength is known to increase by reducing the films thickness. Quite interesting, in the last few years it has been proven experimentally[84]-[85] and discussed theoretically[86]-[35] that the competition between SC phase coherence and charge localisation triggered by strong disorder induces an emergent granularity of the SC order parameter in real space, making more appropriate to speak about inhomogeneity than disorder. Such inhomogeneity can be relevant not only for thin films, but also for different classes of 2D SC materials, such as heterostructures[87]-[88] or even for underdoped cuprate superconductors[62]-[22]. In particular, concerning the BKT transition, the study of the effects of the SC-state granularity can be the key ingredient to explain the smooth downturn of the superfluid-stiffness jump experimentally observed.

In fact, as mentioned in the previous chapter, although detailed measurements of superfluid density in thin SC films became available only recently, so far the cases reported in literature both in conventional superconductors[21][9] and high-temperature ones[62][22] never show a really sharp BKT transition. This puzzling issue can not be simply explained in terms of finite-size effects: neither the presence of a finite screening length Λ, nor the finite length L_ω associated to the finite frequency probe, can justify the smearing observed in the experiments. As shown in[56], indeed, introducing a finite cut-off to the BKT-RG equations the rounding effect generated on the stiffness jump is just hardly visible. The same conclusion, as we will see in the next chapter, is also confirmed by means of finite-size Monte Carlo simulations on the classical XY model. The cause of the observed smearing of the superfluid-stiffness jump has to be found then in a different mechanism, and the spatial inhomogeneity of the SC state seems to be the best candidate. Indeed, in the following, we will demonstrate that it really is the reason behind the observed broadening of the BKT transition.

This chapter is addressed both to the experimental observation and to the theoretical modelling of such emergent granularity. In the first section, I will present the resulting SC-state maps in real space obtained by scanning tunnelling spectroscopy in thin films[1], while in the second one I will derive a possible way to model such inhomogeneity by the use of an effective bosons model[36].

---

[1]Similar results have been also obtained in curate superconductors[89].

## 3.1   Disordered thin SC films: experimental results

The interplay between disorder and superconductivity represents a typical example of competing mechanisms. Indeed, as already mentioned, while the former leads to localisation of the electrons and to insulating-like transport, the latter favours the formation of macroscopic coherent electronic state able to sustain dissipationless current. In the low-disorder limit, as postulated by Anderson[90] on the basis of the BCS theory, the pairing mechanism persists almost unchanged as well as the superconducting critical temperature T_c. However, when the disorder increases toward the strong-disorder limit, measurements on a variety of systems register a gradual decrease of T_c, ultimately leading to a full insulating state. To this class of superconductors, showing the superconducting-insulator transition (SIT), belong for instance thin films of NbN, InO_x or TiN. The phase diagram as function of disorder, obtained in[91] via a combination of magnetrotransport and scanning tunnelling spectroscopy (STS) measurements on NbN SC thin films, is reported in Fig.3.1. The disorder in[91] is tuned by controlling the level of Nb vacancies in the lattice and it is characterised by $k_F l$, where l is the electronic mean free path and k_F the Fermi wave vector.
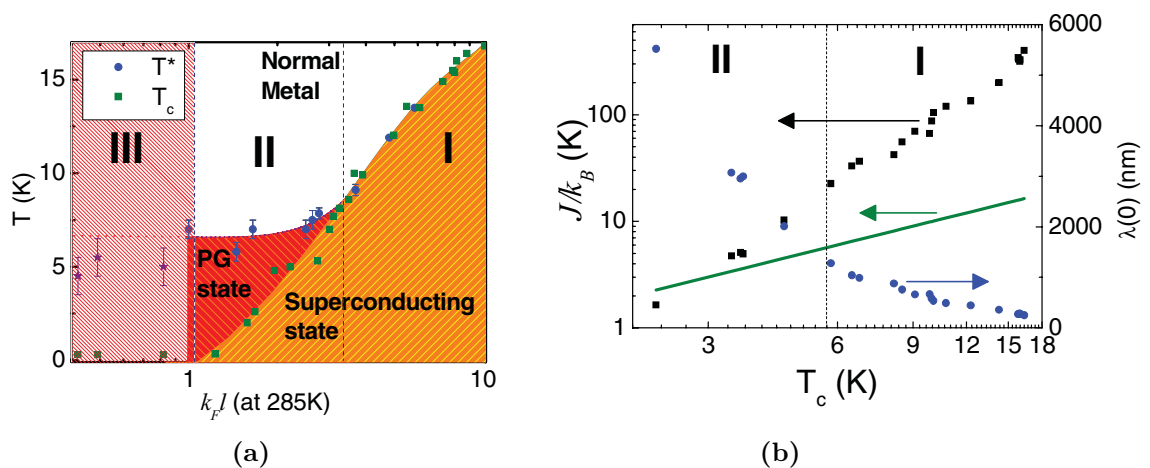
Figure 3.1. [91](a) Phase diagram of strongly disorder NbN, showing T_c and T^* as function of the disorder expressed in terms of $k_F l$. (b) Superfluid stiffness (J/k_B) and penetration depth $\lambda(T \to 0)$ for NbN films with different T_c. The solid line corresponds to $J/k_B = Tc$. Regimes I and II corresponding to the phase diagram are delineated by the dashed vertical line.

The first regime follows a conventional BCS behavior and it is characterised by a monotonically decrease of T_c due mostly to the increase of the repulsive e-e Coulomb interactions, which partially cancels the phonon-mediated attractive pairing inter-action. The disorder regime **II** , is instead characterised by two temperatures: T_c, above which the resistance appears, and T^*, above which the superconducting energy gap disappears. In this region the effects of the disorder on the superfluid stiffness J_s become visible: increasing the electronic scattering the disorder reduces J_s rendering the superconducting film susceptible to phase fluctuations. Thus when the disorder is strong enough, as in this region, the superconducting transition becomes driven

by phase fluctuations of pre-formed Cooper pairs. The relative insensitivity of T^* to the disorder level, suggests that also the gradual decreases of T_c is indeed driven by the increases of phase fluctuations, while the pairing amplitude remains almost constant. Finally, in the regime **III** the sample stays non-superconducting down to $300 \, mK$.
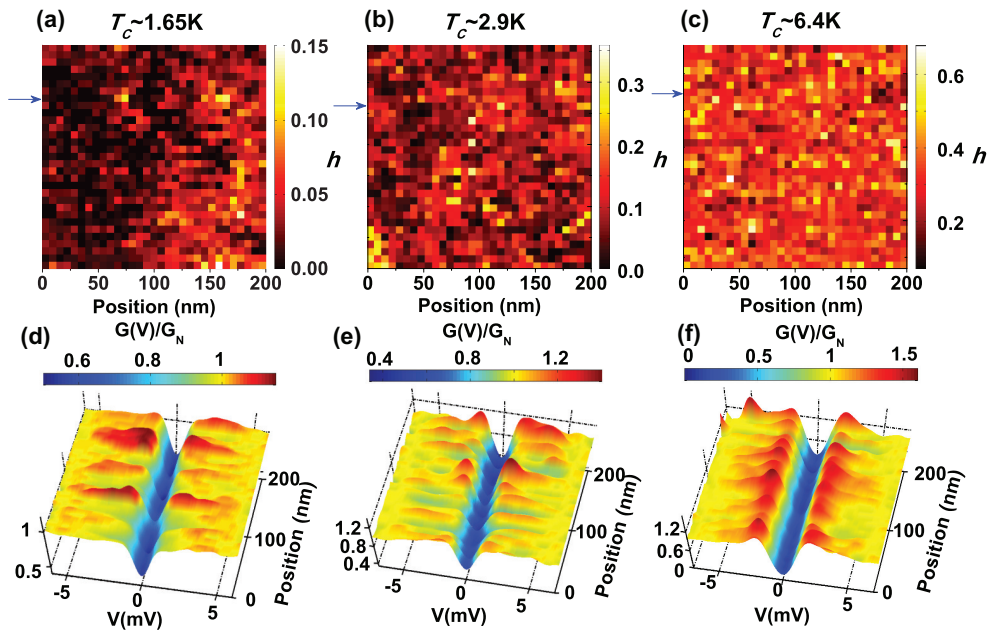
Figure 3.2. [35] (a)-(c) Spatial variation of the average order parameter h, measured at $500 \, mK$ for three NbN films with different T_c. (d)-(f) Normalised tunnelling spectra for the same samples along the line marked by arrows in panels (a)-(c).

In[35] the pseudogap region (**II** regime) has been further investigated via STS measurements, focusing the attention on the spatial variation of the SC order parameter in space. The samples investigated, whose measurements are reported in Fig.3.2, have $T_c \sim 1.65$, 2.9 and $6.4K$, corresponding to an estimated $k_F l \sim 1.5$, 1.8 and 2.7 respectively. For each film, tunnelling conductance (dI/dV vs V) has been measured over an area of $200 \times 200 \, nm$ at the temperature of $500 \, mK$. The normalised spectra obtained do not show any significant variation in the magnitude of the superconducting energy gap, as shown in Fig.3.2(d-f) while they show a large variance in the height of the coherence peaks h_i.

Hence, the scenario of a vanishing order parameter: $\langle \Delta \rangle \to 0$, with finite and uniform energy gap, suggests $\Delta_i \sim h_i$, as confirmed in [86].

Notably, as the disorder increases the map of the SC order parameter become more and more inhomogeneous showing spatial structures of *good* and *bad* SC-state, corresponding to higher and lower local superfluid stiffness. Together with the increase of the spatial correlated inhomogeneity, by increasing the disorder strength the order parameter probability distribution (Fig.3.3) gets logarithmically large, developing a bigger asymmetric tail and moving its mean value to lower values. In[35] it is also shown a remarkable property of such order parameter distribution (OPD),

indeed the OPDs obtained for different disorder levels collapse on the same curve by introducing as a scaling variable the logarithm of the OP, normalised to its variance (R_S in Fig.3.3). This peculiarity, open the question wether the thermodynamics smearing of the BKT transition is due to some emergent spatially correlated disorder or to the particular OPD found in such disordered systems.

I will address this question in the chapter 5 of the PhD Thesis.
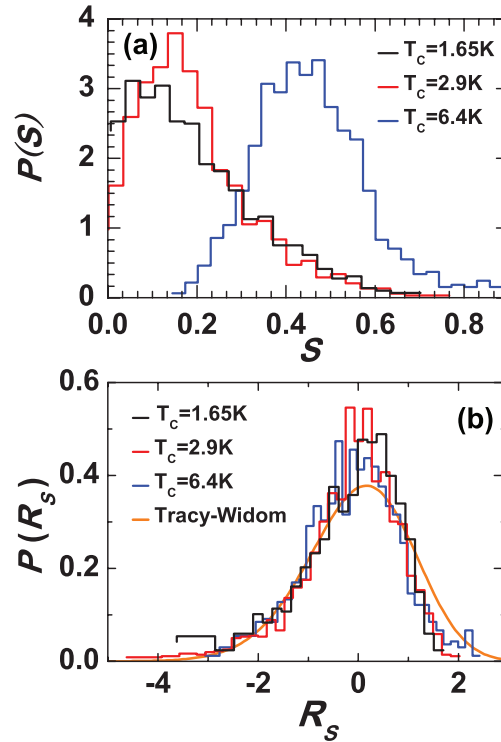
Figure 3.3. [35] (a) OPD of the three samples in linear scale. (b) The same data as in panel (a) plotted in terms of the rescaled variable R_S . The solid line corresponds to the Tracy-Widom distribution.

From the theoretical point of view, the study of disordered superconductors at the verge with the SIT, has been based both on a fermionic and a bosonic approach. The first prototype model can describe the SIT only with a big numerical effort that gives access only to small system sizes. Nevertheless it captures several features of strongly disordered superconductors, such as the survival of a large spectral gap due to the interplay between superconductivity and disorder and the emergence of spatial inhomogeneity of the pairing amplitude. On the other hand, the bosonic model simulating the competition between pair hopping and localisation represents the best theoretical approach to describe the SIT via the loss of the global phase coherence within the Cooper pairs, due firstly to the decrease and afterwards to the vanishing of the global SC superfluid stiffness.

3.2 Fermionic model

A microscopic description of the competition between disorder and superconductivity must necessarily start with the fermionic degrees of freedom. The model Hamiltonian usually considered for the investigation of disordered superconductors is the attractive Hubbard model in a random potential:

$$H = -t \sum_{\langle ij \rangle \sigma} (c_{i\sigma}^\dagger c_{j\sigma} + h.c.) - |U| \sum_i n_{i\uparrow} n_{i\downarrow} + \sum_{i\sigma} (V_i - \mu) n_{i\sigma} \tag{3.1}$$

where $c_{i\sigma}^\dagger$ and $c_{i\sigma}$ are the fermion creation and annihilation operators respectively, $n_{i\sigma} = c_{i\sigma}^\dagger c_{i\sigma}$ is the number operator, t is the hopping amplitude restricted to nearest neighbors sites, $|U|$ is the attractive on-site potential leading to s-wave SC and μ is the chemical potential. The disorder is embedded in the random potential V_i uniformly distributed within $[-V, V]$. Starting from the (3.1), one can proceed with the standard Bogolubov-de Gennes mean-field theory[92]. The decomposition of the interaction term gives the expectation values of the local pairing amplitude and the local density:

$$\Delta_i \equiv -|U| \langle c_{i\downarrow} c_{i\uparrow} \rangle, \quad \langle n_{i\sigma} \rangle = \langle c_{i\sigma}^\dagger c_{i\sigma} \rangle \tag{3.2}$$

yielding to an effective quadratic Hamiltonian:

$$H_{eff} = -t \sum_{\langle ij \rangle \sigma} (c_{i\sigma}^\dagger c_{j\sigma} + h.c.) + \sum_{i\sigma} (V_i - \tilde{\mu}_i) n_{i\sigma} + \sum_i [\Delta_i c_{i\uparrow}^\dagger c_{i\downarrow}^\dagger + \Delta_i^* c_{i\uparrow} c_{i\downarrow}] \tag{3.3}$$

where $\tilde{\mu}_i = \mu + |U| \sum_\sigma \langle n_{i\sigma} \rangle /2$ incorporates the site-dependent Hartree-shift. Introducing the quasiparticles operators γ_α and $\gamma_\alpha^\dagger$, one can diagonalise H_{eff} by means of the transformations:

$$c_{i\uparrow} = \sum_\alpha [\gamma_{\alpha\uparrow} u_{\alpha i} - \gamma_{\alpha\downarrow}^\dagger v_{\alpha i}^*] \tag{3.4}$$

$$c_{i\downarrow} = \sum_\alpha [\gamma_{\alpha\downarrow} u_{\alpha i} + \gamma_{\alpha\uparrow}^\dagger v_{\alpha i}^*] \tag{3.5}$$

with $u_{\alpha i}$ and $v_{\alpha i}$ satisfying $\sum_\alpha |u_{\alpha i}|^2 + |v_{\alpha i}|^2 \ \forall i$, finally obtaining:

$$\begin{pmatrix} \hat{K} & \hat{\Delta} \\ \hat{\Delta}^* & -\hat{K}^* \end{pmatrix} \begin{pmatrix} u_{\alpha i} \\ v_{\alpha i} \end{pmatrix} = E_\alpha \begin{pmatrix} u_{\alpha i} \\ v_{\alpha i} \end{pmatrix} \tag{3.6}$$

where $E_\alpha \geq 0$ are the excitation eigenvalues, while $\hat{\Delta} u_{\alpha i} = \Delta_i u_{\alpha i}$ and $\hat{K} u_{\alpha i} = -t \sum_{\hat{\delta} = \pm \hat{x}, \pm \hat{y}} u_{\alpha i + \hat{\delta}} + (V_i - \tilde{\mu}_i) u_{\alpha i}$ (similarly for $v_{\alpha i}$). Following the procedure of[86][25], from an initial guess for Δ_i's and $\tilde{\mu}_i$'s they first solve numerically the Eq.(3.6) on a finite lattice of N sites with periodic boundary conditions, obtaining the BdG eigenvalues $E_{\alpha i}$ and eigenvectors $[u_{\alpha i}, v_{\alpha i}]$. Afterwards, they compute the local pair amplitudes and the number density:

$$\Delta_i = |U| \sum_\alpha u_{\alpha i} v_{\alpha i}^*, \quad n_i = \sum_\alpha |v_{\alpha i}|^2 \tag{3.7}$$

and finally, they iterate the process until self-consistency is achieved bot for Δ_i and n_i at each site. From this calculations one can have access both to the probability distributions of the local SC order parameter and to its spatial variation within the system, for a given disorder realisation.
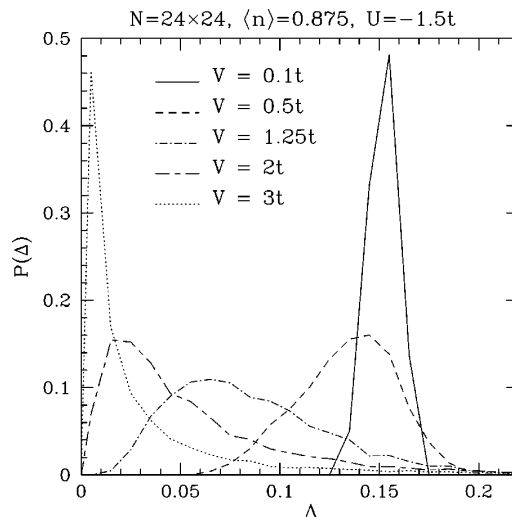
Figure 3.4. [86]Distribution of the local pairing amplitude for various disorder strengths. At low disorder the distribution $P(\Delta)$ is sharply peaked around $\Delta_0 \simeq 0.15$, the pure BCS value for $|U| = 1.5t$. $P(\Delta)$ becomes broad with increasing V and finally at a very large disorder gains significant weight near $\Delta = 0$.
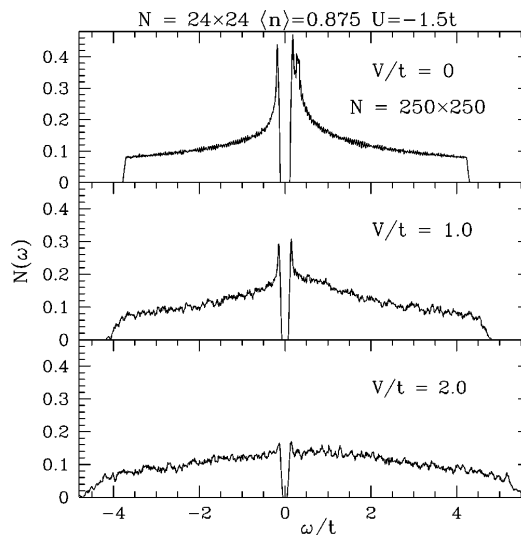

Figure 3.5. [86]Density of states $N(\omega)$ for three disorder strengths V. With increasing disorder the singular pile-up at the gap edge smears out pushing states towards higher energies. Surprisingly, the spectral gap remains finite even at large V.

From Fig.3.4 of[86], one can observe that with the increase of the disorder strength,

the probability distribution of Δ_i becomes broad and the BCS assumption of an uniform Δ, valid in the weak disorder limit, breaks down. Furthermore, together with this broadening as the disorder level increases, the distribution weight moves to lower value becoming significant close to $\Delta \simeq 0$ at very strong disorder.

However, despite in the strong disorder limit a large fraction of sites have near vanishing pairing amplitude, a finite spectral gap, obtained from the disordered averaged one-particle density of states $N(\omega) = \frac{1}{N}\sum_\alpha \delta(\omega - E_\alpha)$, still remains remarkably finite as shown in Fig.3.5.
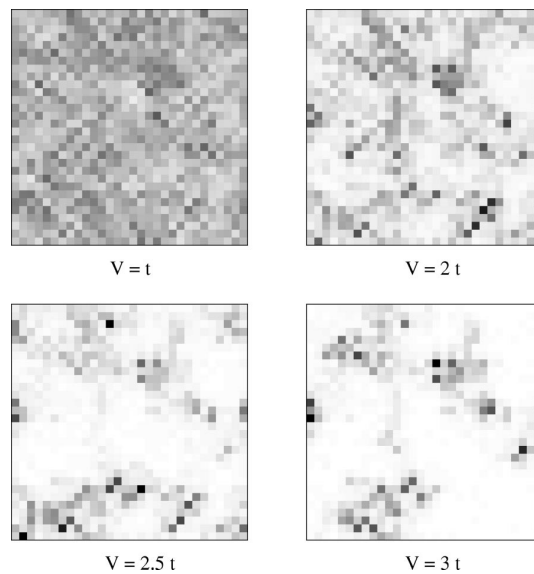
Figure 3.6. [86]Gray-scale plot for the spatial variation of the local pairing amplitude Δ_i for a particular realisation of the random potential, with increasing disorder strength. Note that at large V the system generates "SC islands" (dark regions) with large pairing amplitude separated by an insulating "sea" (white regions) with negligible pairing amplitude.
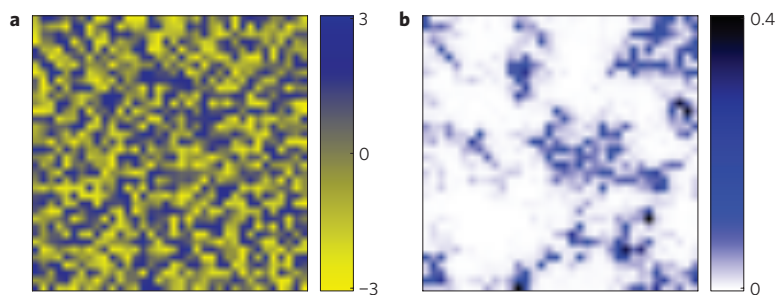
Figure 3.7. [25](a) Disorder realisation V_i on a 36×36 lattice at $V = 3t$. (b)Local pairing amplitude Δ_i from a BdG calculation at $|U| = 1.5t$, $T = 0$ and $n = 0.875$. Note the emergent granular structure where the pairing amplitude self-organizes into superconducting islands on the scale of the coherence length, even though the homogeneous disorder potential in (a) varies on the scale of a lattice spacing.

In order to deeper understand this pseudogap state, in[86][25] the spatial distribution of the Δ_i's for individual realisations of the disorder potential has been further investigated. As shown in Fig.3.6, at high disorder spatially correlated clusters of large Δ_i build up leaving aside large regions where $\Delta_i \simeq 0$. In[86] Ghosal et al. show that this emergent granularity is indeed responsible for the persistence of the energy gap above the superconducting critical temperature, since the eigenfunctions corresponding to low-lying excitations live entirely on such "SC islands", while the surrounding "insulating sea" only supports higher energy excitations. It is worth to highlight more that such granularity of the SC-state emerges from a disorder potential V_i completely uncorrelated site to site, as shown in Fig.3.7.

A further prediction that can be derived from this model, is the gradual reduction of the phase rigidity with the increase of disorder[86]. However, despite a dramatic suppression of the superfluid stiffness is derived in the strong disorder regime, J_s continues to remain nonzero within the BdG approximation. Hence, although so far we have captured several features of the SIT, such as the survival across the transition of the energy gap in the density of states, the emergence of a spatial inhomogeneity of the SC order parameter and the J_s reduction, the phase fluctuations ultimately responsible for the superconducting transition are beyond the BdG approximation. Nevertheless, there are many ways to include again the phase degrees of freedom, ignored in the mean-field approximation used so far. For instance by the use of a 2D quantum XY action solved numerically by Quantum Monte Carlo simulations[86], or by allowing the local phase θ_i in the BdG solutions to relax by the applied transverse fieldl[93].

3.3 Bosonic model

Following the original idea of Anderson[90], Ma and Lee in their seminal paper[94] proposed a theoretical model for the description of disordered superconductors based on the observation that even if single-particle states get localised by disorder, superconductivity can survive if there are enough states localised in a range of energy Δ. In this situation one can show[94] that the fermionic problem can be mapped into an effective bosonic model, more specifically in the XY pseudo-spin 1/2 Hamiltonian for hard bosons in the presence of a random transverse field:

$$\mathcal{H}_{PS} \equiv -2\sum_i \xi_i S_i^z - 2J \sum_{\langle i,j \rangle} \left(S_i^+ S_j^- + h.c. \right). \tag{3.8}$$

where the S_i's are spin-1/2 operators related to the fermionic creation and annihilation operators by:

$$S_i^z = \frac{1}{2}(\sum_{i,\sigma} c_{i\sigma}^\dagger c_{i\sigma} - 1) \tag{3.9}$$

$$S_i^- = (S_i^+)^\dagger = c_{i\downarrow} c_{i\uparrow} \tag{3.10}$$

Such spin-like picture of superconductivity is equivalent to describe a system where each site can be empty (corresponding to the eigenvalue $-1/2$ of S_i^z) or occupied

by a Cooper pair (eigenvalue $+1/2$). The disorder, embedded in the ξ_i's random quenched variables uniformly distributed in the box interval $[-W, W]$, competes with the hopping term $(S_i^+ S_j^- + h.c.)$, of amplitude $J > 0$, trying to localise the Cooper pairs. Thus the superconductor-insulator transition (SIT) can be tuned by the ratio W/J, controlling the competition between hopping and localisation. The model can be also interpreted in terms of a three-dimensional Heisenberg ferromagnet in the presence of a random transverse field of local intensity ξ_i. In this picture, the local SC order parameter is proportional to the expectation value of the spin in the $xy-$plane: $\Delta_i \propto \langle S_i^x + iS_i^y \rangle$ and hence the global SC order appears as the spontaneous magnetization within the xy plane. The random transverse magnetic field, increasing the spin projection on the Z axis, reduces the SC amplitude Δ_i. Following[36], we first solve the model (3.8) at mean-field level, breaking the $U(1)$ symmetry along i.e. x and remaining with a system living on the XZ plane whose ground state is:

$$|\Psi_{MF}\rangle = \prod_i \left[\cos(\phi_i/2) |\uparrow\rangle_i + \sin(\phi_i/2) |\downarrow\rangle_i \right] \tag{3.11}$$

being $\cos(\phi_i) = 2\langle S_i^z \rangle$ and $\sin(\phi_i) = 2\langle S_i^x \rangle$. The corresponding mean field energy reads:

$$E_{MF}[\phi_i] = -\sum_i \xi_i \cos(\phi_i) - J \sum_{\langle i,j \rangle} \sin(\phi_i)\sin(\phi_j) \tag{3.12}$$

whose minimisation with respect to ϕ_i gives us the self-consistent equations:

$$\xi_i \tan(\phi_i) = J \sum_{j(i)} \sin(\phi_j) \tag{3.13}$$

where the sum on the right hand side is extended to all the nearest neighbors of the site i.

Thus the ϕ_i's identify the new axis of quantisation of the system: $|\Psi_{MF}\rangle$ is an eigenstate of each operator $S_i^\parallel \equiv S_i^z \cos(\phi_i) + S_i^x \sin(\phi_i)$ with eigenvalue $+1/2$. The spin-wave excitations, i.e. the smallest energy excitations, around this mean field solution can be derived by means of the Holstein-Primakov approximation, consisting in the introduction of bosons annihilation and creation operators a_i and $a_i^\dagger$, related to the new-basis spins as:

$$S_i^\parallel = \frac{1}{2} - a_i^\dagger a_i \tag{3.14}$$

$$S_i^+ = S_i^\perp + iS_i^y = (1 - a_i^\dagger a_i)^{1/2} a_i \simeq a_i \tag{3.15}$$

$$S_i^- = S_i^\perp - iS_i^y = a_i^\dagger (1 - a_i^\dagger a_i)^{1/2} \simeq a_i^\dagger \tag{3.16}$$

with $S_i^\perp = -S_i^z \sin(\phi_i) + S_i^x \cos(\phi_i)$. Substituting Eq.(3.15)- (3.16) in Eq.(3.8) up to the Gaussian level, we get the Hamiltonian:

$$H_{PS} \simeq E_{MF} \sum_{ij} \left[A_{ij}(a_i^\dagger a_j + h.c.) + \frac{1}{2}B_{ij}(a_i a_j + h.c.) \right] \tag{3.17}$$

where

$$A_{ij} = 2\delta_{ij}\frac{\xi_i}{\cos(\phi_i)} - J(1 + \cos(\phi_i)\cos(\phi_j))(1 - \delta_{ij}) \quad (3.18)$$

$$B_{ij} = J(1 - \cos(\phi_i)\cos(\phi_j))(1 - \delta_{ij}) \quad (3.19)$$

Finally, we can diagonalised (3.17) via a standard Bogolubov transformation for bosons $a_i = \sum_\alpha (u_{\alpha i}\gamma_\alpha + v_{\alpha i}\gamma_\alpha^\dagger)$, so that:

$$H_{PS} = \sum_\alpha E_\alpha \gamma_\alpha^\dagger \gamma_\alpha + \ const \quad (3.20)$$

To describe the bosons excitations in terms of collective modes and in particular of phase fluctuations, we need to make one step further by defining the phase operators Θ_i and their conjugated momenta L_i, satisfying $[\Theta_i, L_j] \equiv i\delta_{ij}$:

$$\Theta_i \equiv -2\frac{S_i^y}{\sin(\phi_i)} = \sum_\alpha \frac{\phi_{\alpha i}}{\sqrt{2}i}(\gamma_\alpha^\dagger - \gamma_\alpha) \quad (3.21)$$

$$L_i \equiv S_i^\perp \sin(\phi_i) = \sum_\alpha \frac{l_{\alpha i}}{\sqrt{2}}(\gamma_\alpha^\dagger + \gamma_\alpha) \quad (3.22)$$

with $\phi_{\alpha i} \equiv \sqrt{2}(u_{\alpha i} - v_{\alpha i})/\sin(\phi_i)$ and $l_{\alpha i} \equiv \sqrt{2}(u_{\alpha i} + v_{\alpha i})\sin(\phi_i)/\sqrt{2}$. The fact that the Θ_i's are the quantum operators associated to the phase fluctuations of the SC order parameter can be understood from a semi-classical argument by writing the operator associated to the local order parameter as $S_i^- \simeq |\Delta_i|(1 + i\Theta_i)$ that implies (3.22), since $|\Delta_i| = \langle S_i^x \rangle$. H_{PS} in Eq. (3.20) can then be rewritten as a quantum phase-only model, whose classical part corresponds to the gaussian approximation of the classical XY model:

$$H'_{PS} \simeq \frac{1}{2}\sum_{i,\mu=\hat{x},\hat{y}} J_i^\mu(\Delta_\mu\Theta_i)^2 + \frac{1}{2}\sum_{i,j} L_i\chi_{ij}^{-1}L_j \quad (3.23)$$

where $\chi_{ij}^{-1} \equiv 2\frac{(A_{ij}+B_{ij})}{\sin(\phi_i)\sin(\phi_j)}$ plays the role of an inverse compressibility, Δ_μ is the discrete derivative in the μ direction and J_i^μ represents the local stiffness of the link $(i, i+\mu)$, which now embeds the disorder. Quite interesting, even though the initial disorder was uniformly distributed, the maps in real space of the local stiffness:

$$J_i^\mu \equiv J\sin(\phi_i)\sin(\phi_{i+\mu}) \quad (3.24)$$

develop structures in real space as shown in Fig.3.8.This emergent inhomogeneity of the SC order parameter captures very well what experimentally observed via STS measurements (Fig.3.2) in real space. The inhomogeneity, moreover, increase with the disorder strength, forming in the strong disorder regime (i.e. $W/J = 10$) percolative paths for the superfluid currents and, at the same time, isolated *good* SC islands, responsible for the finite-frequency optical absorption as shown in[36]. Finally, it is worth noticing that even the probability distributions of the couplings obtained from (3.8), have the same qualitative trend of the order parameter distributions obtained in[35].
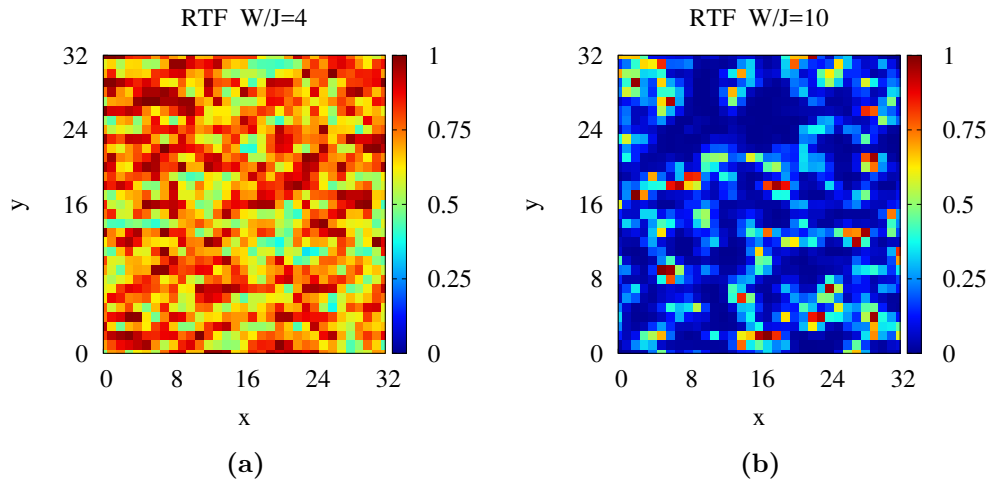
Figure 3.8. Maps in real space of the local stiffness $J_i^x = J \langle \sigma_i^x \rangle \langle \sigma_{i+x}^x \rangle$ (being $\sigma_i^x = 2S_i^x$), obtained self-consistently by means of Eq.(3.13). The two maps correspond to two different level of disorder: (a) $W/J = 4$, (b) $W/J = 10$.
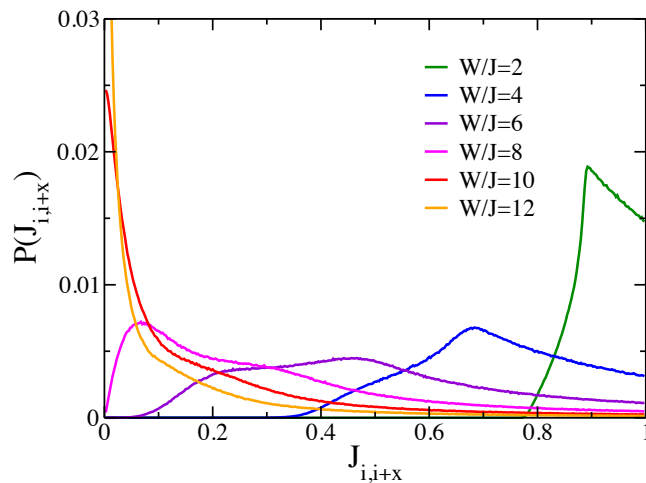
Figure 3.9. Coupling distributions for different values of the disorder strength W/J.

So far we have seen that in the case of SC thin films, the BKT transition is found in the presence of strong disorder. Moreover, as observed experimentally both in thin films[84, 75, 95, 96, 85, 87, 97] and SC heterostructures[98, 13, 88], such disorder can induce a "granular" inhomogeneous SC state, well understood theoretically[86, 23, 34, 25, 93, 35] as the way out of superconductivity, which requires phase coherence, to survive in the presence of disorder-induced charge localisation. Understanding the role of the microscopic electronic disorder on the BKT transition within SC fermionic models is an incredible task[23, 24, 25, 26], due mainly to the small size of systems accessible numerically. Alternatively, one can address the question directly within a proper phase-only model.

A natural option is the two-dimensional XY model with random J_{ij} couplings[27, 28, 29, 30], which mimics the random Josephson-like coupling between coarse-grained neighboring SC islands:

$$H_{XY} = -\sum_{\langle ij \rangle} J_{ij} \cos(\theta_i - \theta_j) \qquad (3.25)$$

It is indeed, nothing but the classical limit of the quantum phase-only Hamiltonian of Eq. (3.23).

The main question I have addressed in the Thesis is how the nature of the disorder in the couplings J_{ij} affects the BKT physics, not only in terms of the smearing of the superfluid-stiffness jump, but also in the temperature dependence of the response functions. I will thus consider the classical XY model in two cases: with spatially uncorrelated and with spatially correlated disordered couplings.

Chapter 4

2D XY model: uncorrelated disorder

In this chapter, two paradigmatic kinds of spatially uncorrelated disorder are considered: random couplings with Gaussian distribution and random diluted couplings. As we will see, the BKT transition is very robust against such uncorrelated disorder, which leaves unaffected the critical jump of the superfluid stiffness perfectly in agreement with the Harris criterion[31]. Furthermore, by means of the mapping into a random resistor network[33], we provide a systematic way to study the effect of such spatially uncorrelated disorder both on the superfluid stiffness and on the paramagnetic and diamagnetic response functions.

The chapter is organised as follow: in the first section I will briefly review the numerical methods used in this study; I will further present, in section (4.2), the Monte Carlo numerical results obtained for the clean case introducing the main observables needed for the BKT characterisation. In section (4.3), I will shortly discuss the Harris Criterion and its implication, while in section (4.4) and (4.5) the numerical results obtained for the disordered XY model in the presence of random couplings Gaussian distributed and random diluted couplings respectively will be presented. Finally in the last section of the chapter, I will derive an effective medium theory for the 2D XY model in the presence of spatially uncorrelated disorder.

4.1 Monte Carlo simulations method

The 2D XY model has been studied by means of Monte Carlo (MC) simulations, a well known, very versatile and powerful numerical method largely used in statistical mechanics to access thermodynamical quantities without the need to solve the system analytically or to perform an exact enumeration of all the possible configurations. Given the two basic principles of ergodicity and detailed balance[1], there is no unique choice of sampling algorithm: it strongly depends on the system studied and it is

---

[1]The ergodicity requires the accessibility, starting from any configuration C_0 with nonzero Boltzmann weight, through a finite number of MC moves to any other configuration with nonzero Boltzmann weight of the phase space. While the detailed balance prevent the Markov chain to be trapped in cycle limit, imposing the equilibration between each elementary process and its reverse process once the equilibrium state has been reached.

chosen in such a way to ensure the system thermalisation (i.e. the achievement of the equilibrium values of the observables we are looking at) in the smallest possible number of iterations. In our simulations, we have used a local Metropolis algorithm, needed to probe the correct canonical distribution of the system, combined with a micro-canonical Over-relaxation algorithm[99], particularly useful for the thermalisation of continuous models which suffer more for the critical slowing down at the critical point. Hence, each Monte Carlo step consists of 5 Metropolis spin flips of the whole lattice, followed by 10 Over-relaxation sweeps of all the spins.

For each temperature we perform 25000 MC steps, we discard the firsts 10000 needed for the system thermalisation, and over the remaining 15000 ones, we measure the thermodynamical observables every 5 MC steps in such a way to compute their time-averages over MC uncorrelated steps[2]. The statistical errors of such measurements, in many cases cannot be computed directly from the MC time evolution of the system. This is the case for instance of the superfluid stiffness. The usual way to overcome this issue is by means of resampling methods, specifically in this work we have used the Jackknife resampling one[99].

In the presence of quenched disorder, on the other hand, the dominant statistical errors come directly from the average values obtained from different disorder realisations. Thus, for the case of disordered system, the average and the correspondent statistical errors have been computed over 15 independent configurations of quenched disorder up to 30 in the strong-disorder limit.

Finally, we have used the Simulated Annealing algorithm to help the correct thermalisation of the system during its temperature evolution. Indeed, lowering the temperature, the free energy landscape (especially in the presence of disorder) can develop several local minima corresponding to different metastable states. The Simulated Annealing procedure is, together with the Parallel Tempering[100], the most used algorithm to prevent the trapping of the system in one of these local metastable minima. Starting from the highest temperature considered, the system is let evolve from an initial configuration of random spins, once reached its equilibrium state (global minimum of the free energy) the temperature is slightly decreased and a new thermalisation starts. This process, consisting in giving as initial state to the lower temperature, the final state of the higher one, is iterated until the lowest temperature of interest has been achieved.

4.2   Clean Case

Let us start considering the classical XY model with constant and uniform couplings:

$$H_{XY} = -J \sum_{\langle ij \rangle} \cos(\theta_i - \theta_j); \quad \text{where} \quad J = 1 \tag{4.1}$$

The superfluid stiffness J_s, also referred as helicity modulus Υ in the context of statistical mechanics, gives the response of the system under a torsion of the phase. It is defined by the second derivative of the free energy with respect to a phase twist α on a given direction, let us say x, at $\alpha = 0$:

---

[2]In order to compute correctly the averages is important to give an estimate of the autocorrelation time τ_a, the number of MC steps needed to produce two independent system configurations. In our simulation $\tau_a = 5$ MC steps.

$$J_s \equiv = -\frac{1}{\beta} \frac{\partial^2 \ln Z_{XY}(\alpha)}{\partial \alpha^2} \big|_{\alpha=0} \tag{4.2}$$

where $Z_{XY}(A) \equiv \int \prod_i d\theta_i \exp[-\beta H_{XY}(A)]$ and $H_{XY}(\alpha) = -J \sum_{\langle ij \rangle} \cos(\theta_i - \theta_j + \alpha_{ij})$ with $\alpha_{ij} = \alpha$ in the direction of the torsion, thus for $j = i \pm x$, and $\alpha_{ij} = 0$ for $j = i \pm y$. From the second derivative in (4.2) one obtains two terms: the diamagnetic term, which coincides except for the sign with the average energy per unit volume of the system, and the paramagnetic J_p one, i.e. the current-current correlation function for the paramagnetic current $I_{ij}^p = J_{ij} \sin(\theta_i - \theta_j)$ of the model. Thus:

$$J_s = J_d - J_p \tag{4.3}$$

$$J_d = \frac{J}{L^2} \langle \sum_i \cos(\theta_i - \theta_{i+x}) \rangle \tag{4.4}$$

$$J_p = \frac{J^2}{TL^2} \langle (\sum_i \sin(\theta_i - \theta_{i+x}))^2 \rangle \tag{4.5}$$

where $\langle \ldots \rangle$ indicates the thermal average. The typical temperature dependence of $J_s(T)$ is shown in Fig.4.1.
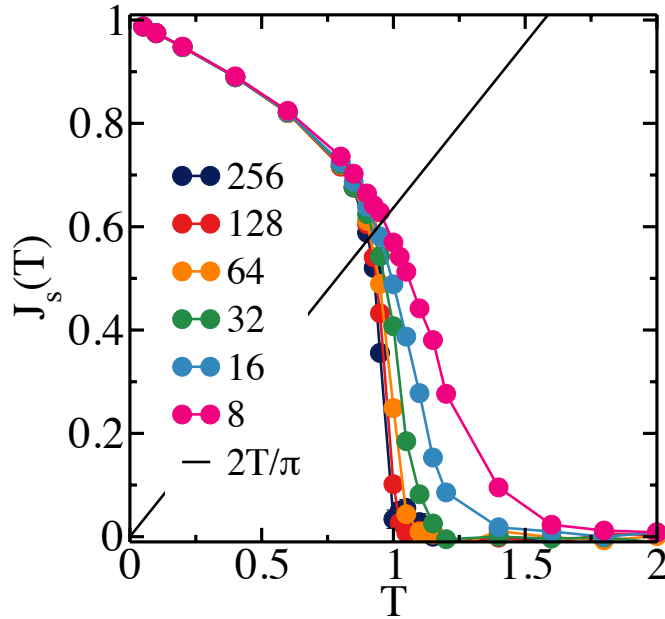
**Figure 4.1.** Superfluid stiffness as function of the temperature for different linear sizes L. The solid black line is the critical line whose intersection with J_s defines the critical temperature T_{BKT}.

In the limit of zero temperature, as we can see from Fig.4.1, the superfluid stiffness coincides with the value of the coupling constant $J_s(T = 0) = J = 1$. In the low-temperature regime, even if the topological vortex-antivortex excitations are absent, the *smooth* spin-waves excitations contribute in depleting the diamagnetic contribution (4.4) of the superfluid stiffness linearly in temperature (see Fig.4.2a).

In particular, as we have derived in the first chapter (see Eq.(1.65)), expanding the cosine up to the fourth other term, one finds that:

$$J_s(T) \simeq J_s(0) - \frac{T}{4}, \quad \text{for} \quad \frac{T}{T_{BKT}} \ll 1 \tag{4.6}$$

On the other hand, at low temperature, the paramagnetic term J_p does not contribute to the superfluid stiffness staying constant and equal to zero (see Fig.4.2b) . Approaching the critical temperature it starts to become finite, until at $T = T_{BKT}$ it sharply increases canceling the diamagnetic term contribution in (4.3) and causing the jump of the superfluid stiffness. For infinite system, as we have already discussed, the transition is expected to occur as a sharp jump of $J_s(T)$ at the temperature where $J_s(T_c) = 2T_c/\pi$, thus at the intersection between $J_s(T)$ and the solid black line $2T/\pi$ in Fig.4.1 . When L is finite, the finite size effects let $J_s(T)$ to remain
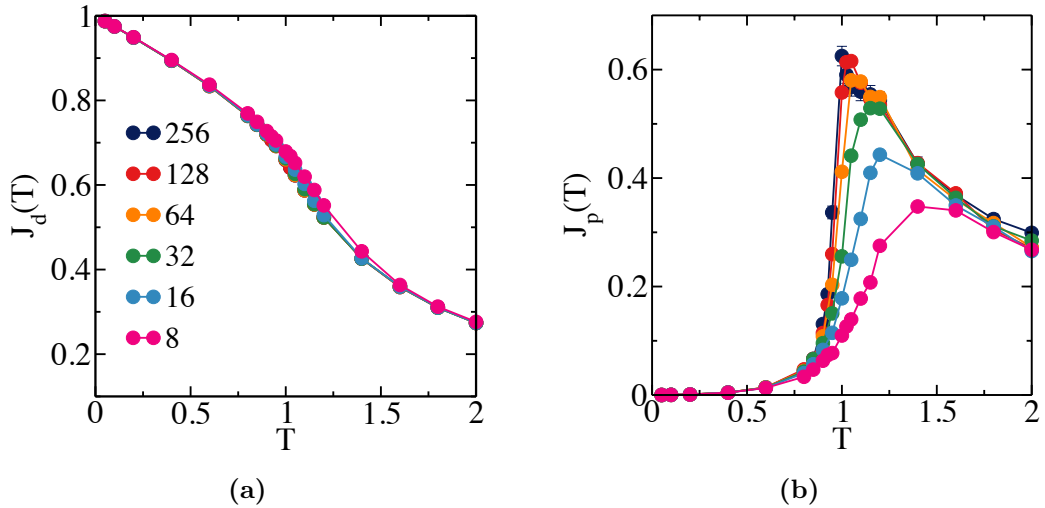
Figure 4.2. (a) Diamagnetic J_d and (b) paramagnetic J_p response function as function of the temperature for different lattice sizes. As discussed in the main text, the finite size effects interest mostly the paramagnetic term, leaving almost unchanged the diamagnetic one.

finite even at $T > T_c$, the effect being larger at smaller lattice sizes. On the other hand, in the region below the critical temperature $T < T_c$ the superfluid density is not affected by the reduction of the lattice size. Such asymmetry means that finite size effects by themselves cannot explain the broadening of the superfluid-stiffness jump observed in real systems (see for instance Fig.2.8), being it symmetric around the critical temperature T_{BKT}.
Looking at the Fig.4.2a and 4.2b, we can also notice that while the diamagnetic term is almost insensitive to the finite size of the system, the paramagnetic term is the one responsible for the high-temperature tail developing at finite L: its peak in temperature becomes smaller and smaller as the lattice size decrease. Indeed, the paramagnetic term J_p is the one depending on the vortices interaction, which logarithmically depends on their mutual distance.
Finally, from the analysis of Fig. 4.1 we can see that in the clean case we do not find appreciable differences between the cases $L = 256$ and $L = 128$. We will then

fix the lattice size for the following numerical simulations at $L = 128$, even though for selected disorder level we will show also simulations at $L = 256$.

Once defined the observables object of this study and having characterised their trends in temperature in the absence of disorder, we can now address the issue of the effect of the disorder on the temperature dependence of these three response functions: J_s, J_d and J_p.

4.3 Uncorrelated disorder: Harris Criterion

How quenched disorder modifies phase transitions and critical points is an issue that have fascinated physicist from decades. An important turning point in this study is due to Harris[31], who formulates a criterion controlling wether a particular clean critical point is modified by the presence of impurities within the system. In his first formulation, to account for the effects of quenched disorder, Harris considered a system with random critical temperatures, i.e. effective local critical temperatures $T_c(\mathbf{r})$, with short-range spatial correlations. Thereafter, Weinrib and Halperin[101] extended the Harris criterion considering local transition temperatures with a correlation function following, for large separation $\mathbf{r}$, a power law decay:

$$g(\mathbf{r}) = \langle T_c(\mathbf{r})T_c(0)\rangle - \langle T_c(\mathbf{r})\rangle^2 \sim \mathbf{r}^{-a} \qquad (4.7)$$

being $\langle \ldots \rangle$ the average over the disorder distribution. The idea behind the derivation, is to consider the system as formed by regions of size ξ, the pure correlation length, and to look if the variation in their critical temperatures become negligible as $T \to T_c$. Being $t(\mathbf{r}) \equiv (T - T_c(\mathbf{r}))/T_c$ the local reduced critical temperature, the effective reduced critical temperature of a region is defined as:

$$t_v = \frac{1}{V} \int d\mathbf{r}\ t(\mathbf{r}) \qquad (4.8)$$

where $V = \xi^d$ is the volume of the d-dimensional region. In the limit of $T \to T_c$ (i.e. ξ large), the variance of the t_V is:

$$\Delta_{t_v}^2 = \langle t_v(\mathbf{r}_1)t_v(\mathbf{r}_2)\rangle - \langle t_v(\mathbf{r}_1)^2\rangle =$$
$$= \xi^{-2d} \int_V d\mathbf{r}_1 \int_V d\mathbf{r}_2\ g(\mathbf{r}_1 - \mathbf{r}_2) \sim \xi^{-d} \int_0^\xi dr\ r^{d-1}g(r) \qquad (4.9)$$

Hence, by means of Eq.(4.7) we can write:

$$\Delta_{t_v}^2 \sim \xi^{-d} \int_0^\xi dr\ r^{d-a-1} \qquad (4.10)$$

so that:

$$\frac{\Delta_{t_v}^2}{t^2} = \begin{cases} t^{d\nu-2}, & a > d \\ t^{d\nu-2} \ln t^{-\nu}, & a = d \\ t^{a\nu-2}, & a < d \end{cases} \qquad (4.11)$$

where we have substituted ξ with its dependece on t close to criticality: $\xi = t^{-\nu}$. The disorder does modify the critical behavior of the system if the ratio $\Delta_{t_v}^2/t^2$ does

not goes to zero as $t \to 0$, thus when:

$$\nu < 2/d, \quad a \geq d \tag{4.12}$$

$$\nu < 2/a, \quad a < d \tag{4.13}$$

where the case $a \geq d$ corresponds to the original short-range Harris criterion.
We can immediately recognise that for the case of the XY model, being ξ exponentially dependent on the reduced critical temperature (i.e. $\nu = \infty$), the conditions (4.12) and (4.13) are never satisfied. This is the reason why in general one would expect the disorder to be irrelevant on the BKT transition. It should be emphasised, however, that the Harris criterion does not provide a guaranteed criterion of *irrelavance* of disorder. Indeed, dealing with a specific mechanism of how disorder can become relevant, the argument provides only a *sufficient*, rather than *necessary*, condition for the relevance of disorder. Nevertheless, in the following sections we will see that spatial uncorrelated disorder is indeed irrelevant on the critical behavior of the XY model.

4.4   Disordered couplings: Gaussian distributed

The paradigmatic way to introduce disordered couplings within the XY model:

$$H_{XY} = -\sum_{\langle i,j \rangle} J_{i,j} \cos(\theta_i - \theta_j) \tag{4.14}$$

is to randomly extract their local values J_{ij} from a Gaussian distribution:

$$P_G(J_{ij}) = \frac{1}{\sqrt{2\pi\sigma^2}} \exp\left[-\frac{(J_{ij} - \bar{J})^2}{2\sigma^2} \right]$$

Keeping the mean value of the distribution fixed to $\bar{J} = 1$, we have considered different values of the standard deviation σ, obviously corresponding to different levels of disorder. Furthermore, in order to avoid unphysical negative local superfluid stiffness (i.e. antiferromagnetic couplings), we have truncated the gaussian distribution through the constraint $J_{ij} \geq 0$. The three response function J_s, J_d and J_p in the presence of the disorder modifies from (4.3),(4.4), (4.5) to:

$$J_s = J_d - J_p \tag{4.15}$$

$$J_d = \frac{1}{L^2} \overline{\langle \sum_i J_{i\,i+x} \cos(\theta_i - \theta_{i+x}) \rangle} \tag{4.16}$$

$$J_p = \frac{1}{TL^2} \overline{\langle (\sum_i J_{i\,i+x} \sin(\theta_i - \theta_{i+x}))^2 \rangle} \tag{4.17}$$

where $\overline{\cdots}$ indicates the average over different quenched disorder realisations.
From Fig.4.3, we can see as the superfluid stiffness conserves its trend in temperature for every strength of the disorder considered, showing in all the cases a sharp downturn at the intersection between $J_s(T)$ and the critical line $2T/\pi$, as expected for the clean case.
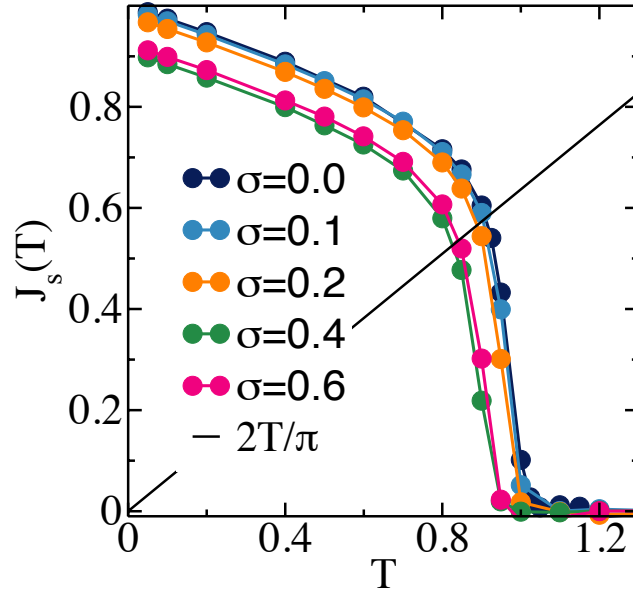
Figure 4.3. Superfluid stiffness as function of the temperature obtained for gaussian distributed disordered coupling J_{ij}. Different value of the standard deviation σ are shown. The solid black line is the critical line $2T/\pi$.

The only appreciable effect of the disorder on the transition is the zero temperature depletion of the superfluid stiffness and the correspondent reduction of the critical temperature T_c. Such depletion increases with the disorder strength, but for the case of $\sigma = 0.6$ (being $T_c(\sigma = 0.6) > T_c(\sigma = 0.4)$) in which the constraint $J_{ij} \geq 0$ by the truncation of the probability distribution $P_G(J_{ij})$, moves the effective mean value of the coupling above one.

At low temperature the primary excitations of the model are disordered longitudinal spin-waves, which can be well described by the quadratic approximation of the Hamiltonian (4.14), $H \approx \int d\mathbf{r} J(\mathbf{r})(\nabla\theta(\mathbf{r}))^2$. As we will see in details in the last section of this chapter, by making an expansion of the local stiffness $J(\mathbf{r}) = \bar{J} + \delta J(\mathbf{r})$ around its average value one can show that at low temperatures

$$J_d \simeq \bar{J} - T/4 \tag{4.18}$$

$$J_p = \bar{J}\left[\frac{\langle\delta J^2\rangle}{2\bar{J}^2} + c(T)^2\right] \tag{4.19}$$

where c is numerical constant. As confirmed by MC simulations (see Fig.4.4a and 4.4b), the diamagnetic term at $T = 0$ is equal to the mean value of the couplings $\bar{J}$ (note that, as we have already mentioned, for $\sigma = 0.6$ $\bar{J} > 1$) and it decreases linearly at low temperature as in the clean case.

Even the paramagnetic term has the same trend in temperature as the clean case, except for its zero-temperature value which increases with the strength of the disorder, being it proportional to the variance $\langle\delta J^2\rangle$ in (4.19).

(a)   (b)
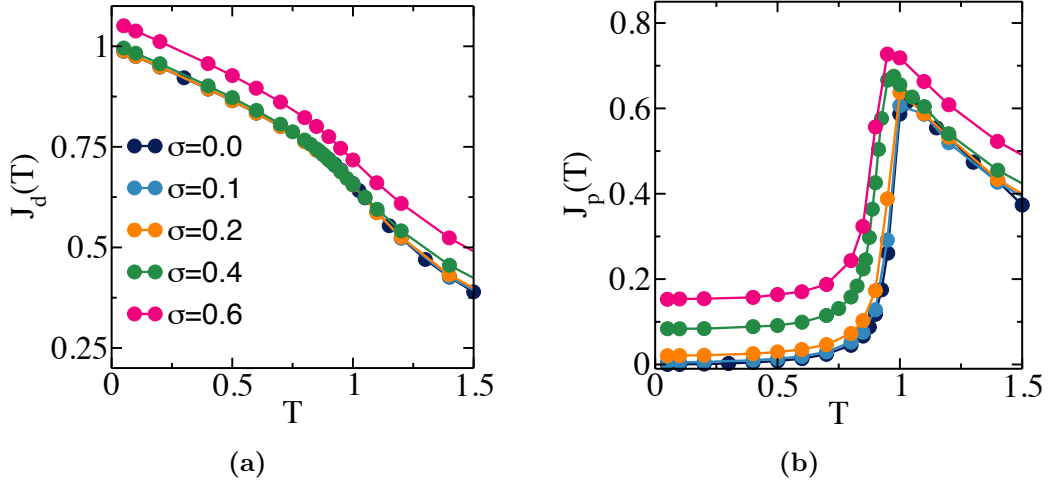
Figure 4.4. (a) Diamagnetic J_d and (b) paramagnetic J_p response function as function of
the temperature for different value of the Gaussian-distribution standard deviation σ.
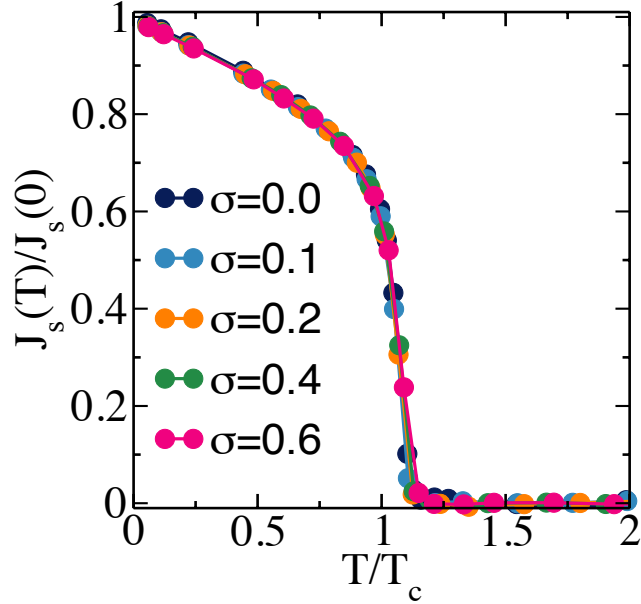
Figure 4.5. renormalized curves of the superfluid stiffness as function of the temperature:
$J_s(T)$ has been renormalized by its zero temperature value, while T by the critical
temperature T_c extrapolated by the intersection between $J_s(T)$ and $2T/\pi$. Every curve
corresponding to different values of the standard deviation σ collapse exactly on the
same curve.

As a consequence, at $T = 0$ disorder induces a paramagnetic suppression of the
stiffness:

$$J_s^{app}(T = 0) \simeq \bar{J} \left[1 - \langle \delta J^2 \rangle / 2\bar{J}^2 \right] \tag{4.20}$$

which can also be obtained[27] by using the mapping[33] into a random-resistor
network with conductance J_{ij} at each node, as we will see in the following.
The irrelevance of disorder for the transition is further emphasised when the $J_s(T)$

curves are rescaled by the $T = 0$ value of the stiffness and by T_c, see Fig.4.5. Here we finds a remarkable collapse of all the curves on each other, showing the complete irrelevance of disorder even away from criticality. According to the previous discussion, this follows from the fact that the leading temperature dependence below T_c, as we have seen in the first Chapter, is due to the universal spin-wave suppression of the diamagnetic term:

$$J_s(T) = J_s(0) - T/4 \tag{4.21}$$

Since the superfluid stiffness and the critical temperature are related via the Kosterlitz-Nelson[32] universal relation:

$$J_s(T_c) = \frac{2T_c}{\pi} \tag{4.22}$$

assuming that Eq.4.21 is approximately valid up to T_c, it follows that:

$$J_s(T_c) = J_s(0) - T_c/4 = \frac{2T_c}{\pi} \tag{4.23}$$

From (4.23) we can see that T_c itself scales with $J_s(T = 0)$ as:

$$T_c = \frac{4\pi J_s(0)}{\pi + 8} \tag{4.24}$$

Hence:

$$\frac{J_s\left(\frac{T \cdot T_c}{T_c}\right)}{J_s(0)} = 1 - \frac{T}{4T_c}\frac{T_c}{J_s(0)} = 1 - \alpha\frac{T}{T_c} \tag{4.25}$$

where α is a numerical constant independent on disorder.

4.5 Disordered couplings: link dilution

Another typical way to introduce disorder within an interacting spin system is to randomly remove links between nearest neighbors spins. Despite its simplicity, the link dilution is a particularly interesting kind of uncorrelated disorder for the percolating transition it induces within the system. Indeed, being p the dilution level[3], it is possible to define a critical value p_c at which the system does not show anymore a phase transition, being it the usual second order phase transition, for the case of the 3D Ising model, or the BKT one. The loss of the phase coherence within the system at $p = p_c$ is the result of the system fragmentation in disconnected islands of spins. Such phenomenology somehow recalls the fragmentation of the SC order parameter experimentally observed, raising the question whether the link dilution affects or not the superfluid-stiffness critical jump.
We have addressed this interesting issue by means of Monte Carlo simulations on the diluted XY model. Being r a random number uniformly distributed in $[0, 1]$, for

---

[3]Corresponding to the density of link removed within the system.

every disorder configuration, we randomly assign to each link J_{ij} the value 0 or 1 according to:

$$J_{ij} = \begin{cases} 0 & \text{if } r \leq p \\ 1 & \text{if } r > p \end{cases} \tag{4.26}$$

We have considered different values of p below the critical 2D percolation value $p_c = 0.5$, and for every value of p we have studied the temperature evolution of the superfluid stiffness, as reported in Fig.4.6 .
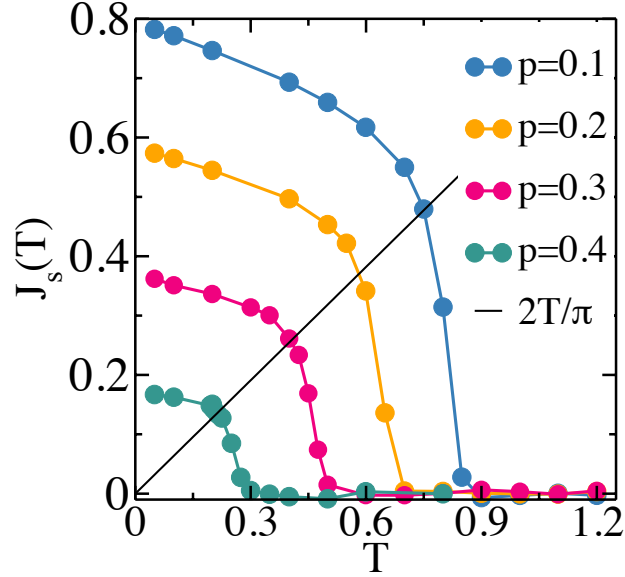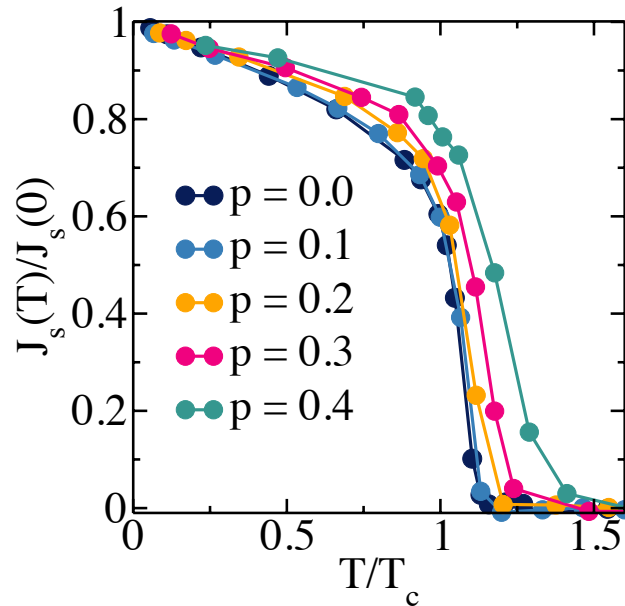

Figure 4.6. Superfluid stiffness as function of the temperature obtained for diluted disordered coupling J_{ij}. Different value of the dilution p are shown. The solid black line is the critical line $2T/\pi$
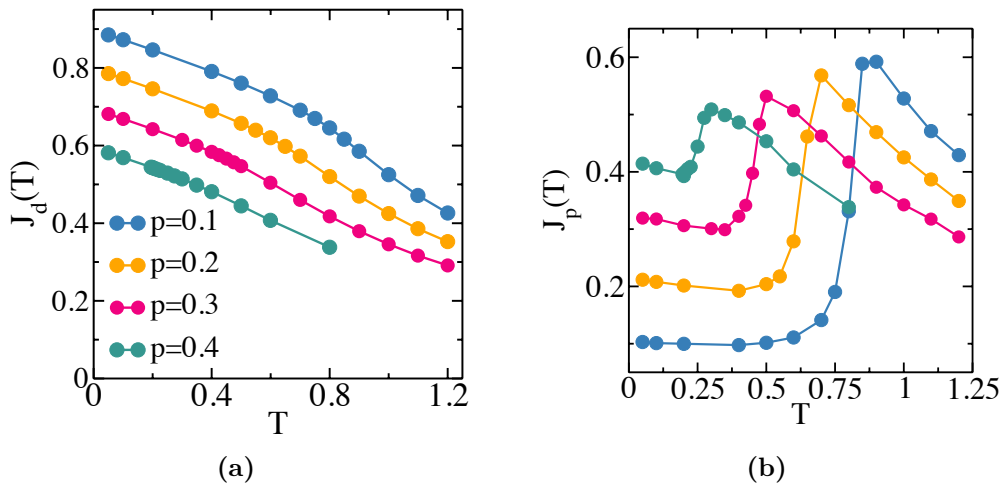
Figure 4.7. (a) Diamagnetic J_d and (b) paramagnetic J_p response function as function of the temperature for different value of the coupling dilution p.

With the increase of the link dilution, the zero temperature superfluid stiffness gets progressively suppressed, vanishing at $p = p_c$. Together with $J_s(T = 0)$, as expected from the universal relation (4.22) between J_s and T_{BKT}, also the critical temperature decreases as the disorder level increases. Nevertheless the jump at the critical point appears to be almost unchanged respect to the clean case, since even for very high dilution (look for instance $p = 0.4$) the downturn at the intersection between $J_s(T)$ and $2T/\pi$ stays sharp, showing no broadening.

Figure 4.8. renormalized curves of the superfluid stiffness as function of the temperature: $J_s(T)$ has been renormalized by its zero temperature value, while T by the critical temperature T_c extrapolated by the intersection between $J_s(T)$ and $2T/\pi$. Every curve corresponds to different values of the dilution p.

However, with respect to the previous case of Gaussian-distributed couplings, the irrelevance of the disorder holds only around the critical point, and not even away from it as before. Indeed, renormalizing $J_s(T)$ by $J_s(0)$ and T by T_c (Fig.4.8), the curves do not collapse one on each other as in the previous case. Moreover, quite surprisingly the effect of the disorder at low temperature is opposite respect to what observed in the experiments. Indeed, in the experimental data preciously shown (Fig.2.8), by effect of the intrinsic inhomogeneity, the superfluid stiffness gets depleted faster in temperature respect to the trend expected for $T < T_c$ exhibiting a symmetric smearing of the J_s jump around T_c. On the contrary, in the case of link dilution, the superfluid stiffness shows a smaller temperature dependence below T_c so that the system seems to become stiffer and stiffer with respect to the clean case as the dilution level increases.

Indeed, with the increase of the link dilution while the diamagnetic term Fig.4.7a keep its temperature dependance almost unchanged, the paramagnetic term Fig.4.7b acquires a negative trend at low temperature whose inclination increase with p. The decrease of J_p at low temperature reflects in the flattening of the superfluid-stiffness,

as highlighted in the renormalized plot of Fig.4.8.

As we will see in the next section, to capture the low-temperature behavior of the three response functions J_s, J_d and J_p, in the case of diluted disorder, the approximated expression of Eq.(4.20) (4.19) are not appropriated anymore: they completely fail in reproducing what numerically found. In this case it is indeed needed to develop an effective medium theory taking into account all the orders of the perturbation expansion around the effective coupling of the system.

4.6 Effective medium theory

The work by Kirkpatrick[33], provides a significant insight on the low temperature superfluid-stiffness response of the disordered XY model. Indeed, in[33] he derives an Effective Medium Approximation (EMA) for the conductance of the Random Resistor Network model (RRN), showing its equivalence with the low-temperature spin stiffness of the XY model with disordered couplings. Looking at the Kirchhoff equation on the single node i:

$$\sum_{\mu=\pm\hat{x},\hat{y}} i_i^\mu = \sum_{\mu=\pm\hat{x},\hat{y}} \frac{1}{R_i^\mu}(V_i - V_{i+\mu}) = 0 \tag{4.27}$$

one can indeed identify the conductance of the single branch with the coupling constants between nearest neighbors spins ($J_i^\mu = \frac{1}{R_i^\mu}$) and, correspondently, the value of the potential on each node with the value of the phase on the single site ($\theta_i = V_i$). With this mapping in mind, it is straightforward to recognise that the electrostatic equation (4.27) can be directly derived from the low temperature expansion of the XY model Hamiltonian:

$$H_{XY} = -\sum_{i,\mu=\hat{x},\hat{y}} J_i^\mu \cos(\theta_i - \theta_{i+\mu}) \simeq -\sum_{i,\mu=\hat{x},\hat{y}} J_i^\mu (1 - \frac{1}{2}(\theta_i - \theta_{i+\mu})^2) \tag{4.28}$$

since from its minimisation one recovers exactly (4.27):

$$\sum_{\mu=\pm\hat{x},\hat{y}} J_i^\mu (\theta_i - \theta_{i+\mu}) = 0 \tag{4.29}$$

Thanks to this equivalence, one identifies the conductance of the RRN model with the stiffness of the XY model. As a consequence, it is possible to use the Effective Medium Approximation to estimate of the zero-temperature value of the spin stiffness. Indeed, the effective conductance σ for a cubic lattice can be derived from:

$$\sum_i P_i \frac{\sigma_i - \sigma}{\sigma_i + (d-1)\sigma} = 0 \tag{4.30}$$

where P_i is for the probability distribution of the on-site conductances σ_i and d is the dimension of the system considered[4].

---

[4]In a more general case in which the lattice is not simply cubic, the factor $(d-1)$ must be replaced with $(z/2-1)$ with z number of nearest neighbors.

By writing: $\sigma_i = \bar{\sigma} + \delta\sigma$, one can further approximate Eq. (4.30) in the limit of small $\delta\sigma$ so that :

$$\sigma = \bar{\sigma}[1 - \frac{\overline{(\delta\sigma)^2}}{d\bar{\sigma}^2}] \tag{4.31}$$

recovering the Eq. (4.20) presented in the previous section. In Eq. (4.31), as well as in the following sections, we will use $\overline{(\dots)}$ to indicate the average over the disorder, while $\langle\cdots\rangle$ for the average over the ensable: $\langle\cdots\rangle = \frac{1}{Z}\int e^{-\beta H}\cdots$.

In this work we face the problem in terms of perturbation theory, showing that the equation (4.30) found by Kirkpatrick in the EMA is the same obtained computing the stiffness via a disorder-induced self-energy at all order in the disorder, in the non-crossing approximation.

Before deriving this important result, let us start simply expanding the disordered XY Hamiltonian (4.14) up to the second-order in the disordered couplings. From this procedure we will recover the approximated estimate of J_s in Eq.(4.20), showing that despite it succeeds in the description of the numerical results obtained for the case of gaussian distributed couplings, it completely fails in describing the diluted model.

4.6.1 Quadratic approximation

Since we are interested in the low-temperature regime, we can start from the continuum limit of H_{XY}, writing it in its gaussian approximated form:

$$H = \frac{1}{2}\int d\mathbf{r} J(\mathbf{r})(\nabla\theta(\mathbf{r}))^2 = \frac{1}{2}\int d\mathbf{r}(\bar{J} + \delta J(\mathbf{r}))(\nabla\theta(\mathbf{r}))^2 = H_0 + H' \tag{4.32}$$

where $\bar{J}$ is the mean value of the couplings and $\delta J(\mathbf{r}) \equiv J(\mathbf{r}) - \bar{J}$ is the local variance with respect to it. We can then rewrite the Hamiltonian as the sum of two terms: the Hamiltonian of a clean system H_0, with uniform and constant couplings equal to $\bar{J}$, and a perturbation term H' with random couplings. Thus:

$$H_0 = \frac{1}{2}\int d\mathbf{r}\bar{J}(\nabla\theta(\mathbf{r}))^2 = \frac{\bar{J}}{2}\sum_{\mathbf{q}}\mathbf{q}^2|\theta(\mathbf{q})|^2 \tag{4.33}$$

$$H' = \frac{1}{2}\int d\mathbf{r}\delta J(\mathbf{r})(\nabla\theta(\mathbf{r}))^2 = \frac{1}{2}\sum_{\mathbf{k},\mathbf{q}}\theta_{\mathbf{k}}\theta_{-\mathbf{k}+\mathbf{q}}\mathbf{k}(\mathbf{q}-\mathbf{k})\delta J_{-\mathbf{q}} \tag{4.34}$$

The problem we are facing here is formally similar to the impurity scattering problem, however instead of averaging over the possible positions of the impurities, the average is made over the probability distribution of the couplings. In other words: impurties are everywhere, but with different intesities according to the disorder probability distribution.

By definition $\overline{\delta J} = 0$, being as before $\overline{\dots}$ the average over the disorder probability distribution. So we get that:

$$\overline{\delta J_q} = \overline{\int d\mathbf{r}\delta J(\mathbf{r})e^{i\mathbf{q}\cdot\mathbf{r}}} = \int dJ P(J)\delta J \int d\mathbf{r}e^{i\mathbf{q}\cdot\mathbf{r}} = 0 \tag{4.35}$$

While for the quadratic term we have:

$$\overline{\delta J_q J_{q'}} = \overline{\int d\mathbf{r} \int d\mathbf{r'} \delta J(\mathbf{r}) \delta J(\mathbf{r'}) e^{i\mathbf{q}\cdot\mathbf{r}} e^{i\mathbf{q'}\cdot\mathbf{r'}}} =_{(\mathbf{r}=\mathbf{r'})} \int d\mathbf{r} \overline{\delta J(\mathbf{r})^2} e^{i(\mathbf{q}+\mathbf{q'})\cdot\mathbf{r}} = \overline{\delta J^2} \delta_{\mathbf{q}+\mathbf{q'}}$$
(4.36)

Indeed, in the presence of spatial uncorrelated disorder the other term of (4.36) is zero:

$$\int d\mathbf{r} \int_{\mathbf{r}\neq\mathbf{r'}} d\mathbf{r'} \overline{\delta J(\mathbf{r})\delta J(\mathbf{r'})} e^{i\mathbf{q}\cdot\mathbf{r}} e^{i\mathbf{q'}\cdot\mathbf{r'}} = \Big[\int dJ P(J)\delta J\Big]^2 \delta_{\mathbf{q}}\delta_{\mathbf{q'}} = 0 \qquad (4.37)$$

By means of equation (4.35)-(4.36) we can now proceed to compute the corrections to the Green's function of the θ variables with respect to (4.34). As we will see, computing the Green function's corrections is equivalent to compute the corrections to the superfluid stiffness J_s.

Let us start from the unperturbed Green's function, whose computation is very easy being the clean Hamiltonian simply gaussian in $\theta(\mathbf{q})$ (4.33):

$$G_q^0 = \overline{\langle\theta_\mathbf{q}\theta_{-\mathbf{q}}\rangle_{H_0}} = \frac{T}{\bar{J}\mathbf{q}^2} \qquad (4.38)$$

where the notation $\langle\ldots\rangle_{H_0}$ indicates the thermal average computed only by means of H_0: $\langle\ldots\rangle_{H_0} = \frac{1}{Z_0}\int\prod_i d\theta_i \ldots \exp(-\beta H_0)$.

Because of (4.35), the first finite order of the expansion in H' is the quadratic term:

$$\frac{1}{Z}\int d\mathbf{q}\overline{\theta_\mathbf{q}\theta_{-\mathbf{q}}e^{\frac{-H_0-H'}{T}}} = G^0 + \frac{1}{2T^2}\overline{\langle\theta_\mathbf{q}H'^2\theta_{-\mathbf{q}}\rangle} + O(H')^3 \qquad (4.39)$$

where the second term reads:

$$\frac{1}{2T^2}\langle\theta_\mathbf{q}\Big(\sum_{\mathbf{k},\mathbf{q'}}\theta_\mathbf{k}\theta_{-\mathbf{k}+\mathbf{q'}}\mathbf{k}(\mathbf{q'}-\mathbf{k})\frac{\delta J_{-\mathbf{q'}}}{2}\Big)\Big(\sum_{\mathbf{k'},\mathbf{q''}}\theta_{\mathbf{k'}}\theta_{-\mathbf{k'}+\mathbf{q''}}\mathbf{k'}(\mathbf{q''}-\mathbf{k'})\frac{\delta J_{-\mathbf{q''}}}{2}\Big)\theta_{-\mathbf{q}}\rangle =$$

$$= G_\mathbf{q}^0\sum_{\mathbf{q'}}G_{\mathbf{q}+\mathbf{q'}}^0\mathbf{q}\cdot(\mathbf{q}+\mathbf{q'})\,\mathbf{q}\cdot(\mathbf{q}+\mathbf{q'})\frac{\delta J_{-\mathbf{q'}}\delta J_{\mathbf{q'}}}{T^2}G_\mathbf{q}^0$$

(4.40)

In order to generalize the solution for any dimension of the system, let us compute carefully the product $\sum_{\mathbf{q'}}\mathbf{q}\cdot(\mathbf{q}+\mathbf{q'})\,\mathbf{q}\cdot(\mathbf{q}+\mathbf{q'})G_{\mathbf{q}+\mathbf{q'}}^0$. Redefining $\mathbf{q'}$ as $\mathbf{q'}-\mathbf{q}$ we have:

$$\sum_{\mathbf{q'}}G_{\mathbf{q'}}^0(\mathbf{q}\cdot\mathbf{q'})^2 = \sum_{\mathbf{q'},\alpha,\beta}q_\alpha q'_\alpha q_\beta q'_\beta G_{\mathbf{q'}}^0 = \sum_{\alpha,\beta}q_\alpha q_\beta \delta_{\alpha,\beta}\sum_{\mathbf{q'}}q_\alpha'^2 G_{\mathbf{q'}}^0 = \mathbf{q}^2\frac{1}{d}\big(\frac{T}{\bar{J}}\big) \quad (4.41)$$

Finally, substituting it in Eq.(4.40) and performing the average over the disorder by means of Eq.(4.36) and Eq.(4.38) we get:

$$\Sigma_\mathbf{q}^{(2)} = \frac{\mathbf{q}^2}{T}\frac{\overline{(\delta J)^2}}{d\bar{J}} \qquad (4.42)$$

where $\Sigma_{\mathbf{q}}^{(2)}$ stays for the the second order contribution to the full self-energy appearing in the usual Dyson's equation. If we truncate the expansion here, at the quadratic order in the perturbation, we obtain the approximated result:

$$G_{\mathbf{q}}^{-1} = (G^0)_{\mathbf{q}}^{-1} - \Sigma_{\mathbf{q}}^{(2)} = \frac{\mathbf{q}^2 \bar{J}}{T}\Big[1 - \frac{\overline{(\delta J)^2}}{d\bar{J}^2}\Big] \tag{4.43}$$

which, in terms of zero-temperature superfluid stiffness, gives the result we presented before in (4.31):

$$J_s = \bar{J}\Big[1 - \frac{\overline{(\delta J)^2}}{d\bar{J}^2}\Big] \tag{4.44}$$

By means of Eq. (4.16) and Eq.(4.44), we can also identify separately the diamagnetic and the paramagnetic term as:

$$J_d(T = 0) = \bar{J} \tag{4.45}$$

$$J_p(T = 0) = \frac{\overline{(\delta J)^2}}{d\bar{J}} \tag{4.46}$$

The expressions just obtained reproduce well the numerical results found for the spatial uncorrelated disordered XY model with gaussian distributed couplings (Fig.4.4). However, as already stressed, they completely fail in describing what obtained in the case of coupling dilution. Indeed, computing for instance J_p with Eq.(4.46) one gets:

$$J_p(T = 0) = \frac{1}{d(1-p)}\sum_i P_i(J_i - (1-p))^2 = \frac{p(1-p)}{d} \tag{4.47}$$

which for the case of $p = 0.3$ gives $J_p(T = 0) \simeq 0.1$, three times smaller than the value found by MC simulations in Fig.4.7b.

4.6.2 Perturbation theory at all orders of disorder

In order to obtain the correct expression for the response functions of the XY model with any kind of spatially uncorrelated disorder, we will expand the hamiltonian at all the orders in the perturbation H'. Moreover, this time we will proceed in a different way: instead of making an expansion around $\bar{J}$ in (4.32), we will use the same logic of the Kirkpatrick's EMA expanding the $J(\mathbf{r})$'s around an effective value of the coupling $\tilde{J}$:

$$H = \frac{1}{2}\int d\mathbf{r}(\tilde{J} + \delta J(\mathbf{r}))(\nabla\theta(\mathbf{r}))^2 = \tilde{H}_0 + \tilde{H}' \tag{4.48}$$

chosen in such a way that the renormalized Green's function $G_{\mathbf{q}}^{-1}$ reads:

$$G_{\mathbf{q}}^{-1} = \mathbf{q}^2\frac{\tilde{J}}{T} \tag{4.49}$$

As direct consequence, hence, the effective coupling $\tilde{J}$ will exactly correspond to renormalized stiffness at all orders in H'. Let us also notice that, since $\tilde{J} \neq \bar{J}$,

Eq.(4.35) it will be not valid anymore and $\langle \delta J \rangle \neq 0$.

The equation we want to solve is:

$$G_{\mathbf{q}} = \frac{T}{\tilde{J}\mathbf{q}^2} = \sum_{n=0}^{\infty} (-)^n \frac{1}{n!} \langle \theta_{\mathbf{q}} \Big(\frac{\tilde{H}'}{T} \Big)^n \theta_{-\mathbf{q}} \rangle \tag{4.50}$$

the term $n = 0$ corresponds obviously to $G_{\mathbf{q}}^0$, while the n-th term of the sum reads:

$$\langle \theta_{\mathbf{q}} \Big(\frac{\tilde{H}'}{T} \Big)^n \theta_{-\mathbf{q}} \rangle = (-)^n \frac{m_n}{2^n} G_{\mathbf{q}}^0 \, \Sigma_{\mathbf{q}}^{(n)} \, G_{\mathbf{q}}^0 \tag{4.51}$$

where $\Sigma^{(n)}$ is the n-th term of the self-energy summation, corresponding to the n-th diagram in Fig.4.9. The prefactor $\frac{1}{2^n}$ comes from the expression of $\tilde{H}'$ in Eq.(4.48), $(-)^n$ from the contractions of the $\theta_{\mathbf{q_i}} \theta_{-\mathbf{q_i}}$ and m_n stays for the multiplicity of each diagram and it is equal to: $m_n = n! \, 2^n$. Finally, we end up with:

$$G_{\mathbf{q}} = \frac{T}{\tilde{J}\mathbf{q}^2} = G_{\mathbf{q}}^0 \Big(\sum_{n=0}^{\infty} \Sigma_{\mathbf{q}}^{(n)} \Big) G_{\mathbf{q}}^0 \tag{4.52}$$
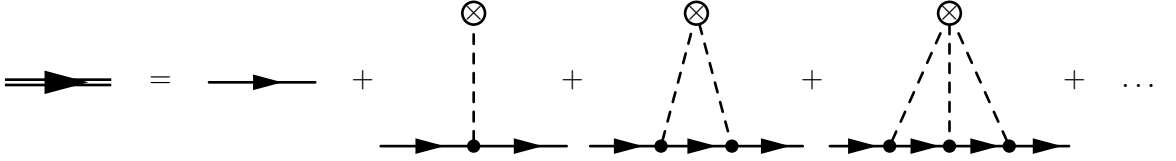
Since the n-th term of the self energy reads:

$$\Sigma^{(n)} = \frac{\mathbf{q}^2}{T} \frac{\overline{(\tilde{J} - J)^n}}{(d\tilde{J})^{n-1}} \tag{4.53}$$

one can write the Dyson's equation of the Green's function as:

$$G_{\mathbf{q}}^{-1} = (G^0)_{\mathbf{q}}^{-1} - \Sigma_{\mathbf{q}} = \mathbf{q}^2 \frac{\tilde{J}}{T} \Big[1 + d \sum_{n=1}^{\infty} \frac{\langle (\tilde{J} - J)^n \rangle}{(d\tilde{J})^n} \Big] \tag{4.54}$$

where: $\Sigma_{\mathbf{q}} = \sum_n \Sigma_{\mathbf{q}}^{(n)}$. The diagrammatic representation of Eq.(4.54) is shown in Fig.(4.9). Each dashed line takes a factor $\propto \overline{(\tilde{J} - J)}/\tilde{J}$ and it connects points on the same position in real space.

Figure 4.9. Diagrams representation of the Green function's Dyson equation.

Finally, in order then to satisfy the request (4.49), we have to impose that:

$$\sum_{n=1}^{\infty} \frac{\overline{(\tilde{J} - J)^n}}{(d\tilde{J})^n} = 0 \tag{4.55}$$

The equation we have just found coincides exactly with the EMA Eq.(4.30). Indeed we have:

$$\sum_{n=1}^{\infty} \frac{\overline{(\tilde{J} - J)^n}}{(d\tilde{J})^n} = \sum_{n=1}^{\infty} \sum_i P_i \frac{(\tilde{J} - J_i)^n}{(d\tilde{J})^n} = \sum_i P_i \sum_{n=1}^{\infty} \frac{(\tilde{J} - J_i)^n}{(d\tilde{J})^n} \tag{4.56}$$

Since $\frac{\tilde{J} - J_i}{d\tilde{J}} = \frac{1}{d} - \frac{J_i}{d\tilde{J}} < 1$ we can put:

$$\sum_{n=1}^{\infty} \frac{(\tilde{J} - J_i)^n}{(d\tilde{J})^n} + 1 = \sum_{n=0}^{\infty} \frac{(\tilde{J} - J_i)^n}{(d\tilde{J})^n} = \frac{1}{1 - \frac{\tilde{J} - J_i}{d\tilde{J}}} = \frac{d\tilde{J}}{(d-1)\tilde{J} + J_i} \qquad (4.57)$$

Hence:

$$\sum_{n=1}^{\infty} \frac{(\tilde{J} - J)^n}{(d\tilde{J})^n} = \frac{d\tilde{J}}{(d-1)\tilde{J} + J_i} - 1 = \frac{\tilde{J} - J_i}{J_i + (d-1)\tilde{J}} \qquad (4.58)$$

So that, finally we get:

$$\sum_{n=1}^{\infty} \frac{\overline{(\tilde{J} - J)^n}}{(d\tilde{J})^n} = \sum_i P_i \frac{\tilde{J} - J_i}{J_i + (d-1)\tilde{J}} = 0 \qquad (4.59)$$

Thus, the equation just derived is exactly Eq.(4.30), with $\tilde{J}$ playing the role of the EMA stiffness (or conductivity in the RRN language).

Once established this important result, we are now interested in going beyond the zero-temperature value of the stiffness, that can be estimate from (4.59), by looking at its leading order in temperature. Together with this purpose, we also want to distinguish between the temperature contributions coming from the diamagnetic and the paramagnetic response function. Thus, starting from the expressions relative to J_d (4.16) and J_p (4.17), we will proceed with the perturbation expansion of H at all orders of H', around the effective value of the coupling $\tilde{J}$. In order to consider the leading terms in temperature, firstly let us expand the two terms J_d and J_p around $\theta_i - \theta_{i+\hat{x}} \simeq 0$:

$$J_d = \overline{\left\langle \sum_i J_i^x \cos(\theta_i - \theta_{i+\hat{x}}) \right\rangle} \simeq \overline{\left\langle \int d\mathbf{r} J(\mathbf{r}) \left[1 - \frac{1}{2} (\nabla_x \theta(\mathbf{r}))^2 \right] \right\rangle} \qquad (4.60)$$

$$J_p = \frac{1}{T} \overline{\left\langle \left[\sum_i J_i^x \sin(\theta_i - \theta_{i+\hat{x}}) \right]^2 \right\rangle} \simeq \overline{\left\langle \int d\mathbf{r} J(\mathbf{r}) \left[\nabla_x \theta(\mathbf{r}) - \frac{1}{6} (\nabla_x \theta(\mathbf{r}))^3 \right]^2 \right\rangle} \qquad (4.61)$$

Starting from the diamagnetic term, the first non vanishing term of J_d in (4.60) is simply:

$$J_d = \overline{\left\langle \int d\mathbf{r} J(\mathbf{r}) \right\rangle}_{H_0 + H'} = \bar{J} \qquad (4.62)$$

Meaning that at all orders in the perturbations, the leading, temperature independent term of the diamagnetic response function is always the mean value of the couplings. The following term $\propto (\nabla_x \theta(\mathbf{r}))^2$, instead, will give us the first order of the J_d temperature dependence. Indeed, separating the term $\tilde{J}$ from its variance we get:

$$\overline{\left\langle \int d\mathbf{r} J(\mathbf{r}) (\nabla_x \theta(\mathbf{r}))^2 \right\rangle}_{H_0 + H'} = \overline{\left\langle \int d\mathbf{r} \tilde{J} (\nabla_x \theta(\mathbf{r}))^2 \right\rangle}_{H_0 + H'}$$
$$+ \overline{\left\langle \int d\mathbf{r} \delta J(\mathbf{r}) (\nabla_x \theta(\mathbf{r}))^2 \right\rangle}_{H_0 + H'} \qquad (4.63)$$

One easily recognise that the first term on the right-hand side is just equal to $T/2d$ at all orders of perturbation in H', thanks to Eq. (4.49). On the other hand, the second term gives:

$$\overline{\langle \int d\mathbf{r} \delta J(\mathbf{r})(\nabla_x\theta(\mathbf{r}))^2\rangle}_{H_0+H'} = \frac{T}{2}\Big[\sum_{n=1}\frac{\langle(\delta J)^n\rangle}{d^n \tilde{J}^n}\Big] \qquad (4.64)$$

Finally, the diamagnetic term at all orders in the perturbation reads:

$$J_d = \bar{J} - \frac{T}{2d}\Big[1 + d\sum_{n=1}\frac{\overline{(\tilde{J}-J)^n}}{d^n \tilde{J}^n}\Big] = \bar{J} - \frac{T}{2d} \qquad (4.65)$$

where we used Eq. 4.55. The diagrammatic representation of Eq. (4.65) is shown in Fig.4.10.
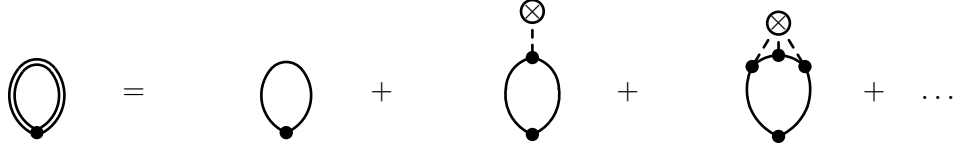
Figure 4.10. Diagramatic representation of the Dyson's equation of the diamagnetic response function J_d.

Quite interesting what we have found, obtained by means Eq.(4.59) in the last passage of Eq.(4.65), tell us that in the presence of spatially uncorrelated disorder, the low temperature trend of the diamagnetic term depends only on the average value of the couplings, showing also an universal linear temperature dependence, with $-1/2d$ as coefficient.

Let us now look at the paramagnetic response function, truncating Eq.(4.61) up to the second order in $\nabla_x\theta(\mathbf{r})$ we get:

$$J_p = \frac{1}{T}\overline{\langle \int d\mathbf{r}'(\tilde{J}+\delta J(\mathbf{r}))(\tilde{J}+\delta J(\mathbf{r}'))\nabla_x\theta(\mathbf{r})\nabla_x\theta(\mathbf{r}')\rangle} \qquad (4.66)$$

The terms of the product proportional to $\tilde{J}$ vanishes, since $\tilde{J}\int d\mathbf{r}\nabla_x\theta(\mathbf{r}) = 0$ with periodic boundary conditions. The first non-vanishing term of the expansion of J_p is then quadratic in δJ:

$$\begin{aligned}
J_p &= \frac{1}{T}\overline{\langle \int d\mathbf{r}\int d\mathbf{r}'\delta J(\mathbf{r})\delta J(\mathbf{r}')\nabla_x\theta(\mathbf{r})\nabla_x\theta(\mathbf{r}')\rangle}_{H_0+H'}\\
&= -\frac{1}{T}\overline{\langle \sum_{\mathbf{q},\mathbf{q}'}\delta J_{\mathbf{q}}\delta J_{\mathbf{q}'}q_x q_x'\theta_{-\mathbf{q}}\theta_{-\mathbf{q}'}\rangle}_{H_0+H'}\\
&= \frac{1}{T}\overline{\langle \sum_{\mathbf{q},\mathbf{q}'}\delta J_{\mathbf{q}}\delta J_{\mathbf{q}'}q_x q_x'\theta_{-\mathbf{q}}\theta_{-\mathbf{q}'}\Big[1 - \frac{H'}{T} + \frac{1}{2}\Big(\frac{H'}{T}\Big)^2 + \dots\Big]\rangle}_{H_0}
\end{aligned} \qquad (4.67)$$

Using as usual $\overline{\delta J_{\mathbf{q}_1}\dots\delta J_{\mathbf{q}_1}} = (\delta J)^n\delta_{\mathbf{q}_1+\dots\mathbf{q}_n}$, as before, one can compute the lowest orders of the expansion and afterwards generalise the result to every order, finally

obtaining the complete resummation of J_p. It is easy to verify that the first term gives:

$$\frac{1}{T}(\delta J)^2 \sum_{\mathbf{q}} q_x^2 G_{\mathbf{q}} = \frac{1}{dT}(\delta J)^2 \frac{T}{\tilde{J}} \tag{4.68}$$
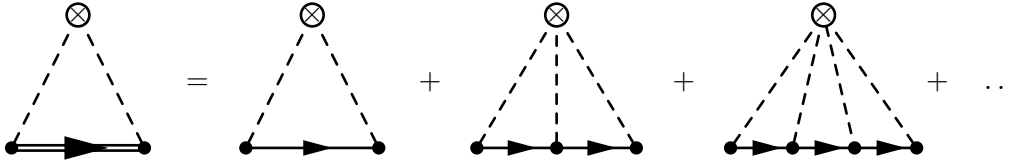
while the second term reads:

$$\frac{1}{d^2 T^2}(\delta J)^3 \Big(\frac{T}{\tilde{J}}\Big)^2 \tag{4.69}$$

In summary, at all orders in H', the resummation of the paramagnetic term will read:

$$J_p = d\tilde{J} \sum_{n=2}^{\infty} \frac{\overline{(\tilde{J} - J)^n}}{(d\tilde{J})^n} \tag{4.70}$$

whose diagrammatic representation is shown in Fig.4.11

Figure 4.11. Diagramatic representation of the Dyson's equation for the paramagnetic response function.

It is crucial to notice that in Eq.(4.70) the sum starts from $n = 2$, since the paramagnetic term is at least quadratic in δJ. Using again Eq.(4.55), we can write it as:

$$J_p = d\tilde{J} \sum_{n=2}^{\infty} \frac{\overline{(\tilde{J} - J)^n}}{(d\tilde{J})^n} = d\tilde{J}\Big[\sum_{n=1}^{\infty} \frac{\overline{(\tilde{J} - J)^n}}{(d\tilde{J})^n} - \frac{\overline{(\tilde{J} - J)}}{d\tilde{J}}\Big] = -\overline{(\tilde{J} - J)} \tag{4.71}$$

Finally, having derived the paramagnetic zero temperature term, it is straightforward to verify, by subtracting it to $J_d(T = 0)$, that the value of the superfluid stiffness at zero temperature is exactly the effective coupling $\tilde{J}$, as required from Eq.(4.49):

$$J_s = J_d - J_p = \bar{J} + \overline{(\tilde{J} - J)} = \tilde{J} \tag{4.72}$$

Nevertheless, if we wanted to obtain the first contribution in temperature of the paramagnetic response function, as derived for the diamagnetic term, we should consider the higher term in Eq.(4.61) and also take into account the following term of the original XY Hamiltonian expansion (4.32). We will not address this issue here, where we will just discuss a phenomenological derivation. However, with the results just obtained (4.65) and (4.71), we can already see that the derived values of J_d, J_p and J_s at $T = 0$ are really in good agreement with what found numerically. Let us look in particular at the diluted case, for which the quadratic approximation (4.46) fails. By means of Eq.(4.59), (4.71) and (4.65), the zero temperature values of J_s, J_p and J_d read:

$$
\begin{cases}
J_s & = 1 - 2p \\
J_d & = \bar{J} = 1 - p \\
J_p & = p
\end{cases}
\tag{4.73}
$$

Indeed applying (4.59) to the case of a two-dimensional system with link dilution one gets: $\sum_i \frac{P_i(\tilde{J}-J_i)}{J_i+\tilde{J}} = (1-p)\frac{\tilde{J}-1}{1+\tilde{J}} + p = 0$, from which it is straightforward to find $J_s = 1 - 2p$. The results of (4.73) are in good agreement with the zero temperature values found by MC simulations for the case of link dilution, as highlighted in Fig4.12a and 4.12b.
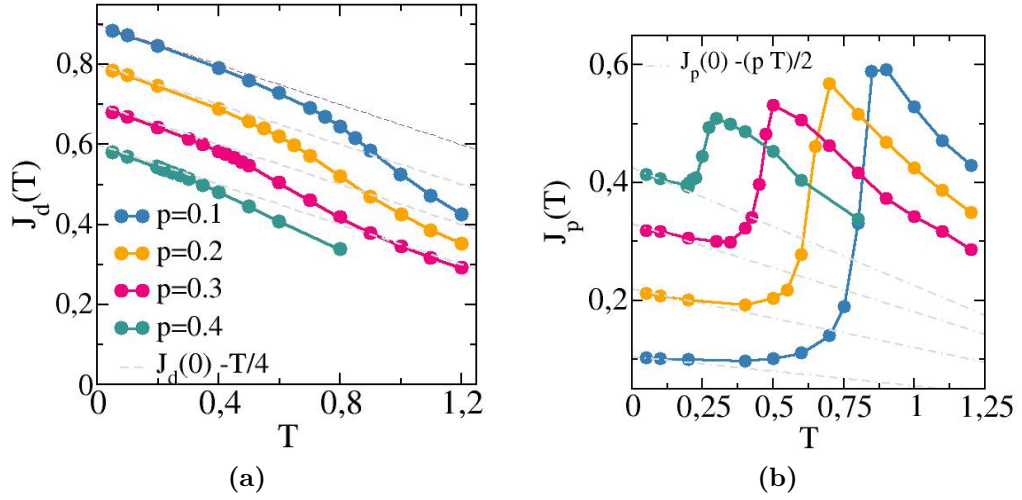
Figure 4.12. (a) Diamagnetic J_d and (b) paramagnetic J_p term as function of the temperature for different values of the coupling dilution p. The dashed gray line represent the fit obtained from the low temperature perturbation theory at all orders in H' for J_d and via a phenomenological argument for J_p.

Finally, while in the case of gaussian distributed couplings, for every value of σ, the paramagnetic term is almost flat at low temperature (Fig.4.4b), in the case of link dilution J_p linearly decreases in temperature with a coefficient somehow proportional to the dilution p. Quite interesting, such dependence can be recovered by substituting in Eq.4.59 $J_i \to J_i - \frac{T}{2d}$, getting:

$$
J_s = (1 - 2p)(1 - \frac{T}{2d})
\tag{4.74}
$$

Since from Eq.(4.65) we know that:

$$
J_d = \bar{J} - \frac{T}{2d} = (1 - p) - \frac{T}{2d}
\tag{4.75}
$$

The paramagnetic term reads:

$$
J_p = p(1 - \frac{T}{d})
\tag{4.76}
$$

This procedure is certainly not rigorous, since one in principle should consider the highest order in Eq.(4.61) computing the full sum at all orders in H', however the phenomenological result obtained in Eq.(4.76), reproduces very well the low temperature trend of the paramagnetic response function (Fig.4.12b).

In summary, from this study we showed that the spatially uncorrelated disorder is irrelevant on the BKT transition and in some cases (as for the Gaussian-distributed random couplings) even away from criticality. This is due to the universality of the spin-wave excitations with respect uncorrelated disorder, that we have demonstrated by means of a perturbation expansion around an effective stiffness, according to the EMA idea for the RRN model. This work is actually under preparation and it will be soon available online.

Chapter 5

2D XY model: spatially correlated disorder

As discussed in the previous chapters, tunneling spectroscopy on several conventional superconductors such as NbN, InO_x and TiN has shown that the local order parameter, as probed by the local density of states, is strongly inhomogeneous, forming domains of good and bad SC regions with a size of a few times the coherence length[84, 95, 97, 35]. These experimental observations have raised the issue of how such mesoscopic heterogeneity modifies the superconducting properties of the system and indeed in the last years a lot of efforts have been devoted to the study and characterisation of disordered superconductors. In particular, the emergent granularity observed can be reproduced by the effective quantum XY pseudo-spin-1/2 model in a transverse random field (RTF)[36, 93, 34]:

$$\mathcal{H}_{PS} \equiv -2 \sum_i \xi_i S_i^z - 2J \sum_{\langle i,j \rangle} \left(S_i^+ S_j^- + h.c. \right). \tag{5.1}$$

As already discussed in the third chapter, within the bosonic picture of the model the pairing degrees of freedom are frozen, and disorder induces a direct SIT, as seen experimentally[97]. In pseudo-spin language, superconductivity corresponds to a spontaneous in-plane magnetization, favored by the coupling J of (5.1), while the random transverse field ξ_i , box distributed between $-W$ and W , tends to align the local spin along z, mimicking the localisation of Cooper pairs due to disorder. At the mean-field level we have previously shown that the local magnetization forms an angle ϕ_i^{PS} with respect to the z axis, with ϕ_i^{PS} approaching 0 as W/J increases. For every given realisation of the disordered ξ_i's in Eq.(5.1), we have derived the mean-field solutions of the local magnetizations ϕ_i^{PS}'s and the correspondent values of the local stiffness, being $J_i^\mu = J \sin(\phi_i^{PS}) \sin(\phi_{i+\mu}^{PS})$. The resulting maps of J_i^μ, shown in Fig.3.8, reproduce the salient features of the experiments[84, 35]: every J_i^μ is on average suppressed by disorder, and it tends to segregate in *bad* SC regions embedding a *good*, filamentary[36] SC structure. In view of that, after having considered the case of spatially uncorrelated disorder, in this chapter we will consider the case of correlated disorder by using as disordered couplings for the two-dimensional XY model exactly those local stiffness J_i^μ obtained from the bosonic model (5.1):

$$H_{XY} = - \sum_{i,\mu=\pm x,y} J_i^\mu \cos(\theta_i - \theta_{i+\mu}) \qquad (5.2)$$

Hence, in this chapter we investigate the effects of classical phase fluctuations on top of this inhomogeneous SC ground state, addressing the issue of whether and in which way such granularity affects the BKT phase transition.

5.1 Correlated disorder: broadening of the BKT universal jump

With the increase of the disorder strength, together with the emergence of spatial inhomogeneity within the system, we have also seen in the previous chapters (Fig. 3.3, Fig. 3.4, Fig. 3.9) that the probability distribution of the SC order parameter moves its average towards lower values, getting more and more broadened. The probability distribution of the J_i^μ's, derived from the bosonic model (5.1), share as well the same characteristics, as reported in Fig.5.1(a).
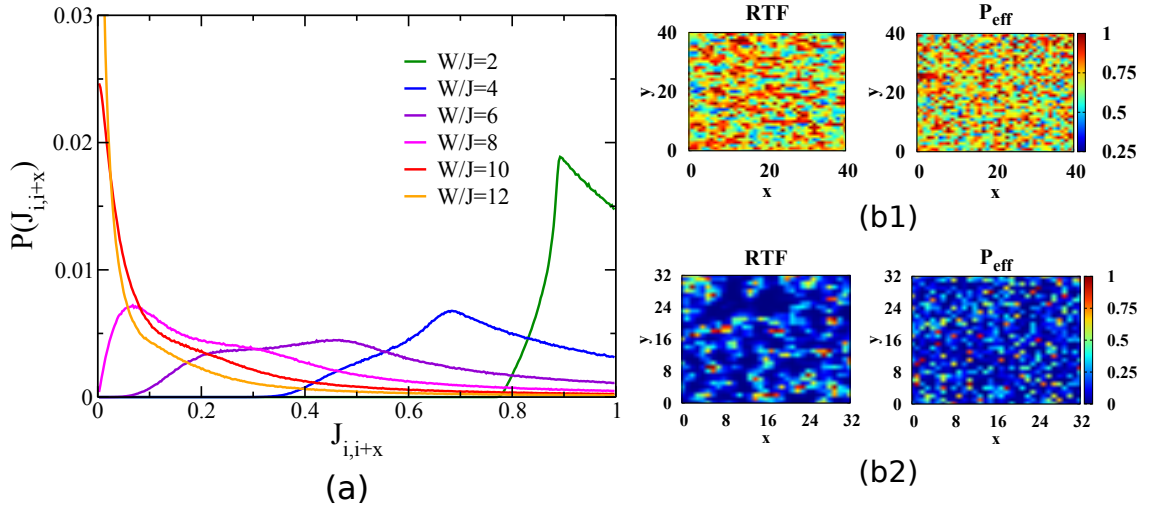

Figure 5.1. (a)Coupling distributions for different values of the disorder strength W/J. Maps of the couplings J_i^x both in the presence of spatial correlations (RTF) and without (P_{eff}) for two level of disorder strength: (b1) W/J=4 and (b2) $W/J = 10$

In light of this, to disentangle the effects of the spatial correlations of the couplings from the ones connected to their probability distribution, we also compute for each disorder level the stiffness of the effective, uncorrelated distribution P_{eff}. This means that we assign the value J_i^μ to each link by extracting it randomly from the same probability distribution $P_{eff}(J_i^\mu)$ which represents the RTF maps. In this case, the SC state does not show any evident aggregation in real space, giving rise to standard, uncorrelated disorder, as it is already evident in the maps shown in Fig.5.1(b1) and (b2). The zero-temperature value of the superfluid stiffness, computed both in the RTF and P_{eff} case, turns out to be dependent only on the disorder probability distribution, regardless of its spatial correlations. Moreover, the value of $J_s(T = 0)$ obtained by Monte Carlo simulations shows a very good agreement with

the approximated expression $J_s^{app} = \bar{J}\left[1 - \frac{\overline{(\delta J)^2}}{d.\bar{J}^2}\right]$, discussed in Chapter 4, even up to large values of the disorder strength, as reported in Fig.5.2.

Nevertheless, the effect of the spatial correlations comes into play as soon as the whole temperature dependence of the superfluid stiffness is taken into account.
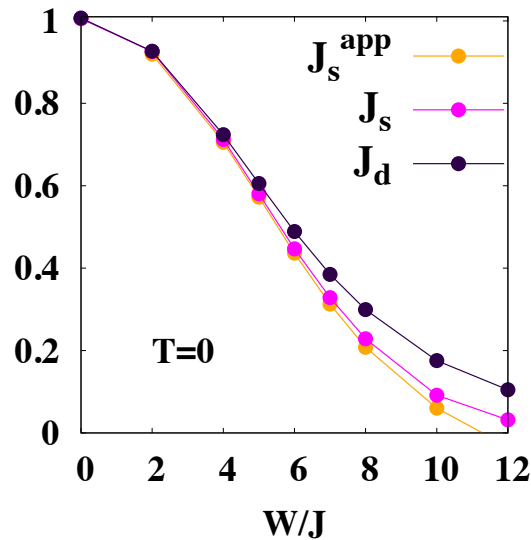
Figure 5.2. Evolution with disorder of the zero-temperature value of J_s and J_d for the RTF model and of the approximated result J_s^{app} from (4.44).

The evolution of the superfluid stiffness, computed by means of Monte Carlo simulations for increasing disorder level W/J, is shown in Fig. 5.3. At low disorder level, $W/J = 4$ (Fig.5.3(a)), the qualitatively trend of J_s stays almost unchanged respect to the clean case. The only remarkable effect of the presence of disorder, as for the case of gaussian distributed couplings, is the depletion of the zero temperature value of J_s and consequently the reduction of the critical temperature T_c. Moreover, the two curves (the red and the green one) of the superfluid stiffness, corresponding respectively to the spatial correlated disorder (RTF) case and to the spatial uncorrelated (P_{eff}) one, overlap perfectly one on each other. For this disorder level, indeed, the maps of their local stiffness (Fig.5.3(a1)) look very similar, meaning that the couplings aggregation occurring in the RTF case is not enough pronounced for $W/J = 4$. Finally, at this level of disorder, also the probability distribution of the couplings (Fig.3.9) has not the characteristic quasi lognormal distribution observed for higher disorder. On the other hand, at strong disorder, $W/J = 10$, we recover both the logarithmically large probability distribution, peaked at low values of the local stiffness, and for the RTF case a much more evident aggregation of the couplings in real space (see Fig.5.3(a)). From Fig.5.3(b), it is clear that despite the strength of the disorder and its wide probability distribution, the absence of spatial correlations among the couplings leaves the critical behavior of the superfluid stiffness unchanged, the green curve correspondent to the P_{eff} case indeed shows a sharp jump at the intersection with the critical line. On the contrary, the presence

of large enough regions of low couplings, embedding filamentary regions of higher couplings, qualitatively changes the superfluid stiffness trend which starts showing a symmetric broadening around the critical temperature T_c.
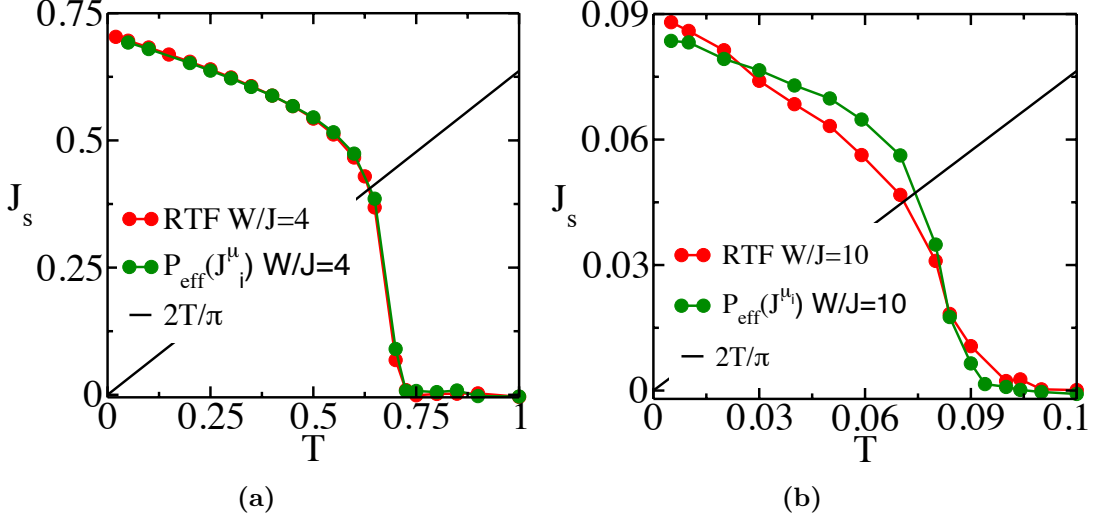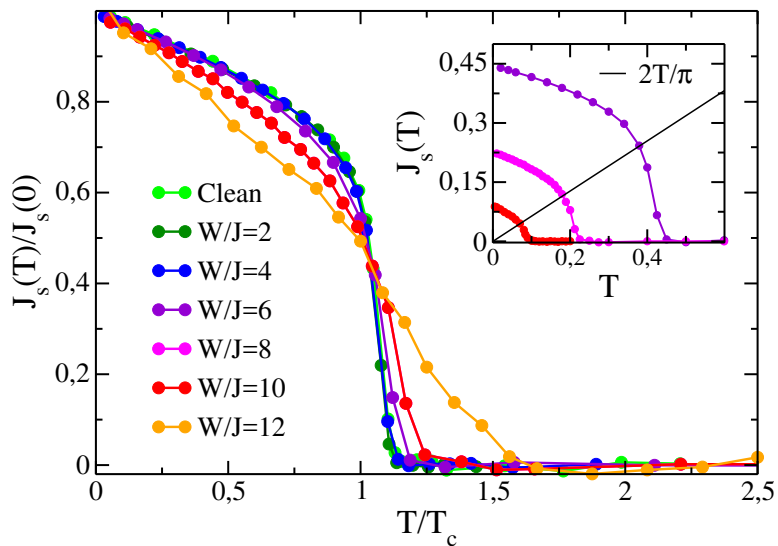

Figure 5.3. Temperature dependence of the superfluid stiffness in the two cases of disordered considered: with spatial correlation (RTF) and without (P_{eff}) for two different disorder levels. At weaker disorder (a) the two curves overlap and the jump of J_s is still sharp. At larger disorder (b) the curve for the RTF case starts to deviate from the usual trend, showing an almost symmetric smearing of the jump around the critical temperature.

Looking at the rescaled curves in Fig.5.4, the irrelevance of spatially uncorrelated disorder on the BKT transition is even more evident: the green curve correspondent to the P_{eff} case, despite the strong disorder level ($W/J = 12$) considered, continues to show the same qualitatively trend of the homogeneous case, showing only a little tail for $T > T_c$ likely due to finite size effects. At the same time, in Fig.5.4 it is also highlighted the symmetric smearing of the BKT jump in the presence of spatial aggregations of couplings: the RTF superfluid stiffness curve seems to completely loss the jump decreasing in temperature with almost the same temperature dependence both below and above T_c.

Finally, in Fig.5.5 the rescaled curves of the superfluid stiffness, obtained in the presence of RTF disordered couplings, are shown for different value of the disorder strength W/J. The symmetric smearing of the universal stiffness jump, absent at weak disorder, starts to be visible around $W/J \simeq 6$ increasing with the increase of W/J. At the same time, the $T = 0$ suppression of the stiffness (shown in the inset of Fig.5.5), as we have discussed above, is well captured by the approximated expression (4.20) up to large values of W/J (see Fig.5.2).
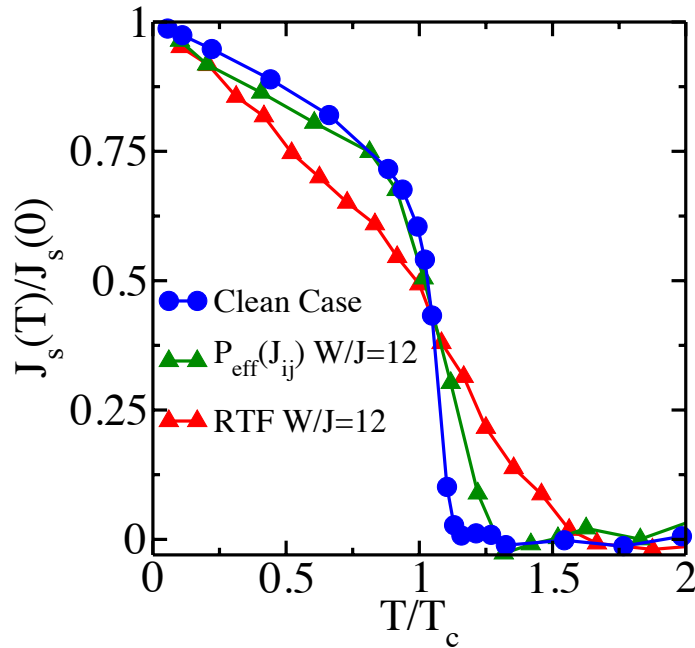
Figure 5.4. Rescaled curves of the superfluid stiffness for the clean case, the uncorrelated P_{eff} and correlated RTF disordered case at $W/J = 12$. Despite the strong disorder the P_{eff} curve shows only a small finite-size effect above T_c, while the RTF stiffness is dramatically modified above and below the transition.

Figure 5.5. Temperature dependence of the superfluid stiffness for the RTF model at various disorder level, rescaled to the value of $J_s(0)$ and to T_c, defines as the intersection with the universal $2T/\pi$ line, see inset. For comparison we also report the clean case, to emphasize the remarkable universality of the rescaled curve up to relatively large disorder level.

5.2 Anomalous Vortex-Antivortex nucleation

To get a deeper insight on the role of the spin-wave and vortex excitations contributing to the symmetric broadening of the superfluid stiffness in the presence of spatially correlated disorder, we show in Fig.5.6 the temperature evolution of J_s together with the two separate diamagnetic (4.4) and paramagnetic (4.5) contributions, and with the average density ρ_V of vortex pairs. The latter one is defined by computing the local (positive or negative) vorticity of the phase around each square plaquette of the array, without distinguish between bound pairs of vortices and free ones.

(a)

(b)   **(c)**
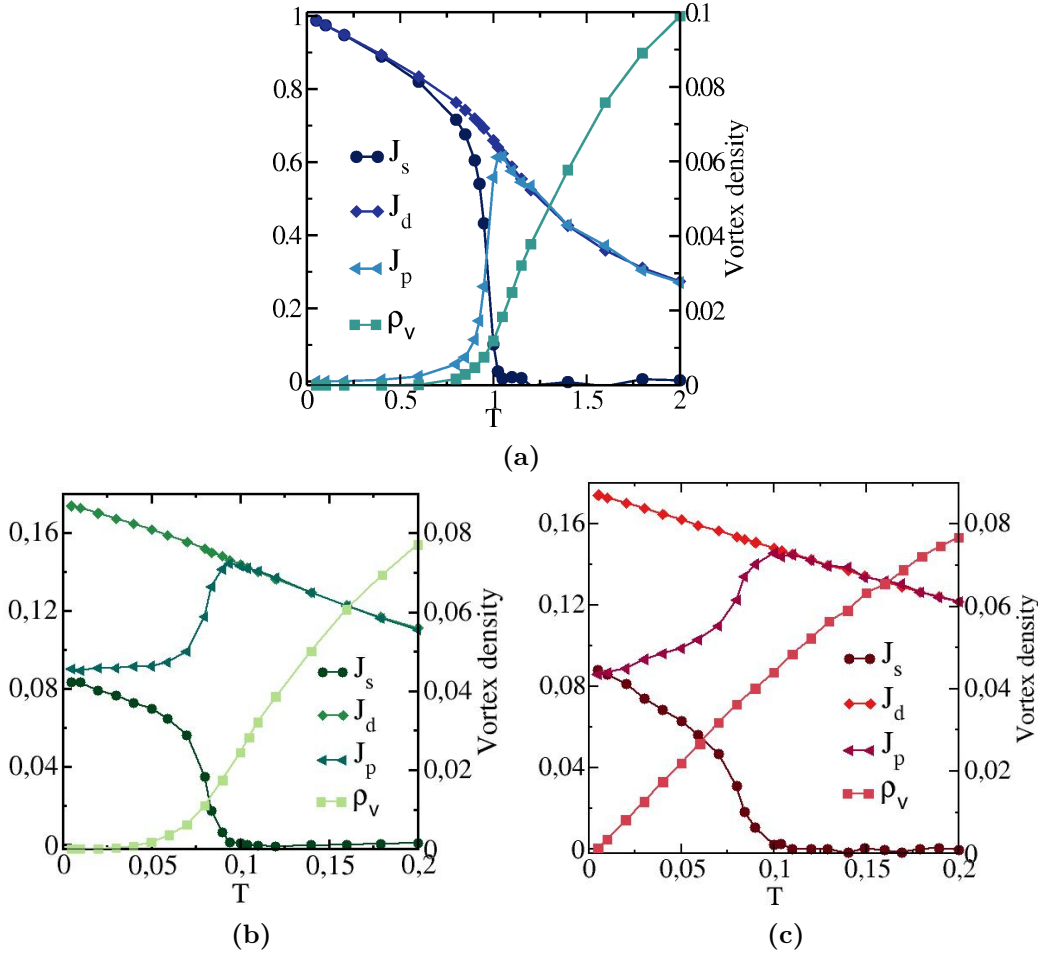
Figure 5.6. Temperature dependence of the superfluid stiffness J_s, the diamagnetic term J_d, the paramagnetic term J_p and the vortex pair density ρ_v for three different cases: (a) Clean case, (b) Uncorrelated disorder P_{eff} with $W/J = 10$ and (c) Correlated disorder RTF with $W/J = 10$.

In Fig.5.6a we show the results for the clean case. As discussed in the previous chapter, spin-waves dominate the behavior of J_d and J_p at low temperatures. The vortex density is exponentially suppressed at low T and it increases sharply at $T \simeq 0.9$, bringing up the paramagnetic contribution, which grows fast leading to $J_p = J_d$ at $T \simeq 1$. A similar trend is observed at $W/J = 10$ for the P_{eff} case, see

Fig.5.6b. Indeed, apart from the sizeable finite corrections to J_d and J_p at $T = 0$, that can be captured by the approximated expression of J_s (4.20), the thermal evolution of the various contributions is essentially the same: the vortex density has a fast increase only at $T \simeq 0.075$, where the universal jump is indeed expected (see Fig.5.6b). Instead, the results change considerably for the RTF model, Fig.5.6c. In particular, we observe an anomalous smooth increase of the paramagnetic response at low temperature, followed by a faster one around the temperature scale where the universal jump should be observed. This unconventional paramagnetic response explains the symmetric broadening of the transition observed in Fig.5.6c. A second striking result is the almost linear increase of the vortex density in the whole temperature range, which raises the issue whether such correlated disorder changes or not the BKT universality class of the transition. We will face this issue in the last section of this chapter by means of the finite size scaling study.

To get deeper insight into the anomalous behavior of J_p at strong disorder, we investigated the vortex nucleation mechanism in real space. As we explained above, a distinct characteristic of the RTF model is the emergence of large clusters of bad SC regions, where the local stiffness is small. Vortices can then proliferate inside these regions already at low temperatures, as shown in Fig.5.7, where the local vorticity is superimposed on the color map of the local stiffness for different value of the temperature. In contrast, in the P_{eff} case the bad regions remain small, and vortex formation cannot be confined in low-coupling clusters. Furthermore, the anomalous nucleation of the RTF case, as we will see in details in the last section of this chapter, does not disappear as the size of the system is increased, suggesting that the effects observed here are very different from the usual rounding of the stiffness above T_c due to conventional finite-size effect.

The direct connection between J_p and ρ_V in the RTF model will be deeper investigated in the fifth section of this chapter, by adding explicitly to the model (5.2) a chemical-potential term weighting the finite vortex density. We will see that while for the homogeneous case the only effect of this term is to shift the transition to higher temperatures, for the RTF case it strongly modifies both J_p and ρ_V at low T, showing that for correlated disorder, vortex-antivortex pairs are relevant already below T_c, in contrast to what was shown in Fig.5.6b for uncorrelated disorder.

Finally, it is worth to highlight the difference between the RTF model and the diluted one. Indeed, also for high values of the link dilution one could expect a sort of aggregation of bad and good couplings regions. Thus, consequently, an anomalous vortex-antivortex pairs nucleation within bad couplings regions could be expected as well. However, from Fig.4.6 and 4.7b no anomalous increase of the paramagnetic term is observed, as well as no smearing below T_c of J_s. Surprisingly, the effect observed there is instead the opposite one: the system, below T_c, is even more stiff respect to the homogeneous case.

This apparently counterintuitive result, can be easily understood once considered that the diluted model allows only zero or one, as possible value for the couplings. Indeed, this constraint makes costless vortices nucleation in bad regions, but at the same time it keeps them strictly confined within such bad regions, creating infinite high barriers between good and bad clusters for any $T < T_c$. In other words, even if vortices can be nucleated below T_c, they can not move neither contaminate the other regions of the system, having hence no effect on the global superfluid stiffness.
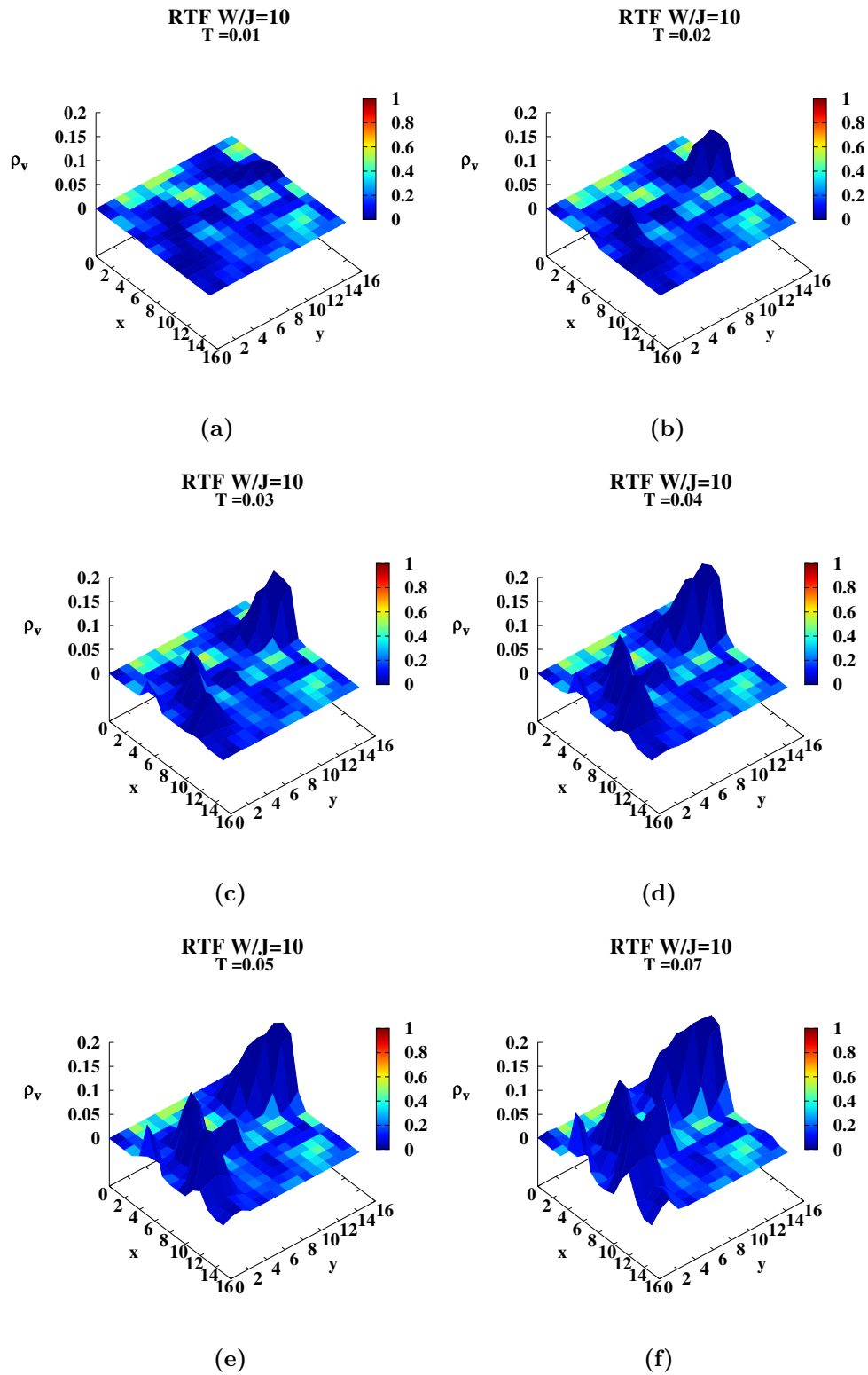
Figure 5.7. Local vortex density ρ_V at different temperatures superimposed to the color map of the local stiffness J_{ij} for the RTF model. All the temperatures considered here are below T_c, nevertheless the vortex density is finite due to the pairs nucleation within cluster of low couplings.

5.3   Discussion on the I-V charachteristics

As we mentioned in the second chapter, the broadening of the superfluid-stiffness jump in the presence of correlated disorder can be accessed experimentally in SC thin films either via direct measurements of the inverse penetration depth, which is proportional to the superfluid density, or via the *I-V* characteristic exponent. In the latter case one can take advantage of the ability of a finite current to unbind a vortex-antivortex pair below T_c, generating a finite density ρ_V of free vortices, which contribute to dissipation[43]. In general one then expects non-linear *I-V* characteristics with an anomalous exponent $a(T)$:

$$V \propto I^{a(T)}, \quad a(T) = 1 + \pi J_s(T)/T \tag{5.3}$$

In the homogeneous case the universal jump of the stiffness at T_c, $J_s(T_c) = 2T_c/\pi$ reflects in the universal jump of the exponent a from $a = 3$ right above the transition to $a = 1$ right below it.
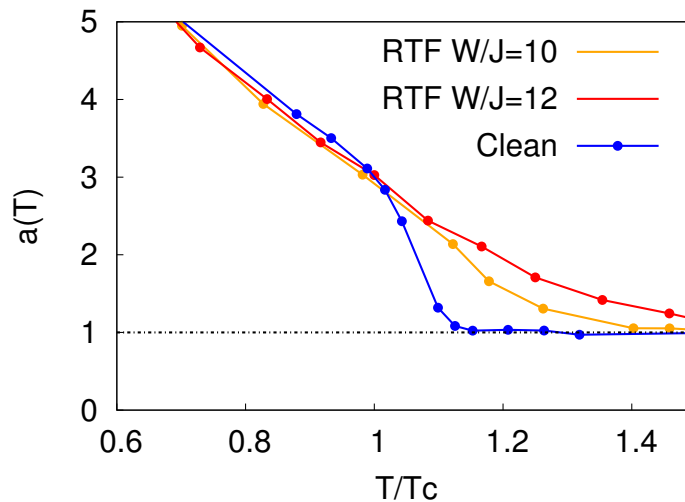
Figure 5.8. Temperature dependence of the *I-V* exponent for the clean and the RTF case as a function of T/T_c. As usual, we define T_c as the intersection of $J_s(T)$ with the universal $2T/\pi$ line, so $a(T_c) = 3$. While for the clean case we observe the rapid downturn of $a(T)$ from 3 to 1, in the RTF case we find a smooth suppression, consequence of the smearing of the $J_s(T)$ jump due to disorder.

In the experiments[102]-[73] such a jump is only verified at a qualitative level, for two reasons: (i) it is very difficult to determine the exponent near to T_{BKT}, where the critical current to break Cooper pairs becomes very small and (ii) the inhomogeneity smears out the $J_s(T)$ jump, and this reflects in the behavior of the $a(T)$ exponent. While a direct computation of the *I-V* characteristic is well beyond the scope of this work, we can nonetheless estimate $a(T)$ by using the same relation (4) with $J_s(T)$ known for the homogeneous case. The results are shown in Fig.5.8, where we determine $a(T)$ in the XY model for the clean and the disordered case. While for the clean case the rapid downturn of $a(T)$ can be clearly identified, in the case of correlated disorder the crossover from $a = 3$ to $a = 1$ is rather smooth, in agreement

with experimental observations[102]-[73]. It is worth noticing that when the disorder-induced inhomogeneity is absent the rapid downturn of $a(T)$ after the intersection with the universal line can be more easily identified also in the experiments, as seen for example for recent transport measurements in thick films of underdoped cuprate superconductors[11].

## 5.4   Characterisation of the correlated disorder

To quantify the differences between the RTF and the P_eff cases for what concerns the space correlations of disorder we analyze the clusterisation effects in the two models. We first need to identify the connected clusters of "*good*" and "*bad*" couplings separately. Starting from the maps of J_i^μ we define "*good* connected cluster" the connected groups of couplings whose value is bigger than a given threshold αJ_s, where J_s is the zero-temperature stiffness and α is a number which fixes the threshold "*bad* connected cluster" are the connected groups with a value of the coupling smaller than αJ_s. The results of this differentiation for $\alpha = 1$ are shown in Fig.5.9. The algorithm used for the definition of such connected clusters is a simplified version of the Holshen and Kopelman algorithm[103]. It assumes that two sites belong to the same cluster only if they differ by a single lattice spacing.

To measure the dimension of each type of connected cluster we computed the mean value of their size:

$$\langle S \rangle = \frac{1}{N_\gamma} \sum_\gamma s_\gamma = \frac{1}{N_\gamma} \sum_\gamma \sum_{i \in c_\gamma} n_i \tag{5.4}$$

where γ is the index of the cluster and N_γ is the total number of the connected clusters considered. In Fig.5.10 we report the mean value of the cluster size for both the P_{eff} and the RTF models as function of the disorder strength W/J. While in the P_{eff} case, the mean value of the clusters size is almost constant with increasing disorder, in the RTF case the granularity of the disorder increases with the disorder strength: both the *good* and the *bad* regions of couplings progressively enlarge their size. As we discussed in the previous sections, the generation of large clusters with low coupling is particularly important for the vortex nucleation mechanism, since in these regions vortex-antivortex pairs can easily nucleate even at temperatures much smaller than the average stiffness. The existence of spatial correlations is further emphasized by the cluster-size dependence on the coupling threshold α. As shown in Fig.5.11 in the RTF model the dimension of the *bad* regions depend significantly on α, while for the uncorrelated P_{eff} case the size of *bad* clusters is independent on it, showing the absence of any characteristic correlation length for the disorder. Notice that a pronounced cluster-size dependence on the disorder level has been identified experimentally also in disordered films of NbN by means of tunneling measurements[35].

(a)

(b)

(c)

(d)
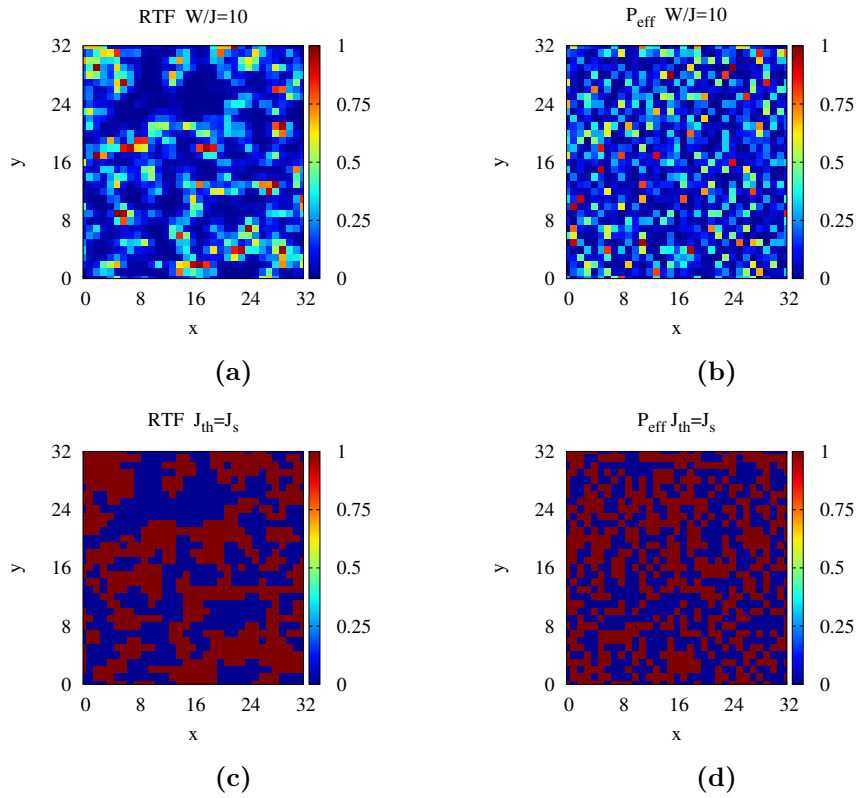
**Figure 5.9.** Top: Maps of the couplings in real space respectively for the P_{eff} and the RTF disordered model with $W/J = 10$. Bottom: Bimodal maps of the clusters in real space, realized from the maps of the coupling in (a) and (b) for a value $\alpha = 1$ of the threshold.

(a)

(b)
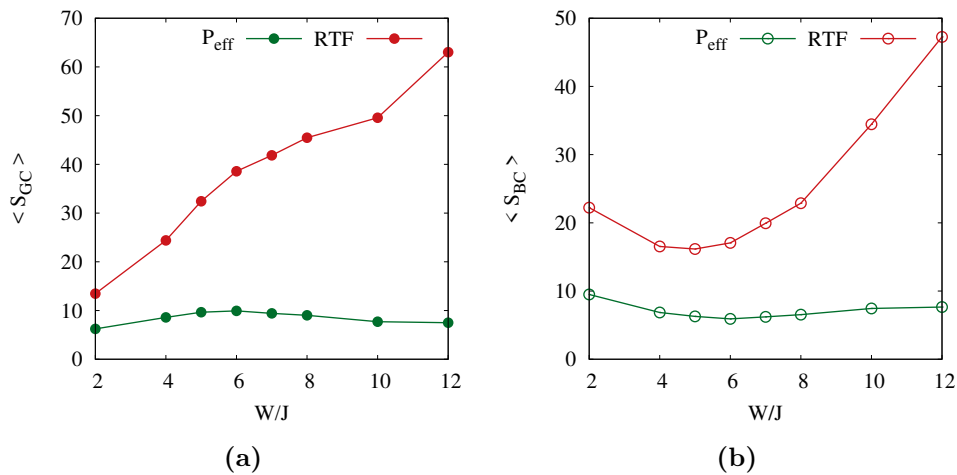
Figure 5.10. Disorder dependence of the mean cluster size for (a) good (S_{GC}) and (b) bad (S_{BC}) clusters for both the P_{eff} and the RTF case. Here the threshold is $\alpha = 1$.
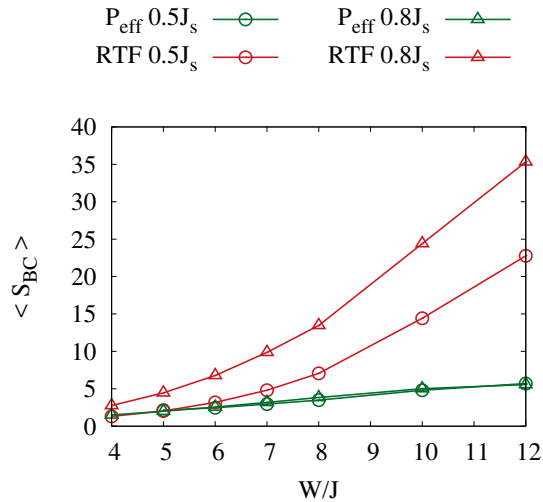
Figure 5.11. Disorder dependence of the mean cluster size of the bad clusters for both the P_{eff} (green) and the RTF (red) case at different level of the cluster threshold $\alpha = 0.8$ and $\alpha = 0.5$. While in the P_{eff} case the cluster size is independent on the threshold, for the RTF case one observes a progressive increase of the bad SC regions as the threshold increases

5.5 Effects on the vortex-antivortex pairs on the low-temperature stiffness

As shown in the previous sections, the temperature dependence of the paramagnetic contribution J_p to the stiffness acquires an anomalous behavior at strong disorder, where also the vortex-antivortex pair density ρ_V shows a fast increase with temperature, to be contrasted with the homogeneous or uncorrelated disordered case. To establish a more closely connection between J_p and ρ_V we performed Monte Carlo simulations on a modified XY model, where we add explicitly and additional energetic cost for the vortex-pair formation:

$$H^{\mu}_{XY} = -\sum_{\langle i \rangle j} J_{ij} \cos(\theta_i - \theta_j) + \mu \sum_p |n_v(p)| \tag{5.5}$$

where $n_v(p)$ is the number of (positive or negative) vortices on each plaquette and the index p runs over all the plaquettes of the lattice.

In the conventional homogeneous case, the additional term in Eq.(5.5) is to some extent equivalent to increase the vortex-core energy. One then expects, on the basis of standard renormalization-group results[82], that the transition temperature shifts to higher values. This is indeed confirmed by our Monte Carlo simulations for the homogeneous case, shown in Fig.5.12. As one can see, the temperature needed to generate vortex-antivortex pairs is higher, and consequently the renormalization of the stiffness due to bound pairs softens, moving the superfluid-stiffness jump to higher temperatures as compared to the case $\mu = 0$. On the other hand, the low-temperature behavior of the paramagnetic current is unaffected, and its sudden jump at T_c is rigidly shifted.
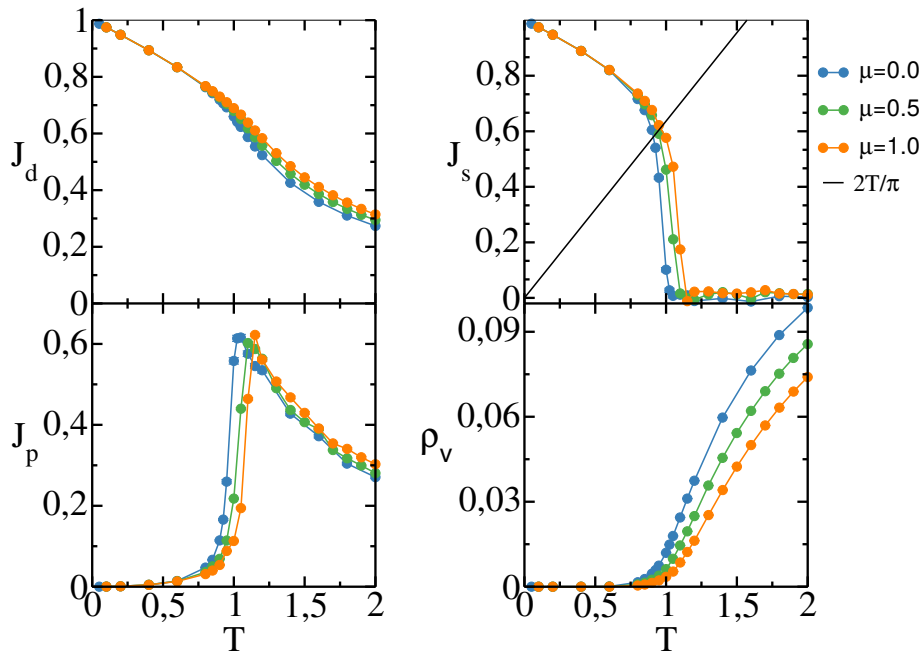
Figure 5.12. Temperature dependence of the superfluid stiffness J_s , its diamagnetic J_d and paramagnetic J_p component, and the vortex density ρ_V for the homogeneous (clean) case with a finite chemical-potential term, as in Eq.(5.5)
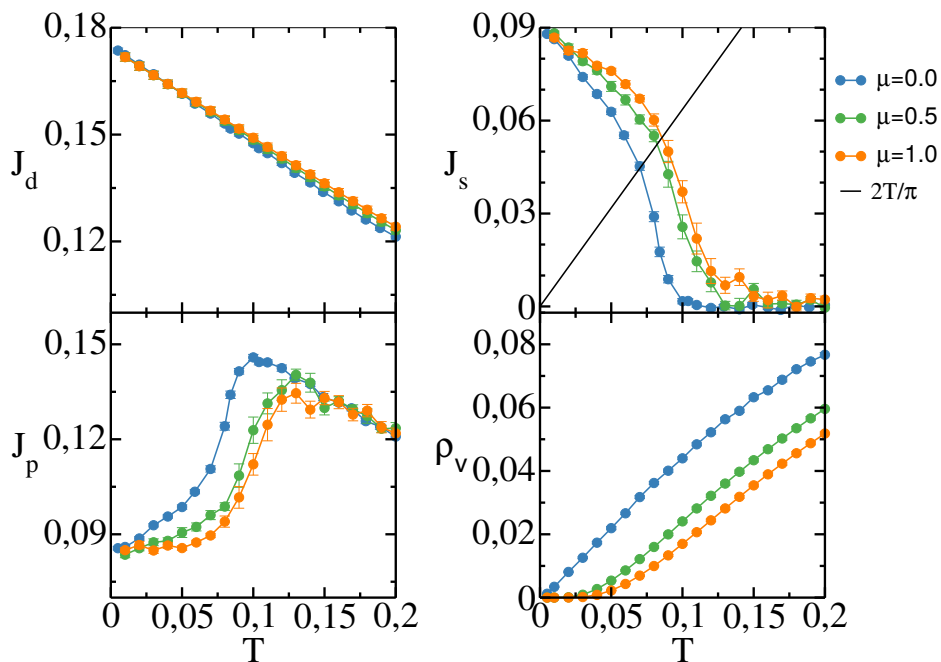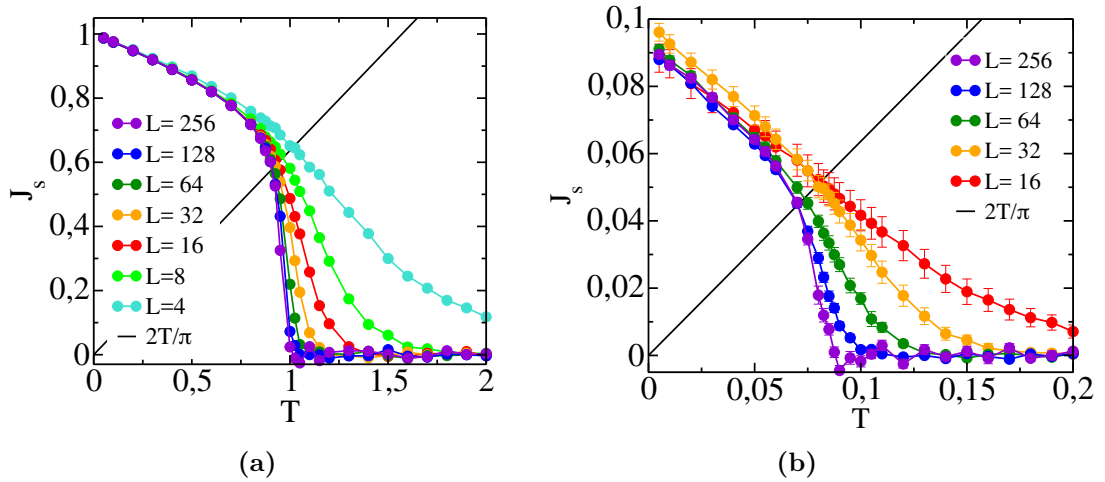

Figure 5.13. Temperature dependence of the superfluid stiffness J_s , its diamagnetic J_d and paramagnetic J_p component, and the vortex density ρ_V for the RTF case at $W/J = 10$ with a finite chemical-potential term, as in Eq.(5.5)

For the RTF case one finds instead a sensible dependence of the transition on the μ value, see Fig.5.13. By taking μ of the order of the transition temperature of the unbiased case we find a strong variation of both ρ_V and J_p already below T_c. This demonstrates the direct connection between the anomalous behavior of J_p and the unconventional vortex-nucleation mechanism in the fragmented SC background. While in the clean case or for uncorrelated disorder the vortex-like excitations are irrelevant for the low-temperature stiffness, for correlated disorder they are relevant also below the temperature scale where the universal jump would be expected. As we have already discussed, the crucial difference in the RTF case is the possibility to generate a low-temperature phase with a high density of bound vortex-antivortex pairs. An interesting open question is the identification of the possible signatures of this high-density vortex phase, besides the suppression of the superfluid stiffness that we investigated so far.

5.6   Universality class: study of the finite size scaling

Until now, we have seen that the presence of large enough regions of low couplings activates an anomalous nucleation of vortex-antivortex pairs even below T_c. It is then natural to ask whether the RTF correlated disorder could change the universality class of the XY model. To address this questions, it is needed to look at the finite-size scaling of the system in order to extrapolate the thermodynamic ($L \to \infty$) behavior of the system. Such study will reveal the critical point of the disordered model and its critical properties, starting from its critical temperature.

Figure 5.14. Superfluid stiffness temperature evolution for different linear sizes L. (a) Clean case. (b) Disordered RTF case, correspondent to $W/J = 10$.

Fig.5.14, shows Monte Carlo results for the temperature dependence of the stiffness both in the clean case and in the RTF disordered one (with a disorder level of W/J=10). The jump expected in the thermodynamic limit is in either case approached very slowly as a function of size. This can be related to the fact that the correlation length for $T > T_{BKT}$ does not diverge as a power-law, but according to

the exponential form:

$$\xi \sim e^{a/(T-T_{BKT})^{1/2}} \tag{5.6}$$

where, as discussed in the first chapter, a depends on the details of the model. From (5.6), since the finite size effect start to become important when $\xi \sim L$, we can derive the finite size shift of T_{BKT} as function of L:

$$T^*(L) - T_{BKT} \sim \frac{1}{2\ln L} \tag{5.7}$$

much slower than the conventional power-law shift.

From Fig.5.14, it is also clear that the superfluid stiffness below and above T_{BKT} scales differently with the linear size of the system L (Fig. 5.14). In[104] the two different regimes are studied separately and the two different scaling are derived. In this study we will first look at the low-temperature regime, where starting from the RG equations[2], already discussed in the first chapter, we will derive the scaling of the superfluid stiffness at the critical point. This first rescaling of the stiffness will give us information about both the critical point and the critical temperature of the system.

In the next step, we will consider the high-temperature regime and we will see how all the superfluid stiffness curves obtained in the previous passage, will collapse one on each other once having plotted them versus the proper scaling function. From this analysis we will gain more information about the exponential decay of the correlation length ξ.

5.6.1   Scaling from $T \to T_{BKT}^-$

The starting point of this study are the RG equation of the XY model close to the critical point Eq.(1.68) -(1.69):

$$\begin{cases} \frac{dx}{dl} = & -y^2 \\ \frac{dy}{dl} = & -xy \end{cases} \tag{5.8}$$

we approach the critical line $x^2 - y^2 = A^2$ from the superconducting (quasi-long-range-order) phase. Since we are looking at the limit: $A \to 0^+$ and $T \to T_{BKT}^-$, as we have already discuss in Chapter 1, we can rewrite Eq.(5.8) as:

$$\frac{dx}{dl} = -x^2 \tag{5.9}$$

whose solution is:

$$x = \frac{1}{l+c} \tag{5.10}$$

where c is a constant connected with the initial value of the RG flow l_0 and $x(l_0)$. Moreover $l = \ln(L)$ and $x = x(L, T = T_{BKT})$, being the finite size of the system (L) the upper boundary of the integration in dl and $dx(l)$. Since by definition: $x = K - 2 = \pi J_s/T - 2$, see Eq. (1.66) and (1.53), we can rewrite Eq.(5.10) as:

$$J_s(L, T_{BKT}) \frac{\pi}{2T_{BKT}} = 1 + \frac{1}{2\ln(L) + c} = 1 + \frac{1}{2\ln(L/L_0)} \tag{5.11}$$

Finally, by means of the universal relation[32] between $J_s(T_{BKT})$ and T_{BKT} (Eq. (1.60)) we end with:

$$J_s(\infty, T_{BKT}) = \frac{J_s(L, T_{BKT})}{\left(1 + (2\ln(L/L_0))^{-1}\right)} \tag{5.12}$$

Rescaling the superfluid stiffness with Eq.(5.12), all the curves corresponding to different linear sizes L, will assume the same value at criticality. As a consequence, the crossing point of all the superfluid-stiffness curves can be used to determine the critical temperature of the transition in the limit of infinite size.

With this purpose, from the superfluid-stiffness numerical data, we have looked for that value of the parameter L_0 giving the best crossing point at finite temperature and afterwards we have estimated the critical temperature of the system.
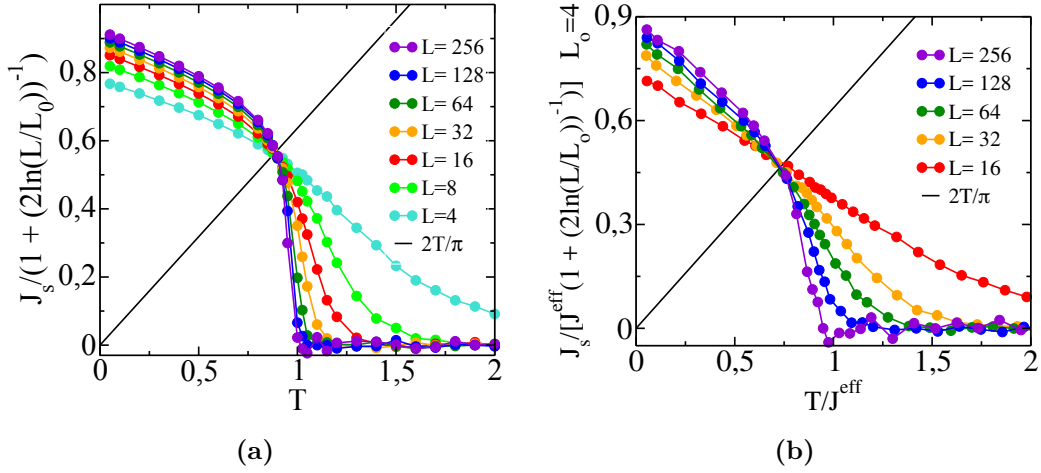
Figure 5.15. Rescaling of the superfluid stiffness curves by means of Eq. (5.12) both for the clean case (a) and for the RTF disordered case with $W/J = 10$ (b). In the presence of disorder, for a better comparison with the clean case, one can rescale both the superfluid stiffness and the temperature by $J_{eff} = J_s(T = 0)$.

When applied to the clean case, this procedure gives $L_0 = 1.4$ from which we can extrapolate $T_{BKT} \simeq 0.89$ (see Fig.5.15a) in good agreement with[105]. For the disordered case, the best crossing point is instead obtained for $L_0 = 4$ and from Fig.5.15b, we can firstly observe that the presence of correlated disorder does not change the universality class of the XY model, being the crossing point still on the critical line $K = 2$. However, despite having rescaled both the superfluid stiffness and the temperature with respect to $J_s(T = 0) \equiv J_{eff}$ (for the clean case: $J_{eff} = 1$), the RTF disorder does change the critical temperature of the rescaled model to a lower value:

$$T_{BKT}^{RTF} \simeq 0.71 \, J_{eff} \tag{5.13}$$

Quite interesting, this result can be physically interpreted in terms of a decrease of the effective vortex-core energy μ, due to the presence of spatially correlated disorder. Indeed a small μ implies a larger renormalization of J_s before the transition, and

as a consequence a smaller value of the critical temperature. Another remarkable effect of the presence of spatially correlated disorder is the magnification of the finite size effects with respect to the homogeneous case. For instance, the curve of the clean case in 5.15a relative to $L = 8$ shows a tail similar for extension to the one correspondent to $L = 64$ of the disordered case see 5.15b, hence eight times bigger than the homogeneous case.

5.6.2 Scaling from $T > T_{BKT}$

In the high-temperature regime the thermodynamic limit of the superfluid stiffness is obviously zero. The finite size effects in this region are essentially due to the correlation length ξ, whose divergence for $T \to T_{BKT}^+$ is cut off by the system size L, see Eq. (5.6). By means of the finite-size scaling hypothesis[106, 107], we can write the rescaled superfluid stiffness as a function of the ratio betwenn L and ξ:

$$\frac{J_s(L,T)}{\left(1 + (2\ln(L/L_0))^{-1}\right)} = F(L/\xi) \tag{5.14}$$

Taking thus the logarithm of the argument of the scaling function $F(x)$, Eq.(5.14) can be written in terms of another function $g(\ln(L/\xi))$, so that:

$$\frac{J_s(L,T)}{\left(1 + (2\ln(L/L_0))^{-1}\right)} = g(\ln(L/\xi)) = g(\ln L - a/(T - T_{BKT})^{1/2}) \tag{5.15}$$

Hence, the rescaled superfluid stiffness will have the same functional dependence on $\ln L - a/(T - T_{BKT})^{1/2}$ for each value of the system size considered.
The collapsed curves of the rescaled stiffness, obtained from our numerical data, are shown in Fig.5.16, where we have obviously used $T_{BKT} = 0.89$ for the clean case and the previously-derived critical temperature $T_{BKT}^{RTF} = 0.71 J_{eff}$ for the RTF disordered case. The parameter to be fixed in this study is a of Eq.(5.6), choosen in such way to obtain the best collapse of all the curves. For the clean case it is known[107] to be $a = 1.5$, while in the presence of correlated disorder we have obtained the best collapse for: $a = 2.0$. The increase of the parameter a, by means of the presence of corraleted disorder, reflects in the scale of the x-axis, much smaller in the RTF case Fig.5.16b with respect to the homogeneous one Fig.5.16a. This physically means that the correlations length ξ diverges faster in the presence of correlated disorder than without it, in agreement with the previously observed increase of the finite size effects (Fig.5.15). Let us also highlight that from the limit $T \to T_{BKT}^+$ in Fig.5.16, which in terms of the function $g(L/\xi)$ corresponds to $\ln L - a/(T - T_{BKT})^{1/2} \to -\infty$, we can extrapolate the value of the superfluid stiffness expected at the critical point. Both for the clean and the disordered case it confirms the Nelson-Kosterlitz relation:

$$J_s(\infty, T_{BKT}) = \frac{2}{\pi} T_{BKT} \simeq 0.6 \tag{5.16}$$

$$\frac{J_s(\infty, T_{BKT}^{RTF})}{J_{eff}} = \frac{2}{\pi} \frac{T_{BKT}^{RTF}}{J_{eff}} \simeq 0.45 \tag{5.17}$$

as expected since either the two critical points are crossed by the universal line $K = 2$.

Hence, this study confirms that in both the cases the universality class is the BKT one, showing at the same time that also in the presence of correlated disorder the correlation length diverges exponentially in the reduced critical temperature. Finally, it sheds light on the two main differences, with respect to the clean case, introduced by the spatially correlated disorder: the reduction of the critical temperature T_{BKT} and the faster increase of the correlation length ξ as $T \to T_{BKT}^+$.
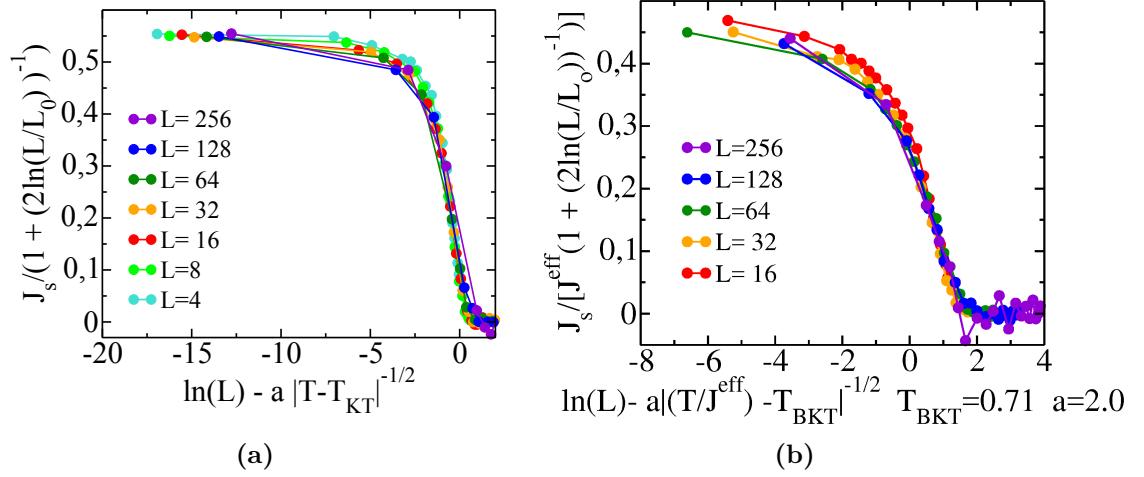


Figure 5.16. Superfluid stiffness curves of different linear size L, renormalized and collapsed on the same universal curve relative to the high-temperature regime: $T > T_{BKT}$. Clean case (a) and RTF disordered case with $W/J = 10$ (b).

Chapter 6

2D XY model with a finite magnetic flux

The application of a transverse magnetic field on the two-dimensional XY model, is one of the most interesting extension of the BKT transition. Its effect is to induce within the system a finite number of vortices with a given vorticity, forming at very low temperature an ordered vortex lattice. As the temperature is increased, the system develops also bound pairs of vortex-antivortex, as topological excitations. In this context, the mechanism driving the loss of the spin rigidity can be either the usual BKT unbinding mechanism of vortex-antivortex pairs or the melting of the low-temperature vortex lattice.
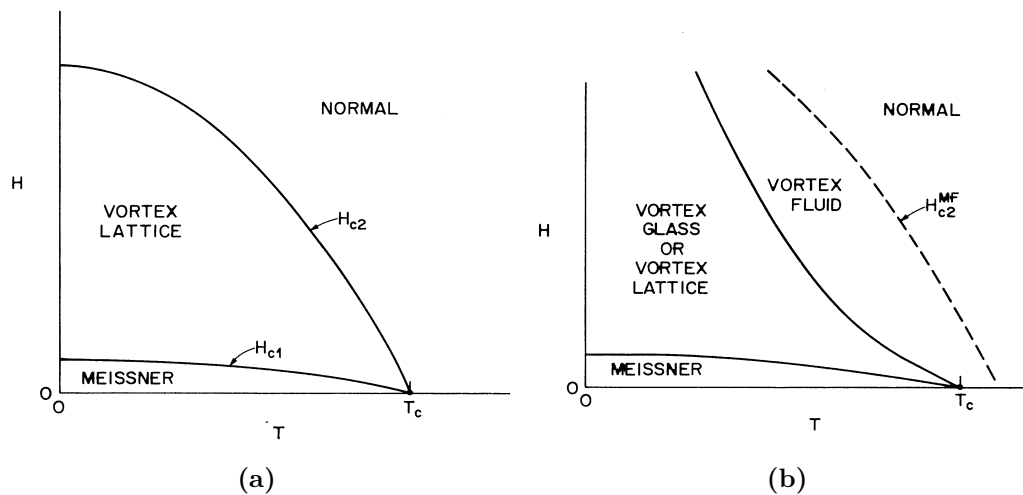
Figure 6.1. [108] (a) Mean-field schematic phase diagram of a type-II superconductor as a function of applied magnetic field H and temperature T. (b) Schematic phase diagram of a three-dimensional type-II superconductor with strong thermal fluctuations. The crossover from the normal regime to the vortex-fluid regime, in which vortices have a finite mobility, is not a sharp phase transition.
Finally, the vortex-lattice phase is replaced with a vortex-glass phase in the presence of disorder.

The physical picture just described, is nothing but the statistical mechanics description of the two-dimensional Abrikosov lattice of vortices occurring in type-II superconductors. Indeed, as demonstrated by Abrikosov in his seminal paper[109], for this class of superconductors, when the applied magnetic field reaches a critical value (usually referred as H_{c1}) from below, the magnetic field begins to penetrate in a quantised form of unity $\Phi_0 = hc/2e$ and a lattice of flux lines (or vortices) takes the place of the Meissner state (see Fig.6.1a). This scenario, schematically shown in Fig.6.1a[1], changes slightly in the presence of strong thermal fluctuations and disorder. Indeed, strong thermal fluctuations increasing the vortex mobility can turn the vortex lattice into a vortex fluid, while the presence of disorder can modify the ordered vortex lattice into a vortex glass as shown in Fig.6.1b.

This topic has found recent experimental application also to thin films[37, 38]-[39], layered high-T_c superconductors[40] and even in cold atomic systems, where the magnetic field is mimicked by imposing a rotation on the condensate[41]-[42]. Nevertheless, despite the strong interest and effort devoted to the issue, it is still mostly unclear how the presence of a transverse magnetic field affect the BKT transition. The problem has been addressed theoretically in many ways: by means of the Coulomb-gas mapping[43], in which the presence of a transverse magnetic field translates simply in an excess of positive (or negative) charges; via a field theoretical approach based on the sine-Gordon model[44] and also by the use of both Quantum[45] and classical[46]-[47] Monte Carlo simulations. The presence of intrinsic disorder within the system renders the problem even more intriguing, indeed it has been recently observed[38] that disorder can act as pinning potential for vortices leading to a modification of the ordered vortices lattice and at the same time reducing the vortex fluctuations responsible for the fast depletion of the superfluid stiffness[48].

In this chapter, I will address the issue of the interplay between disorder and transverse magnetic field applied to the classical two-dimensional XY model by means of Monte Carlo simulations. This chapter is organised as follows: in the first section I will briefly review two very recent experimental results on disordered thin SC films in the presence of a finite transverse magnetic field. In Section II, I will discuss the MC numerical results obtained on the homogeneous 2D XY model with finite flux. In Section III, I will study the interplay between magnetic field and disorder. I will show that the magnetic field increases the inhomogeneity of the system, modifying at the same time the ordered vortex lattice of the ground state. Moreover, studying the superfluid stiffness transition in temperature, I will show that the presence of disorder makes the (disordered) vortex lattice stronger against thermal fluctuations with respect the homogenous case. Indeed, while in the clean case vortices can easily move via thermal fluctuations, the presence of the disorder can act as a vortex pinning potential, reducing their thermal mobility.

---

[1]The phase diagrams shown here have been used for the description of three-dimensional superconductors in[108]. However, for the 2D case the picture is almost still the same, the dimensionality modifies the nature of the transitions between the SC and the normal state, as we will discuss later.

## 6.1   SC films: Magnetic field and inhomogeneity

In the previous chapters we have seen how in the presence of strong disorder, the superconducting state of thin films become fragmented, forming insulating domains and SC islands, both made of Cooper pairs. In this scenario, the superconducting transition is driven by the achievement of a global phase coherence within the system and it is conversely destroyed through phase fluctuations between different SC islands, which, leaving finite the pairing amplitude, give rise to the experimentally observed pseudo-gap state.

Very recently[38], it has been shown that applying a magnetic field on a weakly disordered thin SC film, the proliferation of vortices as well induces a fragmentation of the superconducting state into domains, leading to a pseudo-gap state that progressively widens as the magnetic field is increased.
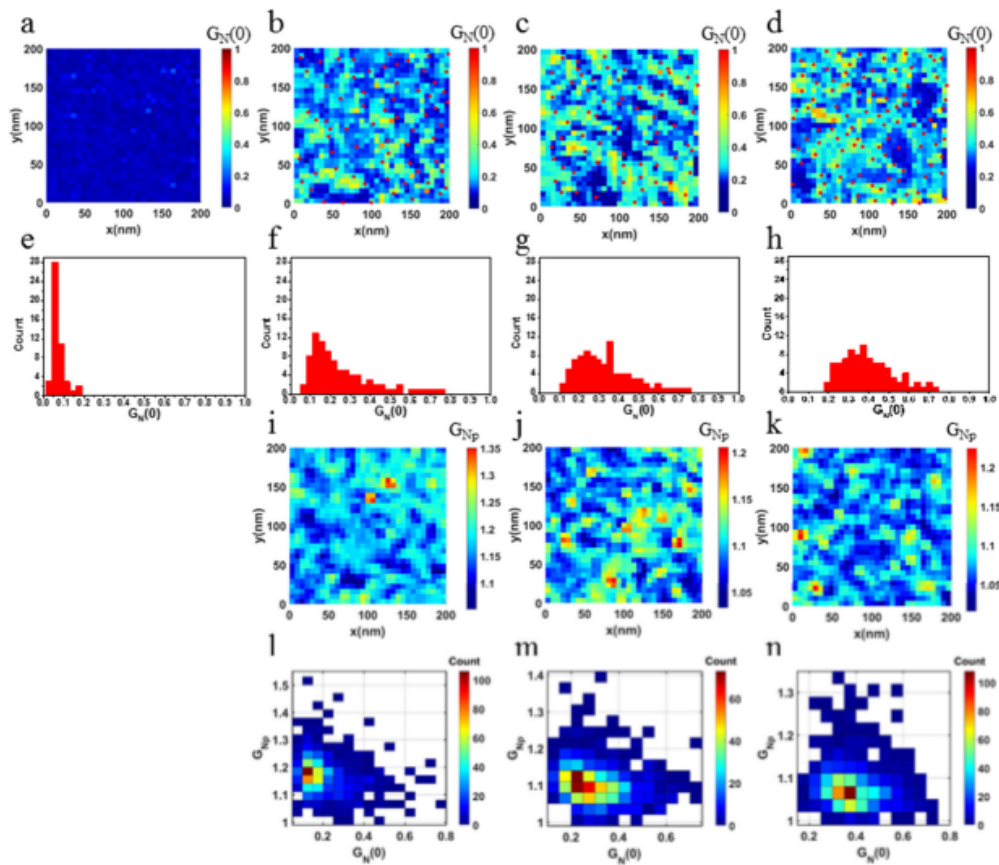
Figure 6.2. [38](a)-(d) Zero bias conductance ($G_N(0)$) maps for fields $0, 40, 60$ and $75\,kOe$ respectively over the same $200\,nm \times 200\,nm$ area at $450\,mK$, obtained from area spectroscopy over 32×32 pixels grid. The red dots show the position of the vortices. (e)-(h) Distribution of $G_N(0)$ for $0, 40, 60$ and $75\,kOe$ respectively. With increasing field the distributions develop large tails, signifying emerging inhomogeneity with field. (i)-(k) Coherence peak height (G_{N_p}) maps for $40, 60$ and $75\,kOe$. (l)-(n) Cross-correlation histograms between $G_N(0)$ and G_{N_p} for corresponding fields, showing inverse correlation between the two quantities.

As we have seen in Chapter 3, the formation of a fragmented SC state is evidenced in STS by the variation of the peak height, i.e. G_{N_P}, that is a measure of the local SC order parameter. On the other hand, experimentally[84] also the zero-bias conductance becomes inhomogeneous at strong disorder. Based on these observations, in Ref.[38] the formation of an inhomogeneous SC state has been investigated via tunnelling conductance spectroscopy on a weakly disordered NbN films. In Fig.6.2, are shown the conductance maps in real space both at zero bias $G_N(0)$ (Fig.6.2(a)-(d)), corresponding to the centre of the gap, and the conductance maps measured in correspondence of the peak around the gap (Fig.6.2(i)-(k)), i.e. $G_{N_P} = G_N(V = 2.2\,mV)$ (see also Fig.6.3). With the increase of the magnetic field, both the maps become more and more inhomogeneous in space; at the same time, as shown in Fig.6.2(e)-(h), the probability distribution of the zero bias conductance (ZBC) becomes broader, developing a large tail.
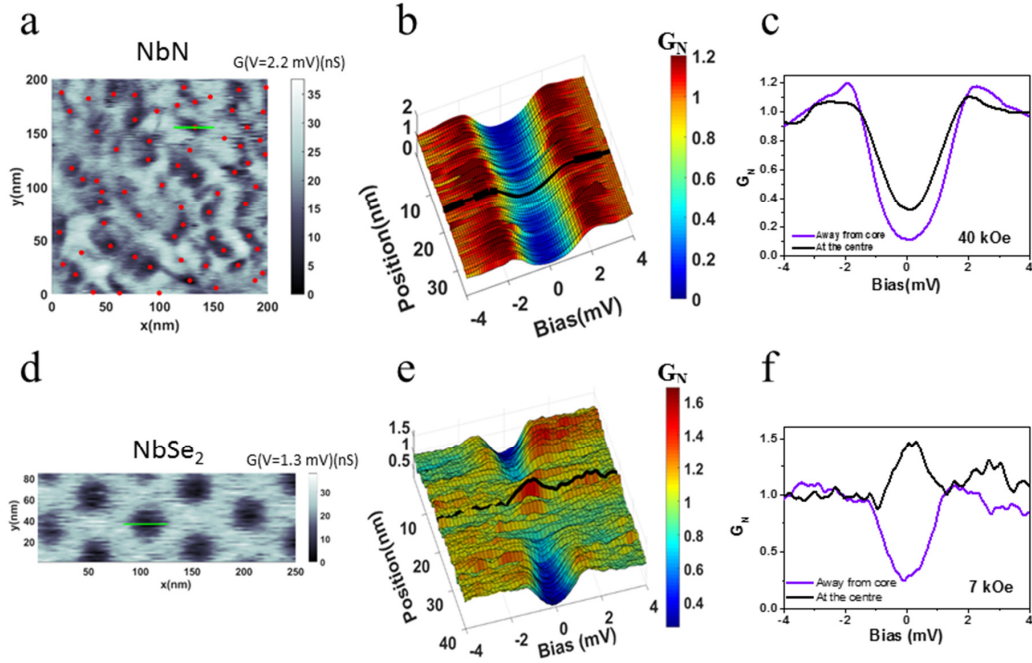

Figure 6.3. [38]Comparison of vortex core in $NbSe_2$ and NbN. (a) Conductance map over $200\,nm \times 200\,nm$ area of NbN at $40\,kOe$ at fixed bias voltage ($G(V = 2.2mV)$). The vortices are shown as red dots. (b) Normalized tunneling spectra ($G_N(V)$-V) along the green line on conductance map in (a) going through the center of one vortex core; the dark black line corresponds to the spectrum at the vortex core. (c) Representative spectra for NbN at the center of the vortex core (black) and a point away from the core (violet). (d) Conductance map over $250\,nm \times 85\,nm$ area of pure $NbSe_2$ at $7\,kOe$ at fixed bias voltage ($G(V = 1.3mV)$). The dark regions are the vortices with lower values of conductance forming a hexagonal Abrikosov lattice. (e) Tunneling spectra ($G_N(V)$-V) along the green line on conductance map in (d) going through one vortex core of $NbSe_2$; dark black line corresponds to the spectrum at the vortex core. (f) Representative spectra for $NbSe_2$ at the center of the vortex core (black) and a point away from the core (violet)

From the two conductance maps of $G_N(V = 0)$ and G_{N_P}, it is also possible to identify the core of the vortices proliferating within the system, indicated as red dots in Fig.6.2(a)-(d) and Fig.6.3(a). In the presence of disorder, the observed vortices do not form an ordered Abrikosov lattice, as observed in clean system (Fig.6.3(d)): the vortex crystal observed in $NbSe_2$, becomes a disordered vortex glass, as we have seen schematically in Fig.6.1b. Nevertheless, from Fig.6.3(a), we can get a deeper understanding, that will be better investigated in the following, on the mechanism behind such lattice deformation: it is indeed quite evident form 6.3(a) the strong correlation between the position of the red spots and the darker regions, corresponding to lower height of the coherence peaks (i.e. lower local superfluid stiffness). The presence of such inhomogeneity induces vortices to move towards those regions in space where the SC phase twist is energetically less expansive, thus towards darker regions of lower local superfluid rigidity. Finally, it is also worth to highlight that, for disordered NbN films, the representative spectra at the centre of the vortex core looks very different respect to the case of the clean single crystal of $NbSe_2$ (Fig.6.3(c) and 6.3(f)). Indeed, in the former case the normalised tunnelling spectrum shows the presence of the pseudo gap state, characterised by a suppression of the coherence peak and a soft gap characteristic of superconducting pairing.

In the same work[38], the experimental results have been also compared with numerical simulations performed on the two-dimensional attractive Hubbard model in the presence of a transverse field. Although they found a good agreement between experimental and numerical results, solving numerically fermionic models (via the usual BdG technique) requires a very big computational effort, which limits in a significant way the accessible size of the system studied. In particular in[38], they access to a maximum area of only 36×36 lattice size with also a very small number of vortices. Nevertheless, as we have just discussed, being the transition driven by phase fluctuations which lead the system from a SC state to a pseudo gap one, one can also address the same issue by means of a bosonic model, in which the fermionic degrees of freedom are assumed to be frozen.

In the following sections, by means of Monte Carlo simulations on the classical XY model, we will indeed recover the main experimental results presented in[38], reaching much larger system size and also higher values of the magnetic field applied. In particular, we will study the Abrikosov lattice of vortices with and without disorder, we will recover the enhancement of the inhomogeneity by the increase of the applied field and we will also investigate the thermodynamic transition of the system measuring the superfluid-stiffness temperature dependence for different value of the magnetic field. Unlucky, superfluid-stiffness measurements on SC films, with an applied magnetic field, are very few. One of these rare experimental results can be found in[48]. In this work by Misra et al., strongly disordered SC films of $Mo_{43}Ge_{57}$ and InO_x have been investigated via low frequency ac conductivity, for different values of the applied transverse magnetic field. The superfluid stiffness is there obtained via the sheet impedance $Z(\omega) = R(\omega) + i\omega L(\omega)$, whose real part is the ac resistance, while $L(\omega)$ is the ac inductance of the sample. Indeed, the inverse inductance L^{-1} (shown in Fig.6.4) is proportional to the superfluid density n_s and constitutes a direct measure of the phase stiffness of the system. From Fig.6.4, we can see that the critical temperature at which the system loses its superfluid response decrease with the increase of the applied field.
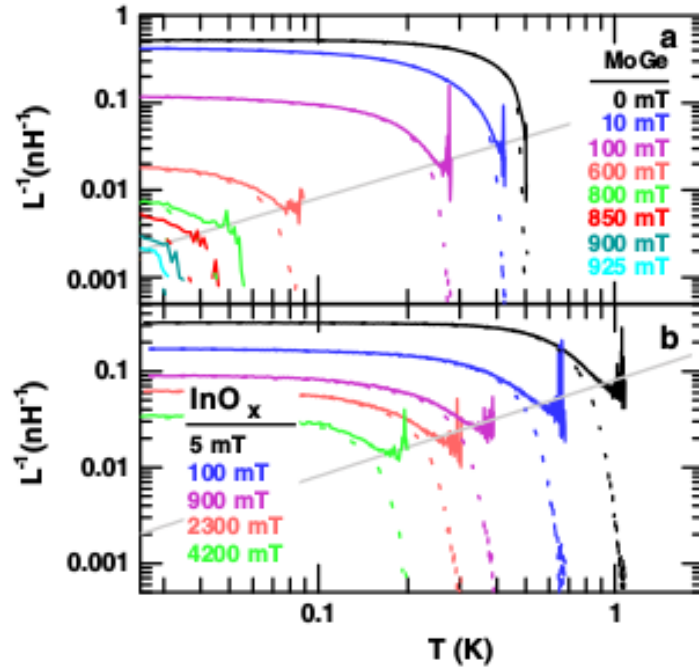
Figure 6.4. [48] Temperature dependence of the inverse conductance $L^{-1}(\omega)$ taken at
$20\,kHz$ for different values of the applied magnetic field. In[48], they used two different
ways to measure the superfluid density, identified respectively with a continuous and
with a dashed line, we refer to the original paper for details. The two panels correspond
to the two samples investigated: (a) $MoGe$ and (b) InO_x thin films. While the grey
line corresponds to the BKT critical line.

Even though such downturn to zero of the stiffness seems to occur in proximity of
the BKT critical line, indicated with a grey line in Fig.6.4, this result is a misleading
effect of the use of the log scale for L^{-1} in Fig.6.4. As we shell see below, the thermal
transition at finite magnetic field is rather different from the case $H = 0$. Our results
are consistent with new unpublished data from the group of Prof. Raychaudhuri,
that we will discuss at the end of the Chapter.

6.2   XY model with $B\hat{z}$: clean case

Motivated by these intriguing results[38, 48], we have faced the issue by means of MC
simulations on the two-dimensional XY model, studying the effects of a transverse
magnetic field on the classical phase fluctuations.
The model has been simulated on a square lattice with periodic boundary conditions
for a maximum size of $L = 64$, new simulations on $L = 128$ are now ongoing. The
algorithms used here are the same presented in the fourth chapter: the standard
Metropolis algorithm combined with the Over-relxation one and the Simulated-
Annealing procedure to help the system thermalisation at lower temperature. For
each run we have made 50000-75000 MC steps, measuring the main observables
with a frequency of 5 steps, after having discarded the firsts 25000. Finally in the

presence of a finite transverse magnetic field, even for the clean case, the averages
have been computed over 5 independent runs.

In the presence of a transverse magnetic field $H\hat{z} = \vec{\nabla} \times \vec{A}$, the XY Hamiltonian
(1.1) modifies. The coupling with the field is introduced by the minimal-coupling
prescription for the vector potential $\vec{A}$, which makes *gauge invariant* the phase angle
difference:

$$H_{XY} = -J \sum_{\mu,i} \cos(\theta_i - \theta_{i+\mu} + F_i^{\mu}) \tag{6.1}$$

where:

$$F_i^{\mu} = \frac{2\pi}{\Phi_0} \int_{r_i}^{r_{i+\mu}} A_i^{\mu} \cdot d\mu \tag{6.2}$$

is proportional to the line integral of the vector potential $\vec{A}$ along the bond connecting
two neighbors spins i and $i + \mu$, and $\Phi_0 = hc/2e$ is the quantum flux.

The sum of F_i^{μ} going counterclockwise around any closed path C of bonds on the
lattice is 2π times the number of magnetic flux quanta f_C penetrating the path:

$$\sum_C F_i^{\mu} = \frac{2\pi}{\Phi_0} \oint_C \vec{A} \cdot \vec{dl} = 2\pi \frac{\Phi_C}{\Phi_0} = 2\pi f_C \tag{6.3}$$

Since in the following we will always consider H to be uniform in space, we will refer
to the intensity of the applied field in terms of the flux quanta f penetrating trough
an unitary plaquette P:

$$f = \frac{Ha^2}{\Phi_0} \tag{6.4}$$

being:

$$2\pi f = \frac{2\pi}{\Phi_0} \oint_C \vec{A} \cdot \vec{dl} = \frac{2\pi}{\Phi_0} \oint_C \vec{\nabla} \times \vec{H} \cdot \vec{dl} = \frac{2\pi}{\Phi_0} Ha^2 \tag{6.5}$$

In literature[46]-[47], one usually refers to this case as the *uniformly frustrated* XY
model with frustration f. Indeed, the phase shift F_i^{μ} in the cosine argument of (6.1)
adds *frustration* to the system by rendering the ground state no longer ferromagnetic:
at $T = 0$, the phases θ_i's instead to be all equal, will vary from site to site trying to
minimise the new gauge-invariant phase $(\theta_i - \theta_{i+\mu} + F_i^{\mu})$. Consequently, the value
of f will correspond to the level of such frustration, determining the inhomogeneous
space structure of the ground state itself. Specifically, the ground state of the
uniformly frustrated XY model will consist of a periodic configuration of vortices in
the phase angle θ_i, whose number is directly proportional to f, as we will see in the
next paragraph. A good gauge choice for the vector potential $\vec{A}$ is the London gauge:
$\vec{\nabla} \cdot \vec{A} = 0$. For simplicity, let us choice for the following numerical simulations:

$$\vec{A} = B(0, x) \tag{6.6}$$

So that:

$$F_i^{\mu} = \begin{cases} 0 & \text{if } \mu = x \\ 2\pi f x_i & \text{if } \mu = y \end{cases} \tag{6.7}$$

Finally, since in our MC simulations we will use periodic boundary conditions, it is important to highlight that with this choice not all the values of f will be allowed. Indeed, periodic boundary conditions, together with the Landau gauge $A_y = 2\pi f x$, give rise to the constraint:

$$L_x \cdot f = 1, 2, 3, \ldots \tag{6.8}$$

Hence, for a given value of L_x the smallest frustration we can introduce within the system is: $f = 1/L_x$.

In conclusion, since our aim is to use the uniformly frustrated XY model to get a deeper understanding of the experimental results[38, 48] made on thin SC films, let us give here the conversion between the frustration value f and the equivalent magnetic field applied to real system in unit of Tesla. By substituting in (6.4) the lattice constant a with the SC coherence length ξ:

$$f = \frac{Ha^2}{\Phi_0} \simeq \frac{H\xi^2}{\Phi_0} = \frac{H(T)\,\xi^2}{2.07 \cdot 10^{-11} T \cdot cm^2} = 0.05 H[T] \tag{6.9}$$

where we used for the coherence length $\xi_0 \sim 10\,nm$, thus an applied magnetic field of $4T$ correspond to a typical value of $f \simeq 0.2$.

6.2.1　Abrikosov lattice of vortices

As already mentioned, the presence of a transverse magnetic field induces within the system a finite number of vortices (with the same vorticity) that, unlike the thermal ones, do not disappear in the low-temperature regime, forming on the contrary a periodic lattice, so to minimise their mutual interaction energy.

The number of vortices of the ground state, can be easily derived by rewriting the charge neutrality condition in terms of the new gauge invariant phase. Indeed, while in the absence of magnetic field the neutrality condition reads:

$$\sum_j \oint_{P_j} \vec{\nabla}\theta_i = 2\pi \sum_i n_i = 0 \quad \text{if } H = 0 \tag{6.10}$$

in the presence of a finite field $H \neq 0$, the same condition needs to be rewritten by means of the minimal substitution $\vec{\nabla}\theta_i \to \vec{\nabla}\theta_i - \vec{A}_i$, so that:

$$\sum_j \oint_{P_j} (\vec{\nabla}\theta_i - \vec{A}_i) = 2\pi \sum_i (n_i - f) = 2\pi \sum_i q_i = 0 \quad \text{if } H \neq 0 \tag{6.11}$$

From the last passage of (6.11), it is important to highlight the distinction between the gauge invariant charge q_i, fulfilling the neutrality condition, and the integer vorticity n_i, connected to the non gauge-invariant phase angle θ_i. Hence, from Eq.(6.11) it follows that the number of extra vortices, induced by the magnetic field, in the phase angles θ_i's is:

$$N_v = fL^2 \tag{6.12}$$

where L is the linear size of the system. Obviously, at finite temperature, also the vorticity of thermal vortices will contribute to the sum $\sum_i n_i$ of (6.11). However,

since the topological excitations nucleated by the system are always originated from a bound vortex-antivortex pair, they will always contribute to the (6.11) with an even number of $+$ and $-$ vortices, canceling out within the sum.

In Fig.6.5, we report the vortex lattice for different values of f, obtained by means of Monte Carlo simulations, measuring the local vortex density at the lowest temperature considered: $T = 0.005$.

Because of the periodicity of the cosine in (6.1), taking $f \to f + 1$ will leave the Hamiltonian invariant. It is thus sufficient to consider f just in the range of 0 and $1/2$ to explore all the possible frustration for a given size. Negative value of f, indeed, will lead to the same amount of frustration, just generating vortices with opposite vorticity with respect to their positive counterpart.

The most studied case of uniform frustration is $f = 1/2$ [46]-[110], also known as the *Fully frustrated* XY model (FFXY). Indeed, this choice is equivalent of having a classic XY model with antiferromagnetic vertical bonds (for odd values of x_i) alternated with ferromagnetic vertical bonds (for even values of x_i). In this particular case, the ground state is such that the gauge-invariant phase angle difference across all bonds is $\pi/4$, and consequently the vortex lattice assumes a checkerboard ordered pattern as shown in 6.5(f). The geometry of the vortex lattice, as well as its symmetries, plays a key role in determining the nature of the phase transitions occurring within the system. Indeed, the ground state, choosing one among the different possibilities to build the same vortex lattice, spontaneously breaks the symmetry of the Hamiltonian (6.1). This spontaneous symmetry breaking will then reflect in the nature of the melting transition of the vortex lattice, which is added to the BKT transition occurring in absence of a transverse field. We will come again on this point in the following paragraph. Let us now highlight an other aspect to keep in mind in the analysis of MC results: the presence of a discrete lattice with a given geometry. Indeed, in thin SC films, or in general in a continuum model, vortices can *freely* organise themselves within the space forming a triangular Abrikosov lattice. On the other hand, for the case of numerical simulations, mimicking a periodic arrays of Josephson-junctions, the discrete lattice forces the vortices to lie at pinning sites, acting thus as a periodic potential that cannot be viewed as a weak perturbation on an uniform film. This topic has been largely studied in [111]-[112], for square, triangular and even honeycomb lattices. In particular, it has been shown that depending on the lattice geometry there are values of the frustration f, for which the ground-state energy is lower, having formed a *better* Abrikosov lattice. However, since our main interest concerns disordered system, the effect of the lattice pinning potential is in that case mostly overcome by the pinning due to the disorder itself. Indeed, as we will see in the next sections, vortices will modify their ordered configuration, favouring sites with lower local stiffness. Nevertheless a fingerprint of such effect can be observed in the superfluid-stiffness phase transition of the clean case, that we are going to present.

6.2.2 Superconducting transition

The critical behavior of the uniformly frustrated XY model changes dramatically with the value of f. For $f = 0$, as we have largely discussed, the system shows the usual BKT transition driven by the unbinding of bound vortex-antivortex pairs. In
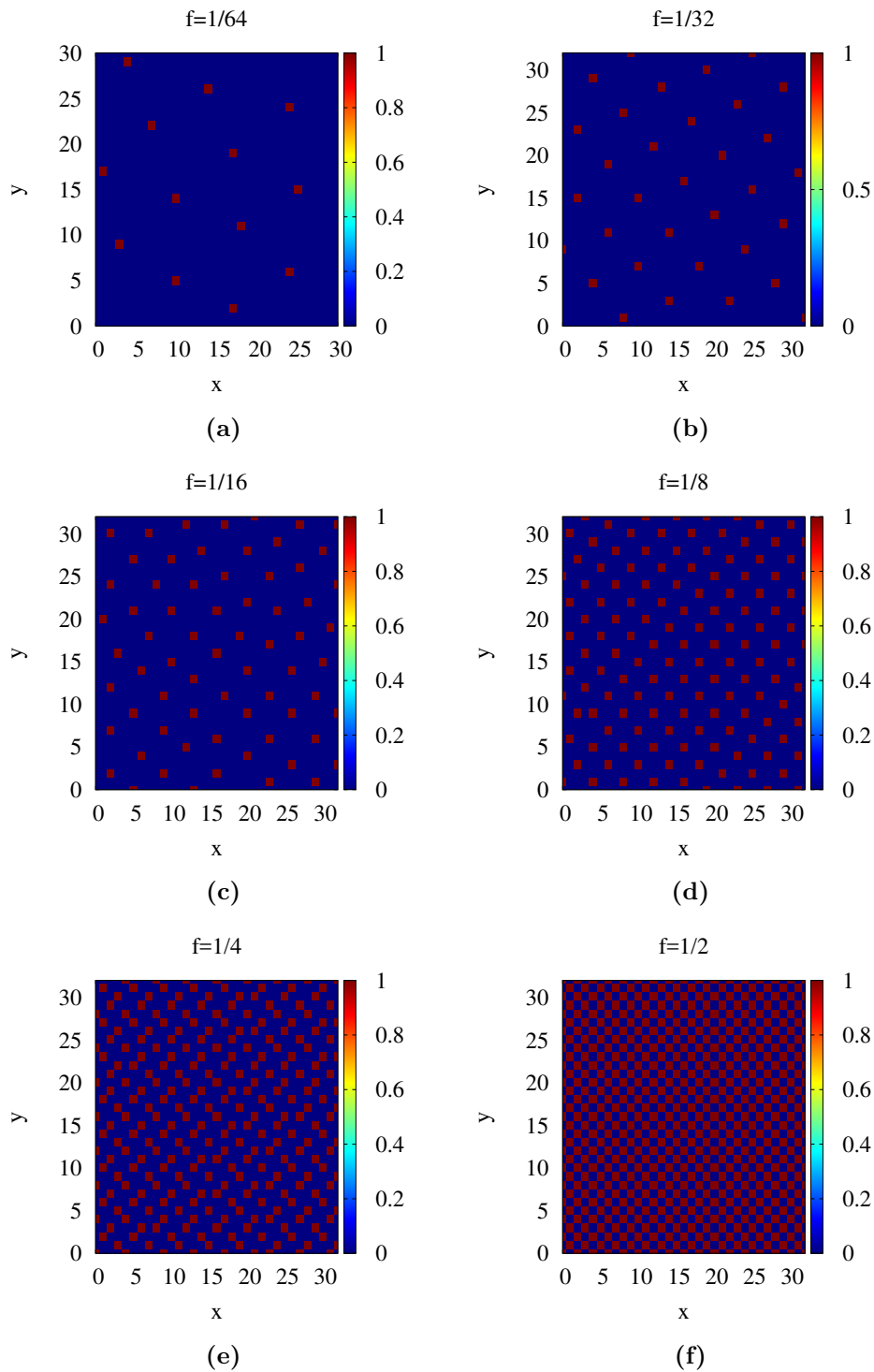
Figure 6.5. Vortex Lattice for different values of the filling fraction f. The color map stays for the density of vortices measured at the lowest temperature reached by the simulated annealing procedure (here $T = 0.005$).

the case of maximal frustration, $f = 1/2$, as shown by Olsson in[113], the system undergoes two very close continuous phase transitions: the BKT transition, followed by the Ising transition at higher temperature, with ordinary Ising exponents. Indeed, the particular space structure of the ground state in the FFXY model, leads to the breaking of a discrete two-fold symmetry Z_2, which reflects in the observed Ising transition.

Apart from these two cases, however, the critical behavior for other values of f is more complex and, despite the effort of the last two decades [114]-[47], less understood. The phase transitions occurring within the system at finite, but not maximal, f can be several and their nature is still unclear in most of the cases.

Nevertheless, without pretending to understand the nature of the transitions observed, being it beyond the aim of our work, we have studied the superfluid stiffness trend in temperature by means of Monte Carlo simulations for different values of the frustration. Starting from the superfluid stiffness J_s definition in Eq. (4.2), let us write its expression for the uniformly frustrated XY model:

$$
\begin{aligned}
J_s^\mu = \frac{J}{L^2}\langle \sum_i \cos(\theta(\mathbf{r}_i) - \theta(\mathbf{r}_i + \hat{\mu}) + F_i^\mu)\rangle + \\
- \frac{J\beta}{L^2}\langle [\sum_i \sin(\theta(\mathbf{r}_i) - \theta(\mathbf{r}_i + \hat{\mu}) + F_i^\mu)]^2\rangle + \\
+ \frac{J\beta}{L^2}\langle \sum_i \sin(\theta(\mathbf{r}_i) - \theta(\mathbf{r}_i + \hat{\mu}) + F_i^\mu)\rangle^2
\end{aligned}
\tag{6.13}
$$

Hence, respect to case $f = 0$ of Eq. (4.3)-(4.5), we have now an additional term to the paramagnetic function J_p. Indeed, in the presence of a finite magnetic field it is needed to consider the *connected* current-current correlation function, since the presence of H induces within the system finite super currents, making non vanishing the term $\propto \langle \sum_i \sin(\theta(\mathbf{r}_i) - \theta(\mathbf{r}_i + \hat{\mu}) + F_i^\mu)\rangle^2$.

The numerical results of J_s for different values of f are shown in Fig.6.6 and 6.7.

We can immediately notice that the critical temperature T_c at which the paramagnetic phase ends is strongly suppressed for smaller values of f, completely at odd with the experimental results shown before in Fig.6.4. The general trend seems, indeed, to be a proportionality between T_c and f: lower critical temperatures for smaller frustration.

The observed trend has been already carefully proved in[47], where Alba et al. have shown that in the limit of small frustration $f = 1/n$ (and $n \gg 1$), the critical temperature T_c decreases with the increase of n: $T_c \sim 1/n \to 0$ as $n \to \infty$.

This apparently counterintuitive result, far from any idea of adiabaticity, can be easily understood in terms of correlation length ξ. Indeed, by a simple dimensional argument one can show that for sufficiently small f and any $T < T_{BKT}$, the correlation length is finite and thus the system is paramagnetic. Let us imagine to renormalize the system introducing a new lattice spacing twice the older one $a' = 2a$, the new screening length in lattice unit will be then $\xi' = \xi/2$, analogously we obtain $f' = 4f$ for the frustration parameter. Hence, it follows that $\xi' f'^{1/2} = \xi f^{1/2}$, meaning that this quantity stays constant under real-space renormalization-group transformation.

Finally since for small f, one is closed to the XY line of fixed points for which

is expected $T' \simeq T$ [47], the condition $\xi f^{1/2} = c$ holds, approximately, at fixed temperature so that in the limit $f \to 0$: $\xi \sim f^{-1/2}$.

In other words, in the limit of very small magnetic field, the few vortices present at low temperature have much more freedom to move within the system, respect to the case of a higher vortex density. In the latter case, indeed, the presence of a stronger mutual interaction would create a vortex lattice more *robust* under thermal fluctuations. The superconducting to insulator transition is in any case driven by the melting of the vortex lattice and not anymore by the unbinding of vortex-antivortex pairs as in the BKT physics.

However, in order to reproduce the dependence between T_c and f observed in[48], we have to consider something else responsible for the vortices strong pinning at low f. In the following, we will see that the presence of disorder plays a key role in this sense, restoring the dependece between T_c and f experimentally observed.
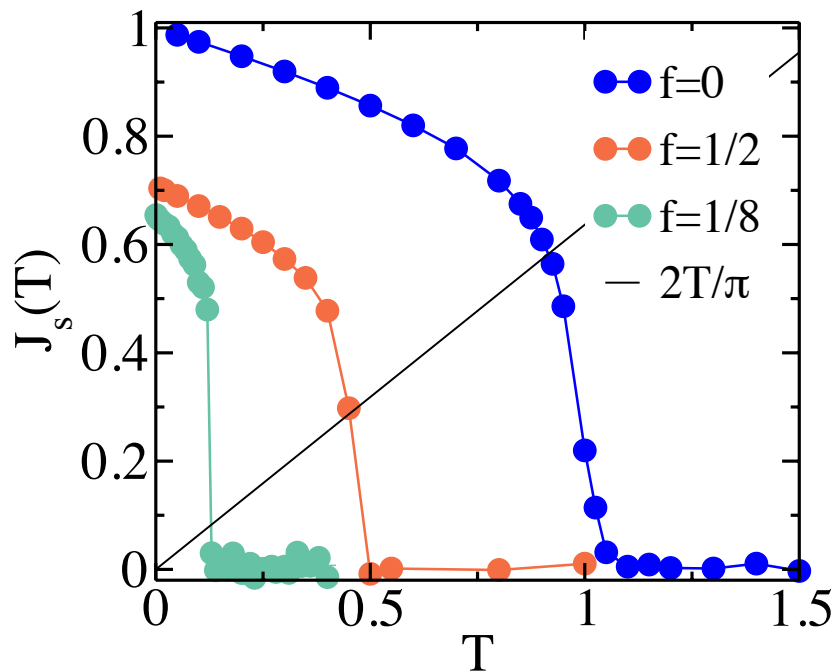
Figure 6.6. Superfluid stiffness behavior in temperature for different values of f.
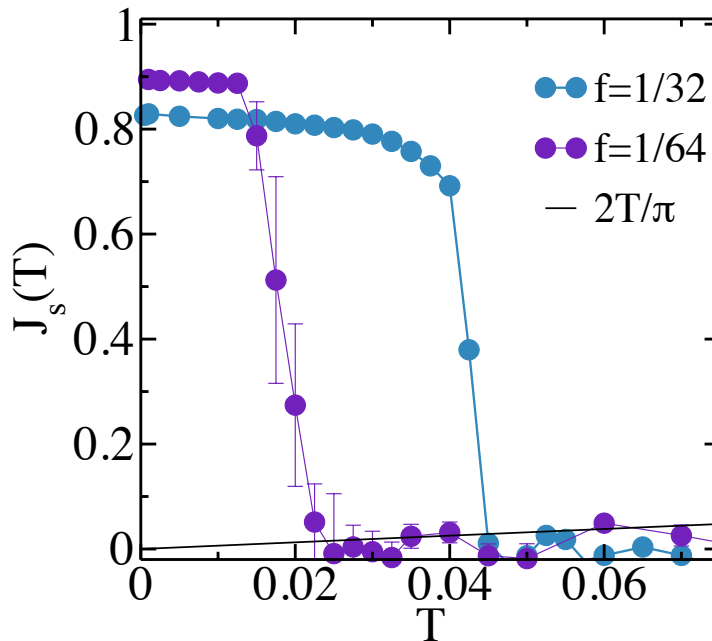
Figure 6.7. Superfluid stiffness behavior in temperature for different values of f, in the limit of small frustration.

6.3 XY model with $B\hat{z}$: disordered case

Let us now consider the case of a transverse magnetic field applied to a disordered SC film. We will address in this section two main issues: whether and how the inhomogeneity of the system is increased by the applied magnetic field and in which way the combined effect of disorder and finite uniform frustration f modifies the superconducting transition.

6.3.1 Increase of the inhomogeneity

From Fig.6.2, we have seen how both the zero-bias conductance $(G_N(0))$ and the hight of the peaks around the gap (G_{N_P}) become more and more inhomogeneous with the increase of the magnetic field applied to the system. To get a deeper insight in what observed, we will start again from the bosonic model for disordered superconductors of Eq.(3.8):

$$\mathcal{H}_{PS} = -2\sum_i \xi_i S_i^z - 2J \sum_{i,\mu=\pm\hat{x},\hat{y}} \left(S_i^+ S_{i+\mu}^- + h.c. \right) \tag{6.14}$$

Following the same procedure presented within the third chapter, we will derive a new expression for the local stiffness depending both on the disorder level and on the value of the applied field. Indeed, as already discussed, the maps of the local stiffness are directly connected with maps of the SC order parameter, measured experimentally via the height of the coherence peaks measured in[38] and indicated in 6.2 as G_{N_P}. In order to introduce a physical transverse magnetic field to (6.14), that

obviously has nothing to do with the pseudo random transverse field ξ_i mimicking the disorder, we have to proceed with the usual Peierls substitution:

$$S_i^+ S_{i+\mu}^- \to S_i^+ S_{i+\mu}^- e^{-iF_i^\mu} \tag{6.15}$$

where F_i^μ is exactly the one of Eq.(6.2). By means of this minimal substitution the pseudo-spin Hamiltonian (6.14) reads:

$$\mathcal{H}_{PS} = -2\sum_i \xi_i S_i^z - 4J \sum_{i,\mu=\pm\hat{x},\hat{y}} \big[\cos(F_i^\mu)\left(S_i^x S_{i+\mu}^x + S_i^y S_{i+\mu}^y\right) +$$

$$\tag{6.16}$$

$$+ \sin(F_i^\mu)\left(S_i^x S_{i+\mu}^y - S_i^y S_{i+\mu}^x\right)\big]$$

As before, let us firstly derive the mean-field solution of the model.

In the presence of a finite magnetic field, we can not anymore break the $U(1)$ symmetry by choosing a given direction, as we did by choosing $\hat{x}$ in the previous discussion, the mean field ground state indeed depends both on the angle ϕ_i the single spin forms with the $\hat{z}$ axis and the angle θ_i it forms with the $\hat{x}$ axis within the XY plane. This is after all expected in the presence of a transverse field, since the spins will form vortices within the XY plane so to minimise the energy of the system.

Hence, the mean-field ground state reads:

$$|\Psi_{MF}\rangle = \prod_i \Big[\cos(\phi_i/2)\big(\cos(\theta_i) - i\sin(\theta_i)\big)|\uparrow\rangle_i + \sin(\phi_i/2)|\downarrow\rangle_i\Big] \tag{6.17}$$

Being:

$$\begin{cases} \cos(\phi_i) = 2\langle S_i^z\rangle = \langle\sigma_i^z\rangle \\[2mm] \sin(\phi_i)\cos(\theta_i) = 2\langle S_i^x\rangle = \langle\sigma_i^x\rangle \\[2mm] \sin(\phi_i)\sin(\theta_i) = 2\langle S_i^y\rangle = \langle\sigma_i^y\rangle \end{cases} \tag{6.18}$$

The corresponding mean field energy is:

$$E_{MF}[\phi_i] = -\sum_i \xi_i \cos(\phi_i) - J\sum_{i,\mu=\pm\hat{x},\hat{y}} \sin(\phi_i)\sin(\phi_{i+\mu})\cos(\theta_i - \theta_{i+\mu} + F_i^\mu) \tag{6.19}$$

From which we can derive the two self-consistent equations:

$$\xi_i \sin(\phi_i) - J\cos(\phi_i)\sum_{\mu=\pm\hat{x},\hat{y}} \sin(\phi_{i+\mu})\cos(\theta_i - \theta_{i+\mu} + F_i^\mu) = 0 \tag{6.20}$$

$$J\sum_{i,\mu=\pm\hat{x},\hat{y}} \sin(\phi_{i+\mu})\sin(\theta_i - \theta_{i+\mu} + F_i^\mu) = 0 \tag{6.21}$$

We want now to consider the low energy excitations around the mean field solution. Thus, we will proceed by using the Holstein-Primakov (HP) approximation on the

new basis of quantisation, formed by the eigenvectors of the Hamiltonian(6.16). The new spin operator $S_i^{\|}$, relative to the new quantisation direction, and the other two along the orthogonal directions $S_i^{\perp}$ and S_i^{ϕ} are reconnected to the original spin operators by:

$$
\begin{pmatrix} S_i^x \\ S_i^y \\ S_i^z \end{pmatrix} = \begin{pmatrix} \sin\phi_i\cos\theta_i & \cos\phi_i\cos\theta_i & -\sin\theta_i \\ \sin\phi_i\sin\theta_i & \cos\phi_i\sin\theta_i & \cos\theta_i \\ \cos\phi_i & -\sin\phi_i & 0 \end{pmatrix} \begin{pmatrix} S_i^{\|} \\ S_i^{\perp} \\ S_i^{\phi} \end{pmatrix} \tag{6.22}
$$
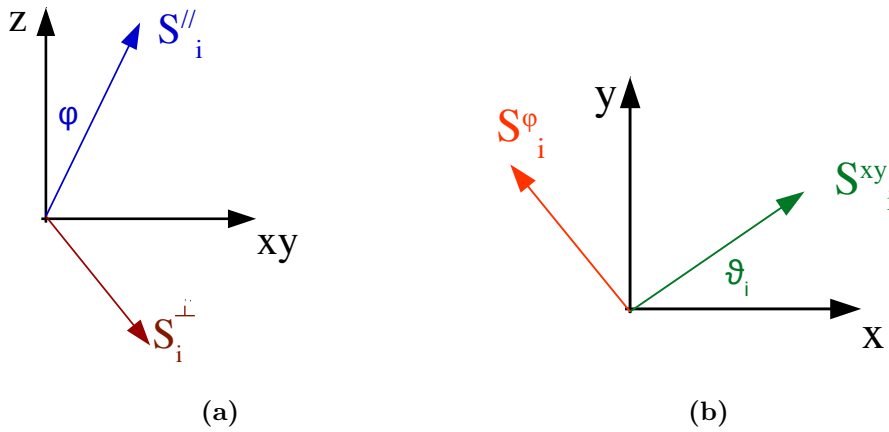
Figure 6.8. Schematic representation of the new axis of quantisation in the (a) $x - z$ and (b) $x - y$ plane respectively.

As before, the HP transformations can be implemented as:

$$
S_i^{\|} = \frac{1}{2} - a_i^{\dagger}a_i \tag{6.23}
$$

$$
S_i^{\perp} = \frac{1}{2i}(a_i - a_i^{\dagger}) \tag{6.24}
$$

$$
S_i^{\phi} = \frac{1}{2}(a_i + a_i^{\dagger}) \tag{6.25}
$$

By having truncated the expansion up to the quadratic term in the bosons operators $a_i^{\dagger}$ and a_i, we can rewrite the Hamiltonian in terms of the phase fluctuation quantum operator Θ_i and its conjugated momentum operator L_i, defined as:

$$
\Theta_i = \frac{2S_i^{\phi}}{\sin\phi_i} \tag{6.26}
$$

$$
L_i = \sin\phi_i S_i^{\perp} \tag{6.27}
$$

Indeed, by using the self-consistence equations (6.20)-(6.21), one can easily sees that the effective low-energy Hamiltonian 6.16 reduces to:

$$H \simeq E_{MF} + \frac{1}{2} \sum_{i,\mu=\pm\hat{x},\hat{y}} J \sin\phi_i \sin\phi_{i+\mu} \cos(\theta_i - \theta_{i+\mu} + F_i^\mu)(\Delta_\mu \Theta_i)^2 +$$

$$+ 4J \sum_{i,\mu=\pm\hat{x},\hat{y}} \cos(\theta_i - \theta_{i+\mu} + F_i^\mu) \Big(\frac{\sin\phi_{i+\mu}}{\sin^3\phi_i} L_i^2 - \frac{\cos\phi_i \cos\phi_{i+\mu}}{\sin\phi_i \sin\phi_{i+\mu}} L_i L_{i+\mu} \Big) \tag{6.28}$$

giving just a constant contribution to (6.28). Taken into account also in this case the classical limit of the above Hamiltonian 6.28, we can immediately recognise the XY model in its gaussian approximated form, having as coupling constant:

$$\tilde{J}_i^\mu \equiv J \sin\phi_i \sin\phi_{i+\mu} \cos(\theta_i - \theta_{i+\mu} + F_i^\mu) \tag{6.29}$$

the effective local stiffness of the model. The $\tilde{J}_i^\mu$'s in (6.29) result to be the product between the disordered and spatially-correlated ones J_i^μ, derived in the third chapter, and the cosine of the gauge invariant phase accounting for the presence of a finite transverse magnetic field. In principle, by solving the mean field self-consistent equations (6.20)-(6.21) one could directly study the zero temperature ground state of the system for any given disorder and magnetic field applied. They can remarkably also be used as input couplings for Monte Carlo simulations on the classical XY model, avoiding the computational effort to simulate the uniformly frustrated XY model. Nevertheless, obtaining the correct convergence of the self-consistent equations (6.20)-(6.21) is not an easy task, especially over large system. Indeed, because of the several possibilities for the system to build the ground state, it tends to find locally different solutions without obtaining the global correct one. This is why, despite the important result found, we have used Monte Carlo simulation in the presence of disordered J_i^μ coupling using as Hamiltonian the uniformly frustrated one (6.1). However, from the calculations just derived we know that the quantity connected to the experimentally measured G_{N_P} is the new local stiffness $\tilde{J}_i^\mu$ of Eq.(6.29). In particular one could say that $|\tilde{J}_i^\mu| \sim \Delta_i \Delta_{i+\mu}$.

Thus, to compare our results with the experimental data previously reported Fig.6.2, we have reported in Fig.6.9 the map in real space of the effective local-stiffness absolute value $|\tilde{J}_i^\mu|$. The maps shown have been obtained by means of MC simulations run with the Hamiltonian:

$$H_{XY} = - \sum_{\mu,i} J_i^\mu \cos(\theta_i - \theta_{i+\mu} + F_i^\mu) \tag{6.30}$$

where the coupling constant J_i^μ are the ones obtained in the third chapter from the disordered pseudo-spin Hamiltonian (3.8).

Specifically, the maps shown in Fig.6.9 correspond to the maps of the local observable:

$$\tilde{J}_{i\ MC}^\mu = J_i^\mu \langle \cos(\theta_i - \theta_{i+\mu} + F_i^\mu) \rangle \tag{6.31}$$

computed at the lowest temperature reached ($T = 0.005$), for the same given disorder configuration for all the values of f considered. The disordered couplings used here have been obtained at weak disorder with $W/J = 4$. Finally, as usual $\langle \ldots \rangle$ stays for the thermal average.
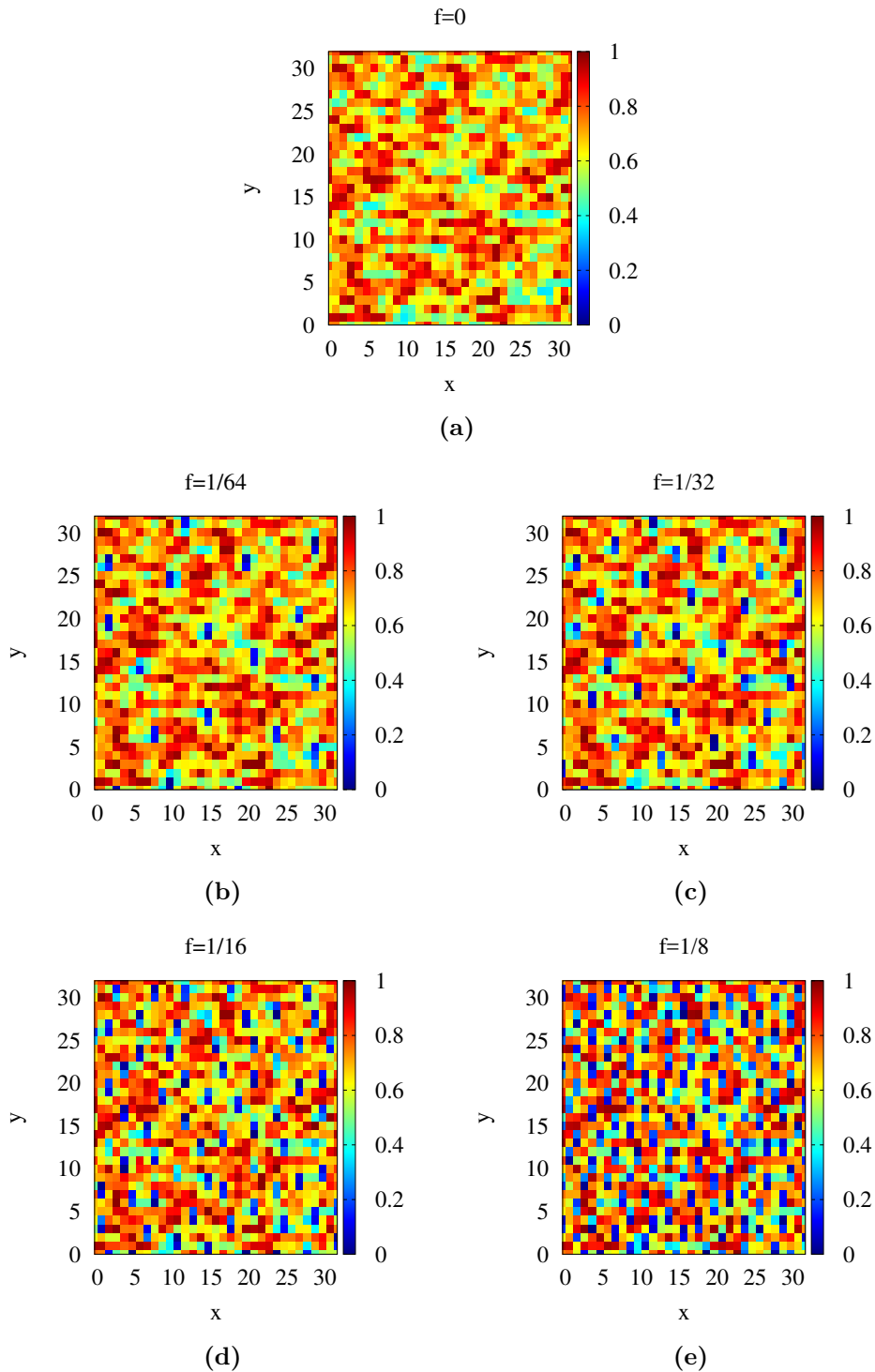
Figure 6.9. Maps in real space of the absolute value of the local stiffness $\tilde{J}^{\mu}_{i\ MC}$, obtained in the presence of both disorder and transverse magnetic field, for different values of the filling fraction f. The maps refer to the lowest temperature reached by our numerical simulations (here $T = 0.005$).

From Fig.6.9, it is well visible the increase of the spatial inhomogeneity with the increase of the frustration f as experimentally observed and reported in Fig6.2. In order to highlight and to better compare our results with the experimental ones, we also show the histograms obtained by the spatial distribution of $|\tilde{J}^{\mu}_{i\ MC}|$ and the correspondent histograms extrapolated from the experimental maps of G_{N_P}.

As one can see comparing Fig.6.10 and Fig.6.11, both the distributions become asymmetric at finite field, moving their spectral weight towards lower values with the increase of the magnetic flux f applied.

The maps have been obtained by simulating a system of size $L = 64$, the minimum value of f, because of the constraint in (6.8), corresponds to $f = 1/64$.
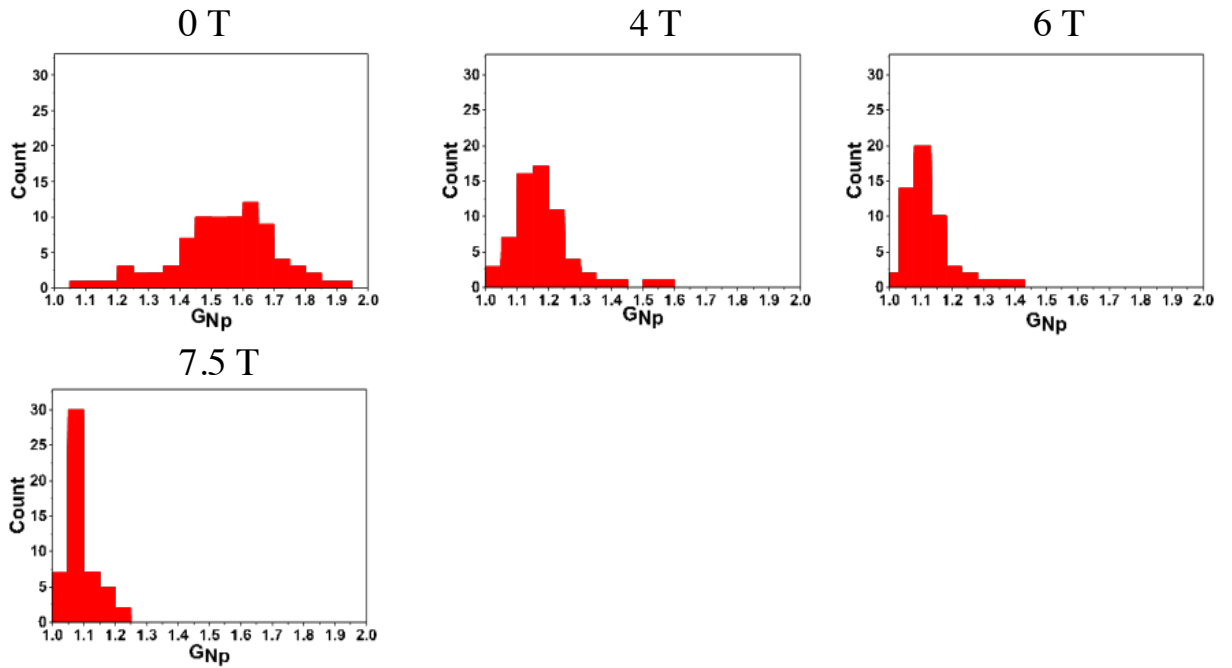
**Figure 6.10.** Histograms of the local values of G_{N_P} for different values of the field applied. These data are unpublished and provided by Prof. Pratap
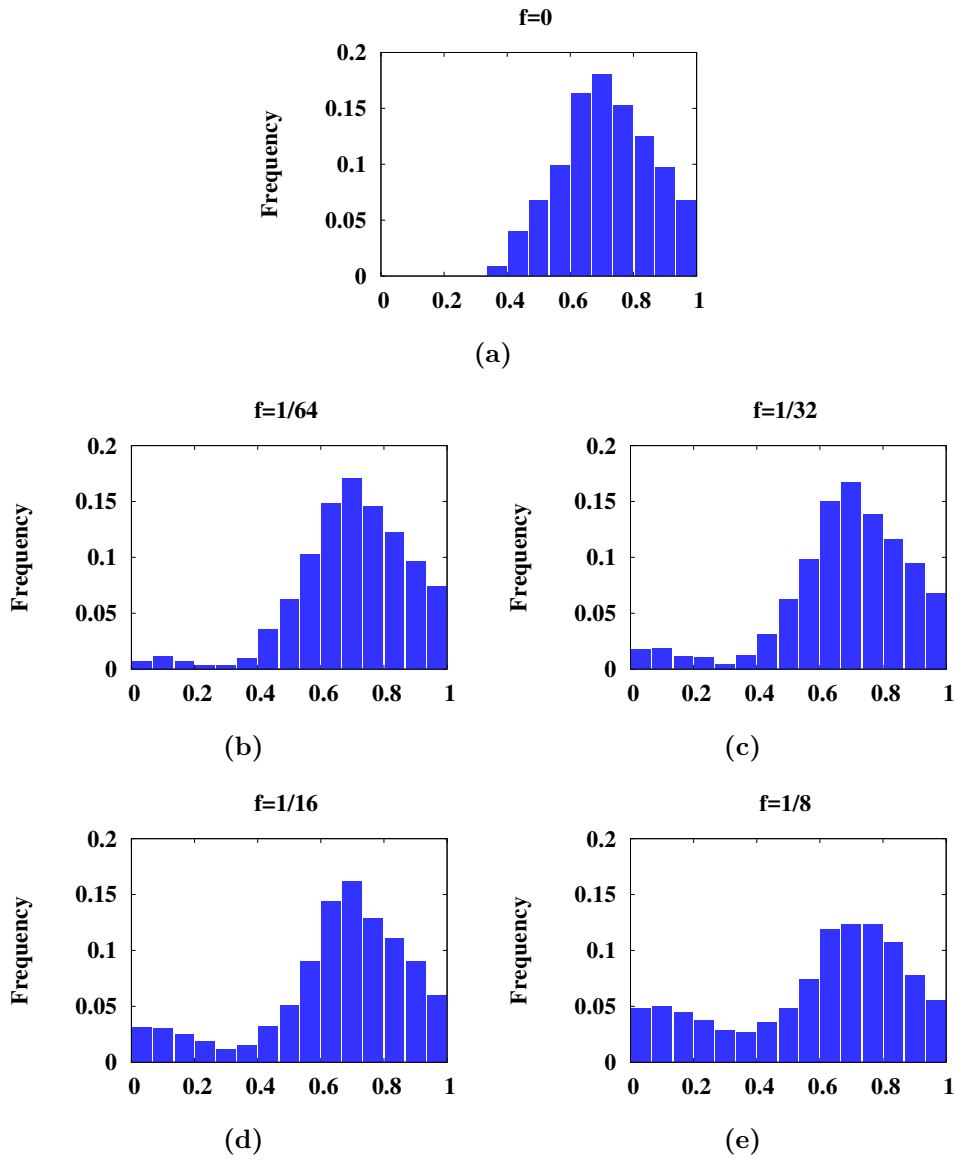
Figure 6.11. Histograms of the values assumed by the absolute value of the local stiffness $\tilde{J}^{\mu}_{i\ MC}$ within the system, at the lowest temperature investigated ($T = 0.005$).Different values of the applied magnetic field have been considered.

6.3.2 Abrikosov lattice of vortices

Consistently with the experimental observations of[38] reported in Fig.6.3, our MC numerical results also reveal that the presence of disorder within the system leads to a modification of the ground-state vortex lattice, as shown in Fig.6.12, enlighten in addition also the underlying mechanism. The core of the vortices, indeed, is pinned by the inhomogeneity of the local stiffness, which makes them moving towards those regions with lower $|\tilde{J}_i^\mu|$ so to gain in energy by minimising the Hamiltonian(6.30), as highlighted in Fig.6.12.
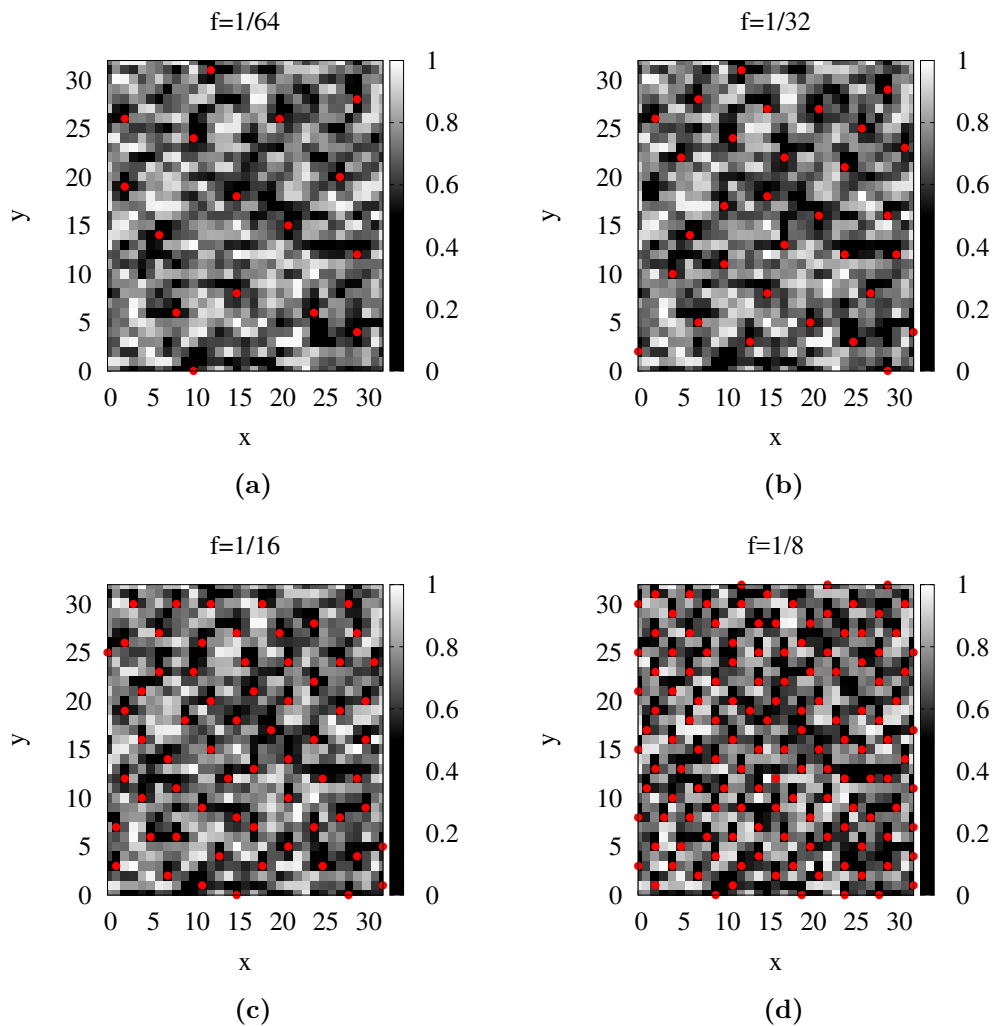
Figure 6.12. Vortex Lattice, in the presence of weak disordered couplings, for different values of the filling fraction f. Each red spot corresponds to a single vortex core, while the underlying colour map correspond to the maps of the local stiffness $|\tilde{J}_i^\mu|$.

It is also worth to stress that to observe a distortion of the vortex lattice, it is not needed specifically to consider spatially correlated disordered couplings. Indeed, the resulting vortex maps in Fig.6.12, have been obtained at weak disorder $W/J = 4$,

where the clustarisation of good and bad regions of couplings was still almost absent (look for istance Fig.5.10).

The reason is that in this case vortices are induced by the magnetic field and the mechanism observed is beyond the low-temperature anomalous vortices nucleation, which is instead observed only in presence of a large enough aggregation of low-couplings J_i^μ as largely discussed in the previous chapter.

To confirm the correlation in space between low-couplings regions and the vortices lattice deformation, in Fig. 6.12 we have superimposed the vortex lattice to the couplings map, obtained by computing over each plaquette the average value of the local stiffness J_i^μ.

6.3.3   Superconducting transition

Finally, let us address the issue of the interplay between intrinsic disorder and transverse magnetic field in terms of its effect on the superconducting transition.

In the previous sections we have seen how in absence of inhomogeneity, the application of an infinitesimal small magnetic field $f = 1/n$, dramatically suppresses the critical temperature of the system, moving it to zero as $\sim 1/n$.

However, the presence of disorder, by acting as pinning potential for the vortices, could reverse such trend restoring the dependence between T_c and f experimentally observed in thin SC films, as previously shown in Fig.6.4.
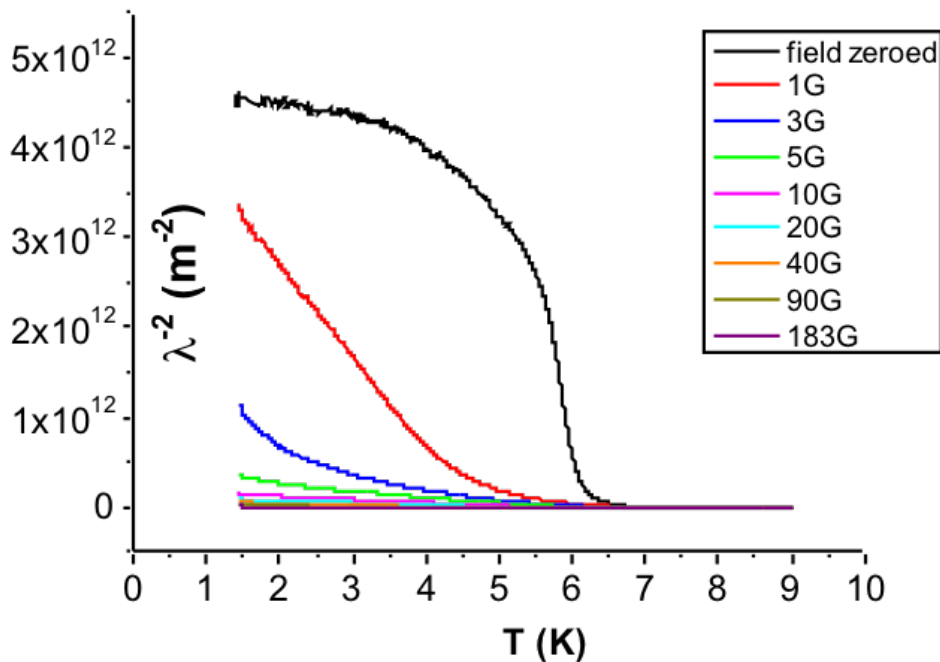
Figure 6.13. Preliminary experimental results obtained by the Prof. Raychaudhuri's group at the Tata Insitute of research in Mumbai. The system studied is a thin film of $MoGe$ investigated via the two-coils mutual inductance technique.

Very recently, the same trend registered in[48] has been also observed in weakly disordered thin SC films of *MoGe*. The preliminary experimental results, kindly provided by our collaborators at the Tata Institute of Fundamental Research in Mumbai, are shown in Fig.6.13.

The inverse penetration depth measurements, obtained via the two-coils mutual inductance technique, reveal a strong suppression of the superfluid stiffness for very low value of the field, which progressively leads to the complete loss of the superconducting state. Remarkably, the superconducting state disappears for an applied magnetic field much lower than the critical field H_{c2} at which the pair breaking occurs, causing the vanishing of the diamagnetic state. This means that the main mechanism leading to the loss of superconductivity observed in this system is driven by phase fluctuations, validating once more our theoretical approach to the problem. Nevertheless, the superfluid-stiffness temperature dependence reported in Fig.6.13 is completely different with respect to the zero-field case in which the BKT physics is observed.

By means of MC simulations on the disordered and uniformly frustrated XY model (6.30), we have thus measured the temperature evolution of the superfluid stiffness for different values of f.

In the presence of disordered couplings and uniform magnetic field the expression of J_s is a generalisation of (6.13):

$$
\begin{aligned}
J_s^\mu = {} & \frac{1}{L^2} \Big\langle \sum_i J_i^\mu \cos(\theta(\mathbf{r}_i) - \theta(\mathbf{r}_i + \hat{\mu}) + F_i^\mu) \Big\rangle + \\
& - \frac{\beta}{L^2} \Big\langle [\sum_i J_i^\mu \sin(\theta(\mathbf{r}_i) - \theta(\mathbf{r}_i + \hat{\mu}) + F_i^\mu)]^2 \Big\rangle + \\
& + \frac{\beta}{L^2} \Big\langle \sum_i J_i^\mu \sin(\theta(\mathbf{r}_i) - \theta(\mathbf{r}_i + \hat{\mu}) + F_i^\mu) \Big\rangle^2
\end{aligned}
\tag{6.32}
$$

where the averages have been performed both on the canonical ensemble (thermal average) and over 10 independent realisations of quenched disorder.

The numerical results, shown in Fig.6.14, confirm exactly our expectation: the presence of disorder restores the measured dependence between T_c and f by rendering more robust the vortex lattice against thermal fluctuations.

In this regard, it is quite impressive to notice that, compared to the homogeneous case (see Fig.6.7), the critical temperature T_c corresponding to the lowest value of f ($f = 1/64$) has increased by a factor of ten by the effects of the inhomogeneity.

Moreover, the whole superfluid stiffness trend in temperature in Fig.6.14, shows a great similarity with the experimental behavior of the penetration length measured on *MoGe* films (Fig.6.13). behavior that, nevertheless, has nothing to do with the BKT transition, as claimed in[48]. Indeed, from Fig. 6.14 one can see that at the intersection with the BKT critical line, any significant change in the superfluid-stiffness trend occurs.
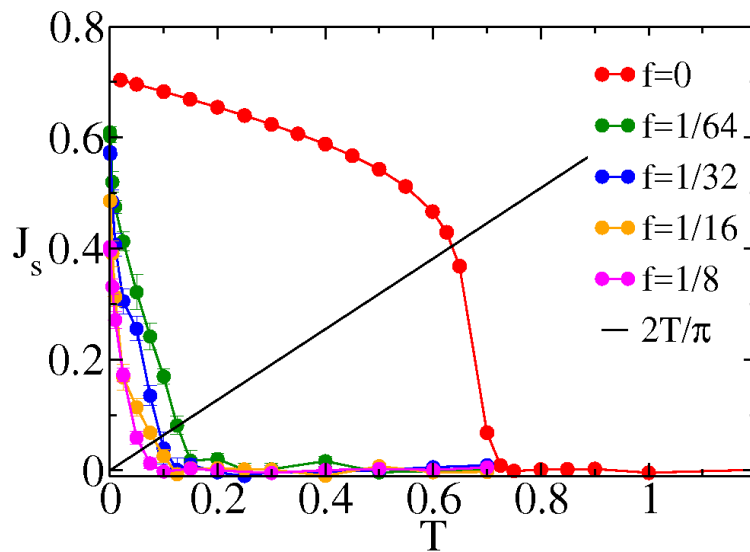
Figure 6.14. Temperature dependence of the superfluid stiffness in the presence of weak disorder $W/J = 4$, for different values of the frustration f. The continuous black line indicates the BKT critical line.

After having studied the weak disorder regime, let us investigate the case of strong disorder by using disordered couplings with $W/J = 10$.

From Fig.6.15, it is clear that in this case the transition appears to be even more robust with respect to the previous case. Looking for instance at the lowest value of the field ($f = 1/64$), the critical temperature is reduced, because of the field, just by half with respect to the zero-field value, while at weak disorder ($W/J = 4$) it was five times smaller.
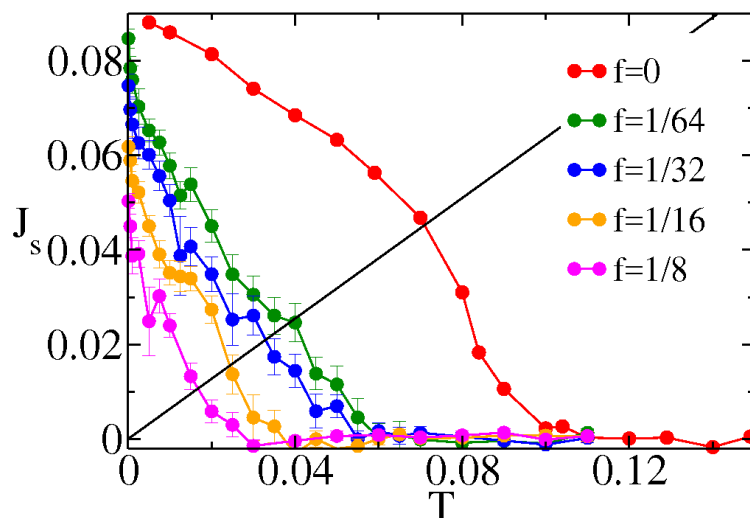
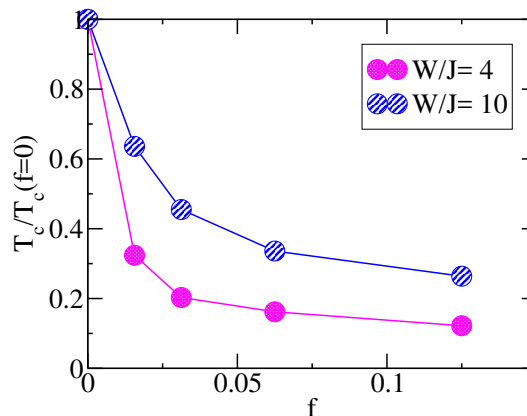**Figure 6.15.** Temperature dependence of the superfluid stiffness in the presence of strong disorder $W/J = 10$, for different values of the frustration f. The continuous black line indicates the BKT critical line.

In order to highlight such increase of robustness, as effect of the increase of the intrinsic disorder, we have reported in Fig.6.16 the extrapolated values of the critical temperature as function of the applied field, for the two disorder regime considered. In Fig.6.17, what just said is even more evident, having rescaled the curves of T_c by their value in absence of magnetic field.
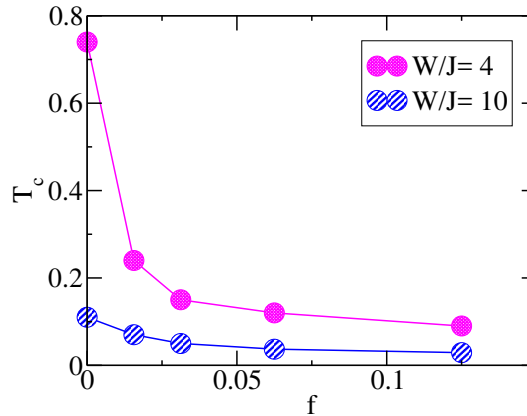
Figure 6.16. Magnetic field dependence of the critical temperature T_c for the two disorder level considered: $W/J = 4$ and $W/J = 10$.

Figure 6.17. Magnetic field dependence of the rescaled critical temperature $T_c(f)/T_c(f = 0)$for the two regime of disorder considered: $W/J = 4$ and $W/J = 10$.

Hence, despite separately both disorder and magnetic field act on the SC thin film by suppressing the superfluid stiffness, when a magnetic field is applied to the system, the presence of disorder help to prevent the destruction of the SC state by thermal fluctuations. However, the superfluid-stiffness temperature dependence in the presence of a finite magnetic flux changes completely nature with respect to the zero-field case. The occurring transition, indeed, has nothing to do with the BKT transition anymore, as confirmed by the experimental data reported in Fig.6.13. This work, made in collaboration with the experimental group of Prof. Raychaudhuri, is actually under preparation.

Chapter 7

Conclusions

In summary, in this PhD Thesis, I have investigated the BKT transition in the presence of disorder by means of Monte Carlo simulations within a XY model with random local couplings. I compared models with and without spatial correlations, focusing on the temperature dependence of the superfluid stiffness.

When disorder lacks spatial structure it appears irrelevant not only for the jump at criticality, as expected, but also away from it. Indeed, by rescaling the stiffness to its $T = 0$ value, suppressed by disorder, we observe a remarkable universal temperature dependence. The universality of the spin-wave excitations in the presence of uncorrelated disorder has been also demonstrated by means of a perturbation expansion of the disordered XY Hamiltonian around an effective value of the coupling. From this study, we derived and effective medium theory which gives access to the low temperature behavior of the superfluid stiffness, and also separately to the paramagnetic and the diamagnetic response function of the system, in the presence of uncorrelated disorder.

The main result of this work comes, however, from the study of XY model with spatially correlated couplings, modelled here as a fragmentation of the SC state in good islands embedded in a bad SC background. In this case the superfluid-density jumps is considerably smeared out both above and below the temperature where the universal jump would be expected. This effect is attributed to a different mechanism for the vortex-antivortex pair generation due to the presence of large clusters of low-SC regions. Our results not only provide an explanation for the trends observed experimentally in thin films of conventional [8, 15, 16, 17, 21, 18, 19, 20] and unconventional[22] superconductors, but they pave the way for the understanding of the topological excitations in gated 2D superconductors, where the inhomogeneity of the SC state is recently emerging[98, 13, 88, 97] as the hallmark of the field-induced electron doping. Finally, from the finite-size scaling analysis, we have shown that the presence of mesoscopic inhomogeneity within the system does not change the universality class of the BKT transition, affecting nonetheless the critical properties of the homogeneous XY model. Indeed, after having properly rescaled both the temperature and the superfluid stiffness, the critical temperature results to be lower with respect to the homogeneous case, and the divergence of the correlation length ξ faster in temperature in the presence of spatial correlated disorder.

The second issue I faced in this Thesis is the effect of a transverse magnetic field both

on the ground state properties of the system and on its superconducting transition. In particular, by means of Monte Carlo simulations on the uniformly frustrated XY model, I have shown that the presence of disorder, mimicked as before via random couplings, modifies the ordered vortex lattice of the ground state in agreement with some very recent experimental observations[38] made on thin $MoGe$ SC films. Moreover, we have also recovered that for a given weakly disorder configuration, the increase of the applied field corresponds to an increase of the intrinsic inhomogeneity, leading to a stronger fragmentation of the SC state, as found in [38].

Finally, the more intriguing result we have found within this last study, is the role of the inhomogeneity on the superfluid stiffness transition in the presence of a transverse magnetic field. Indeed, we have shown that it is needed to take into account the presence of intrinsic disorder in our uniformly frustrated XY model, so to recover the experimentally observed[48] dependence between the intensity of the applied field and the critical temperature of the system. In fact, the disorder acts in this case as a pinning potential for vortices, making the ground-state vortex lattice more robust against thermal fluctuations, which instead in the clean case would lead to the loss of the superfluid rigidity for a critical temperature as lower as smaller would be the magnetic field applied.

Bibliography

[1] V. L. Berezinsky. *Sov. Phys. JETP*, 34:610, 1972.

[2] J. M. Kosterlitz and D. J. Thouless. *J. Phys. C*, 6:1181, 1973.

[3] J. M. Kosterlitz. *J. Phys. C*, 7:1046, 1974.

[4] Singapore Jorge V. José, World Scientific, editor. *40 Years of Berezinskii-Kosterlitz-Thouless Theory.* 2013.

[5] D. McQueeney, G. Agnolet, and J. D. Reppy. *Phys. Rev. Lett.*, 52:1325, 1984.

[6] Z. Hadzibabic, P. Kr uger, M. Cheneau, B. Battelier, and J. Dalibard. *Nature*, 44:1118, 2006.

[7] P. A. Murthy, I. Boettcher, M. Holzmann L. Bayha, D. Kedar, M. Neidig, M. G. Ries, A. N. Wenz, G. Z urn, and S. Jochim. *Phys. Rev. Lett.*, 115:010401, 2015.

[8] A. T. Fiory, A. F. Hebard, and W. I. Glaberson. *Phys. Rev. B*, 28:5075, 1983.

[9] M. Mondal, S. Kumar, M. Chand, L. Benfatto A. Kamlapure G. Seibold, G. Saraswat, and P. Raychaudhuri. *Phys. Rev. Lett.*, 106:047001, 2011.

[10] D. M. Broun, W. A. Huttema, P. J. Turner, S. Ozcan, B. Morgan, R. Liang, W. N. Hardy, and D. A. Bonn. *Phys. Rev. Lett.*, 99:237003, 2007.

[11] P. G. Baity, Xiaoyan Shi, Zhenzhong Shi, L. Benfatto, and Dragana Popović. *Phys. Rev. B*, 93:024519, 2016.

[12] Julie A. Bert, Katja C. Nowack, Beena Kalisky, Hilary Noad, John R. Kirtley, Chris Bell, Hiroki K. Sato, Masayuki Hosoda, Yasayuki Hikita, Harold Y. Hwang, and Kathryn A. Moler. *Phys. Rev. B (R)*, 86:060503, 2012.

[13] Gopi Nath Daptary, Shelender Kumar, Pramod Kumar, Anjana Dogra, N. Mohanta, A. Taraphder, and Aveek Bid. *Phys. Rev. B*, 94:085104, 2016.

[14] Yu Saito, Yuichi Kasahara, Jianting Ye, and Tsutomu Nojima Yoshihiro Iwasa. *Science*, 350:409, 2015.

[15] S. J. Turneaure, T. R. Lemberger, and J. M. Graybeal. *Phys. Rev. Lett.*, 84:987, 2000.

[16] R. W. Crane, N. P. Armitage, A. Johansson, G. Sambandamurthy, D. Shahar, and G. Gruner. *Phys. Rev. B*, 75:094506, 2007.

[17] W. Liu, M. Kim, G. Sambandamurthy, and N. P. Armitage. *Phys. Rev. B*, 84:024511, 2011.

[18] M. Mondal, S. Kumar, M. Chand, A. Kamlapure, G. Saraswat, G. Seibold, L. Benfatto, and P. Raychaudhuri. *Phys. Rev. Lett.*, 107:217003, 2011.

[19] Y. h. Lin, J. Nelson, and A. M. Goldman. *Phys. Rev. Lett.*, 109:017002, 2012.

[20] S. Misra, L. Urban, M. Kim, G. Sambandamurthy, and A. Yazdani. *Phys. Rev. Lett*, 110:037002, 2013.

[21] A. Kamlapure, M. Mondal, M. Chand, A. Mishra, J. Jesudasan, V. Bagwe, L. Benfatto, V. Tripathi, and P. Raychaudhuri. *Appl. Phys. Lett.*, 96:072509, 2010.

[22] Jie Yong, M. J. Hinton, A. McCray, M. Randeria, M. Naamneh, A. Kanigel, and T. R. Lemberger. *Phys. Rev. B*, 85:180507, 2012.

[23] Y. Dubi, Y. Meir, and Y. Avishai. *Nature*, 449:876, 2007.

[24] A. Erez and Y. Meir. *Europhys. Lett.*, 91:47003, 2010.

[25] K. Bouadim, Y. L. Loh, M. Randeria, and N. Trivedi. *Nat. Phys.*, 7:884, 2011.

[26] E. J. K onig, A. Levchenko, I. V. Protopopov, I. V. Gornyi, I. S. Burmistrov, and A. D. Mirlin. *Phys. Rev. B*, 92:214503, 2015.

[27] S. Barabash, D. Stroud, and I.-J. Hwang. *Phys. Rev. B (R)*, 61:14924, 2000.

[28] G. M. Wysin, A. R. Pereira, I. A. Marques, S. A. Leonel, and P. Z. Coura. *Phys. Rev. B*, 72:094418, 2005.

[29] A. Erez and Y. Meir. *Phys. Rev. Lett.*, 111:187002, 2013.

[30] Y.-l. Loh M. Swanson, M. Randeria, and N. Trivedi. *Phys. Rev. X*, 4:021007, 2014.

[31] A. B. Harris. *J. Phys. C*, 7:1671, 1974.

[32] D. R. Nelson and J. M. Kosterlitz. *Phys. Rev. Lett.*, 19:1201, 1977.

[33] S. Kirkpatrick. *Rev. Mod. Phys*, 45:574, 1973.

[34] L. B. Ioffe and M. Mezard. *Phys. Rev. Lett.*, 105:037001, 2010.

[35] G. Lemarie, A. Kamlapure, D. Bucheli, L. Benfatto, J. Lorenzana, G. Seibold, S. C. Ganguli, P. Raychaudhuri, and C. Castellani. *Phys. Rev. B*, 87:184509, 2013.

[36] T. Cea, D. Bucheli, G. Seibold, L. Benfatto, J. Lorenzana, and C. Castellani. *Phys. Rev. B*, 89:174506, 2014.

[37] D. Matthey, N. Reyren, J. m. Triscone, and T. Schneider. *Phys. Rev. Lett.*, 98:057002, 2007.

[38] R. Ganguly, I. Roy, A. Banerjee, H. Singh, A. Ghosal, and P. Raychaudhuri. *Phys. Rev. B*, 96:054509, 2017.

[39] A. Pourret, H. Aubin, J. Lesueur, C. A. Marrache-Kikuchi, L. Bergé, L. Dumoulin, and K. Behnia. *Phys. Rev. B*, 76:214504, 2007.

[40] L. Li, Y. Wang, M. J. Naughton, S. Ono, Y. Ando, and N. P. Ong. *Europhys. Lett.*, 72:451, 2005.

[41] M. A. Cazalilla, A. Iucci, and T. Giamarchi. *Phys. Rev. A (R)*, 75:051603, 2007.

[42] K. Kasamatsu. *Phys. Rev. A*, 79:021604, 2009.

[43] P. Minnhagen. *Rev. Mod. Phys*, 59:1001, 1987.

[44] L. Benfatto, C. Castellani, and T. Giamarchi. *Phys. Rev. Lett.*, 99:207002, 2007.

[45] K. Kim and D. Stroud. *Phys. Rev. B*, 78:174517, 2008.

[46] S. Teitel and C. Jayaprakash. *Phys. Rev. B (R)*, 27:598, 1983.

[47] V. Alba, A. Pelissetto, and E. Vicari. *J. Phys. A*, 41:175001, 2008.

[48] S. Misra, L. Urban, M. Kim, G. Sambandamurthy, and A. Yazdani. *Phys. Rev. Lett.*, 110:037002, 2013.

[49] I. Maccari, L. Benfatto, and C. Castellani. *Phys. Rev. B*, 96:060508, 2017.

[50] N. D. Mermin and H. Wagner. *Phys. Rev. Lett.*, 17:1133, 1966.

[51] R. Peierls. *Proc. Cambridge Phil. Soc.*, 32:477, 1936.

[52] P. C. Hohenberg. *Phys. Rev.*, 158:383, 1967.

[53] N. Nagaosa. *Quantum field theory in condensed matter physics*. Springer.

[54] M. H. W. Chan, A. W. Yanof, and J. D. Reppy. *Phys. Rev. Lett.*, 32:1347, 1974.

[55] L. Benfatto, C. Castellani, and T. Giamarchi. *Phys. Rev. B*, 80:214506, 2009.

[56] L. Benfatto, C. Castellani, and T. Giamarchi. In Jorge V. José, editor, *Book Chapter in "40 Years of Berezinskii-Kosterlitz-Thouless Theory"*. World Scientific, 2013.

[57] K. G. Wilson. *Rev. Mod. Phys*, 47:773, 1975.

[58] T. Giamarchi. *Quantum physics in one dimension.*

[59] M. R. Beasley and J. E. Mooij ad T. P. Orlando. *Phys. Rev. Lett.*, 42:1165, 1979.

[60] S. Doniach and B. A. Huberman. *Phys. Rev. Lett.*, 42:1169, 1979.

[61] B. I. Halperin and D. R. Nelson. J. low temp. phys. 36:590, 1979.

[62] I. Hetel, T. R. Lemberger, and M. Randeria. *Nat. Phys.*, 3:700, 2007.

[63] E. P. Gross. *Il Nuovo Cimento*, 20:454, 1961.

[64] L. P. Pitaevskii. *Sov. Phys. JETP.*, 13:451, 1961.

[65] V. L. Ginzburg and L. D. Landau. *Zh. Eksp. Teor. Fiz.*, 20:1064, 1950.

[66] M. Tinkham. *Introduction to Superconductivity.*

[67] J. Pearl. *Appl. Phys. Lett.*, 5:65, 1964.

[68] S. J. Turneaure, T. R. Limburger, and J. M. Graybeal. *Phys. Rev. B.*, 63:174505, 2001.

[69] L. Li, Y. Wang, S. Komiya, S. Ono, Y. A. G. D. Gu, and N. P. Ong. *Phys. Rev. B.*, 81:054510, 2010.

[70] L. G. Aslamov and A. I. Larkin. *Sov. Phys. Solid State*, 10:875, 1968.

[71] A. Larkin and A. A. Varlamov. *Thoery of fluctuations in superconductors.* Oxford University Press, 2005.

[72] H. Schmidt. *Phys. Rev.*, 180:527, 1969.

[73] A. T. Fiory, A. F. Hebard, and W. I. Glaberson. *Phys. Rev. B*, 28:5075, 1983.

[74] K. Epstein, A. M. Goldman, and A. M. Kadin. *Phys. Rev. B*, 27:6691, 1983.

[75] M. Mondal, A. Kamlapure, M. Chand, G. Saraswat, S. Kumar, J. Jesudasan, L. Benfatto, V. Tripathi, and P. Raychaudhuri. *Phys. Rev. Lett*, 106:047001, 2011.

[76] L. S. Bilbro, R. V. Aguilar, G. Logvenov, O. Pelleg, I. Bosović, and N. P. Armitage. *Nat. Phys.*, 7:298, 2011.

[77] S. J. Turneaure, E. R. Ulm, and T. T. Lemberg. *J. Appl. Phys.*, 79:4221, 1996.

[78] G. Blatter, M. V. Feigel'man, V. B. Geshkenbein, A. I. Larkin, and V. M. Vinkour. *Rev. Mod. Phys*, 66:1125, 1994.

[79] V. J. Emery and S. A. Kivelson. *Nature (London)*, 374:434, 1995.

[80] P. A. Lee, N. Nagaosa, and X. g. Wen. *Rev. Mod. Phys*, 78:17, 2006.

[81] J. Corson, R. Mallozzi, J. Orenstein, J. N. Eckstein, and I. Bozovic. *Nature*, 398:221, 1999.

[82] L. Benfatto, C. Castellani, and T. Giamarchi. *Phys. Rev. Lett.*, 98:117008, 2007.

[83] Y. L. Zuev, M. s. Kim, and T. R. Lemberger. *Phys. Rev. Lett.*, 95:137002, 2005.

[84] C. Chapelier B. Sacepe, T. I. Baturina, V. M. Vinokur, M. R. Baklanov, and M. Sanquer. **1**, 140 (2010). b. *Nature Communications*, 1:140, 2011.

[85] C. Brun, T. Cren, V. Cherkez, F. Debontridder, S. Pons, D. Fokin, M. C. Tringides, S. Bozhko, L. B. Ioffe, B. L. Altshuler, and D. Roditchev. *Nat. Phys.*, 10:444, 2014.

[86] A. Ghosal, M. Randeria, and N. Trivedi. *Phys. Rev. B*, 65:014501, 2001.

[87] C. Carbillet, S. Caprara, M. Grilli, C. Brun, T. Cren, F. Debontridder, B. Vignolle, W. Tabis, D. Demaille, L. Largeau, K. Ilin, M. Siegel, D. Roditchev, and B. Leridon. *Phys. Rev. B*, 93:144509, 2016.

[88] G. E. D. K. Prawiroatmodjo, F. Trier, D. V. Christensen, Y. Chen, N. Pryds, and T. S. Jespersen. *Phys. Rev. B*, 93:184504, 2016.

[89] K. K. Gomes, A. N. Pasupathy, A. Pushp, S. Ono, Y. Ando, and A. Yazdani. *Nature (London)*, 447:569, 2007.

[90] P. W. Anderson. *J. Phys. Chem. Solids*, 11:26, 1959.

[91] G. Saraswat M. Chand, A. Kamlapure, M. Mondal, S. Kumar, J. Jesudasan, V. Bagwe, L. Benfatto, V. Tripathi, and P. Raychaudhuri. Phys. *Rev. B*, 85:014508, 2012.

[92] P. G. de Gennes. *Superconductivity in Metals and Alloys.* Benjamin, New York, 1966.

[93] G. Seibold, L. Benfatto, C. Castellani, and J. Lorenzana. *Phys. Rev. Lett.*, 108:207004, 2012.

[94] M. Ma and P. A. Lee. *Phys. Rev. B*, 32:5658, 1985.

[95] A. Kamlapure, T. Das, S. Chandra Ganguli, J. B. Palmar, S. Bhattacharyya, and P. Raychaudhuri. *Sci. Rep.*, 3:2979, 2013.

[96] Y. Noat, T. Cren V. Cherkez, C. Brun, C. Carbillet, F. Debontridder, K. Ilin, M. Siegel, A. Semenov, H. w. H ubers, and D. Roditchev. *Phys. Rev. B*, 88:014503, 2013.

[97] C. Brun, T. Cren, and D. Roditchev. *Supercond. Sci. Technol.*, 30:013003, 2017.

[98] J. Biscaras, N. Bergeal, S. Hurand, C. Feuillet-Palma, A. Rastogi, R. C. Budhani, M. Grilli, S. Caprara, and J. Lesueur. *Nat. Mater.*, 12:542, 2013.

[99] M. E. J. Newmann and G. T. Barkema. *Monte Carlo Methods in Statistical Physics.* Oxford University Press, 1999.

[100] R. H. Swendsen and J. S. Wang. *Phys. Rev. Lett.*, 57:2607, 1986.

[101] A. Weinrib and B. I. Halperin. *Phys. Rev. B*, 27:1, 1983.

[102] K. Epstein, A. M. Goldman, and A. M. Kadin. *Phys. Rev. Lett*, 47:534, 1981.

[103] J. Hoshen and R. Kopelman. *Phys. Rev. B*, 14:3438, 1976.

[104] N. Schultka and E. Manousakis. *Phys. Rev. B*, 49:12071, 1993.

[105] M. Hasenbusch. *J. Phys. Gen. A: Math.*, 38:5869, 2005.

[106] M. E. Fisher and M. N. Barber. *Phys. Rev. Lett.*, 28:1516, 1972.

[107] A. W. Sandvick. *Aip Conf. Proc.*, 1297:135, 2010.

[108] D. S. Fisher, M. P. A. Fisher, and D. A. Huse. *Phys. Rev. B*, 43:130, 1991.

[109] A. A. Abrikosov. *Sov. Phys. JETP*, 5:1174, 1957.

[110] M. Hasenbusch, A. Pelissetto, and E. Vicari. *J. Stat. Mech*, P12002, 2005.

[111] W. Y. Shih and D. Stroud. *Phys. Rev. B*, 30:6774, 1984.

[112] S. Teitel and C. Jayaprakash. *Phys. Rev. Lett.*, 51:1999, 1983.

[113] P. Olsson. *Phys. Rev. Lett.*, 75:2758, 1995.

[114] S. A. Hattel and J. M. Wheatley. *Phys. Rev. B*, 51:11951, 1995.